

AD-A195 716

APPLICATION OF NONDESTRUCTIVE TESTING TECHNIQUES TO
MATERIALS TESTING(U) STANFORD UNIV CA EDWARD L GINZTON
LAB OF PHYSICS G S KING DEC 87 AFOSR-TR-88-0667

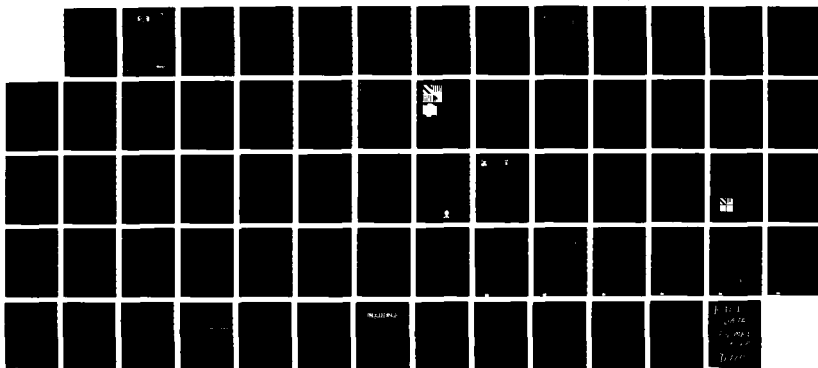
1/1

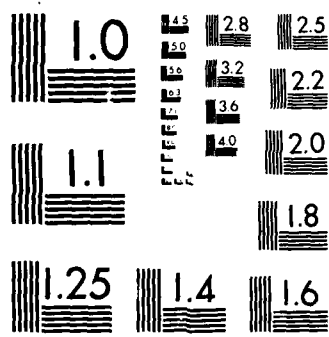
UNCLASSIFIED

AFOSR-84-0063

F/G 14/2

NL





MICROCOPY RESOLUTION TEST CHART
NATIONAL BUREAU OF STANDARDS-1963-A

2

REPORT DOCUMENTATION PAGE

AD-A195 716

1b. RESTRICTIVE MARKINGS **OTIC FILE COPY**

2b. DECLASSIFICATION / DOWNGRADING SCHEDULE

3. DISTRIBUTION / AVAILABILITY OF REPORT
Approved for public release;
distribution unlimited.

4. PERFORMING ORGANIZATION REPORT NUMBER(S)

5. MONITORING ORGANIZATION REPORT NUMBER(S)
AFOSR-TR- 88 - 0 6 6 7

6a. NAME OF PERFORMING ORGANIZATION
Stanford University

6b. OFFICE SYMBOL
(if applicable)

7a. NAME OF MONITORING ORGANIZATION
AFOSR/NE

6c. ADDRESS (City, State, and ZIP Code)
Edward L. Ginzton Laboratory
W. W. Hensen Laboratories of Physics
Stanford, CA 94305-1502

7b. ADDRESS (City, State, and ZIP Code)
Bldg 410
Bolling AFB, DC 20332-6448

8a. NAME OF FUNDING / SPONSORING ORGANIZATION
AFOSR/

8b. OFFICE SYMBOL
(if applicable)
NE

9. PROCUREMENT INSTRUMENT IDENTIFICATION NUMBER
AFOSR-84-0063

8c. ADDRESS (City, State, and ZIP Code)
Bldg 410
Bolling AFB, DC 20332-6448

10. SOURCE OF FUNDING NUMBERS
PROGRAM ELEMENT NO. 61102F
PROJECT NO. 2306
TASK NO. A3
WORK UNIT ACCESSION NO.

11. TITLE (Include Security Classification)
Application of Nondestructive Testing Techniques to Materials Testing

12. PERSONAL AUTHOR(S)
Professor Kino

13a. TYPE OF REPORT
FINAL

13b. TIME COVERED
FROM 010184 TO 301187

14. DATE OF REPORT (Year, Month, Day)

15. PAGE COUNT

16. SUPPLEMENTARY NOTATION

17. COSATI CODES
FIELD GROUP SUB-GROUP

18. SUBJECT TERMS (Continue on reverse if necessary and identify by block number)
AIRCRAFT, COMPOSITE MATERIALS, INTEGRATED CIRCUITS, STRUCTURAL MECHANICS, PHOTO MEASUREMENT, METAL FILMS, EMAY COMPOSITE, FIBER OPTICS, TEST

19. ABSTRACT (Continue on reverse if necessary and identify by block number)
A set of new techniques in scanning acoustic and optical microscopy is described. Starting with an acoustic microscope that can directly measure both phase and amplitude, similar techniques have been developed for the scanning optical microscope. These make it possible to measure range to a thousandth of a wavelength. Other techniques involving scanning optical microscopy have been demonstrated which make it possible to carry out profiling of semiconductor circuits. Developments of these methods are now being actively pursued for use in the semiconductor industry. Developments of acoustic technology pioneered on this program have proven extremely important for measuring internal defects in composites and surface cracks on ceramics.

20. DISTRIBUTION / AVAILABILITY OF ABSTRACT
☐ UNCLASSIFIED/UNLIMITED ☐ SAME AS RPT ☐ OTIC USERS

21. ABSTRACT SECURITY CLASSIFICATION
UNCLASSIFIED

22a. NAME OF RESPONSIBLE INDIVIDUAL
WEINSTOCK

22b. TELEPHONE (Include Area Code)
202-767-4933

22c. OFFICE SYMBOL
NE

Final Report
to
Air Force Office of Scientific Research
for

**APPLICATION OF NONDESTRUCTIVE TESTING
TECHNIQUES TO MATERIALS TESTING**

Contract No. AFOSR 84-0063

Principal Investigator:
G. S. Kino

December 1987

Accession For	
NTIS CRA&I	<input checked="checked" type="checkbox"/>
DTIC TAB	<input type="checkbox"/>
Unannounced	<input type="checkbox"/>
Justification	
By	
Distribution/	
Availability Codes	
Dist	A.S. (for Subject)
A-1	



Edward L. Ginzton Laboratory
W. W. Hansen Laboratories of Physics
Stanford University
Stanford, California 94305-1502

APPLICATION OF NONDESTRUCTIVE TESTING TECHNIQUES TO MATERIALS TESTING

G. S. Kino

SUMMARY

A set of new techniques in scanning acoustic and optical microscopy is described. Starting with an acoustic microscope that can directly measure both phase and amplitude, similar techniques have been developed for the scanning optical microscope. These make it possible to measure range to a thousandth of a wavelength. Other techniques involving scanning optical microscopy have been demonstrated which make it possible to carry out profiling of semiconductor circuits. Developments of these methods are now being actively pursued for use in the semiconductor industry. Developments of the acoustic technology pioneered on this program have proven extremely important for measuring internal defects in composites and surface cracks on ceramics.

INTRODUCTION

The purpose of this program has been to develop new techniques of nondestructive testing as in the forerunning AFOSR contract, Contract No. F49620-79-C-0217. During the earlier contract period we developed acoustic wave techniques to examine materials of the type typically used in aircraft and in various types of structural components. During that time, we pioneered the development of new types of electronically-scanned acoustic imaging systems and highly successful new theoretical approaches for determining the attenuation of waves in polycrystalline materials. Toward the end of that contract, surrounded as we are by Silicon Valley, our interests began to change toward the examination of small devices such as integrated circuits and other electronic components. We therefore began to develop acoustic microscopy techniques suitable for examining composite materials and structural ceramics, as well as electronic components. This work was continued on the contract being reviewed here.

A second program begun on the first contract was concerned with using fiber-optic techniques to measure the displacement of the surface of an object by surface acoustic waves propagating along it. This noncontacting technique was used to measure the depth and size of surface cracks and other defects in metals and ceramics, and proved to be very powerful for measuring the properties of surface acoustic wave devices. It is now in regular use at Hewlett-Packard, Santa Rosa, where it is employed for measuring wavefronts in their surface acoustic wave resonators.

The work on this contract led to major new developments in acoustic and optical microscopy. One example is our development of the first acoustic microscope capable of measuring phase directly. With this microscope, we were able to use Fourier transform techniques to directly measure the reflectivity, as a function of angle of plane waves, incident on the surface of a material, and to measure the thickness of metal films of the order of 1000 \AA thick using waves with a wavelength of $30 \text{ }\mu\text{m}$.^{1,2} The devices were therefore very sensitive to minor changes in material properties, to the presence of small defects, and particularly cracks. As an example, we were able to measure the stress variation across a disc of glass with this noncontacting method. The work on acoustic microscopy is now being continued by Professor Khuri-Yakub on another program where the techniques developed out of the AFOSR program have proved to be particularly useful for measuring the width, depth, and features of defects inside epoxy composite materials, and for the measurement of cracks in ceramics associated with surface machining.

The work on fiber-optic sensors combined with our background in acoustic microscopy, which gave us a different viewpoint from standard optical microscopists, led to a range of new types of scanning optical microscopes. The first of these, an electronically-scanned scanning optical microscope, was developed on this contract and was the first optical microscope capable of directly measuring phase and amplitude.³ One example of the use of this technique is that of a precision range sensor suitable for use in robotics.⁴

Later developments arising from this work have included yet other types of real-time scanning optical microscope, and a device called the correlation microscope. The first of these devices is now being developed commercially from our design. The major advantage of such scanning optical microscopes is that they have excellent depth resolution along with transverse resolution, and contrast is somewhat better than with standard microscopes. This makes it possible to measure the profiles of integrated circuits with low submicron resolutions, and to determine the thickness of films with resolutions of the order of 10 \AA .

Three theses were written during the time of this contract. One was on precision phase measurements in acoustic microscopy.⁵ The second was on the fiber-optic sensor and the electronically scanned scanning optical microscope.⁶ Both of these devices resulted in patents. The third thesis concerned itself with the development of the electronically-scanned scanning optical microscope.⁷

We shall discuss this work in more detail below, and refer the reader to the Appendix and our published papers for still fuller descriptions of the research.

DESCRIPTION OF PROJECTS

Phase Measuring Acoustic Microscope

A 50 MHz phase measuring acoustic microscope was constructed as shown in Fig 1.⁸ A ceramic transducer, with a 20% bandwidth, was indium bonded to a quartz buffer rod in which was ground a 3.2 mm spherical depression which formed a lens with a focal length of 4.24 mm in water. When the surface of a solid was placed nearer to the lens than the focal plane, two waves could be set up by a short tone burst exciting the transducer. The first corresponded to direct specular reflection from the surface, and the second to the excitation of a Rayleigh wave which propagated along the surface. The received tone burst corresponding to the Rayleigh wave is delayed relative to the specular reflection. Thus, it was possible to gate the two tone bursts and switch them into separate circuits. By this means, we were able to design a circuit which could measure the phase difference of the carriers corresponding to the two tone bursts, and hence the surface wave velocity along the substrate. By using, instead, a reference corresponding to a pulse reflected from the flat sides of the buffer rod, it was also possible to measure the relative phase or time delay of the specularly-reflected pulse from the object, and hence the distance from the object with good accuracy.

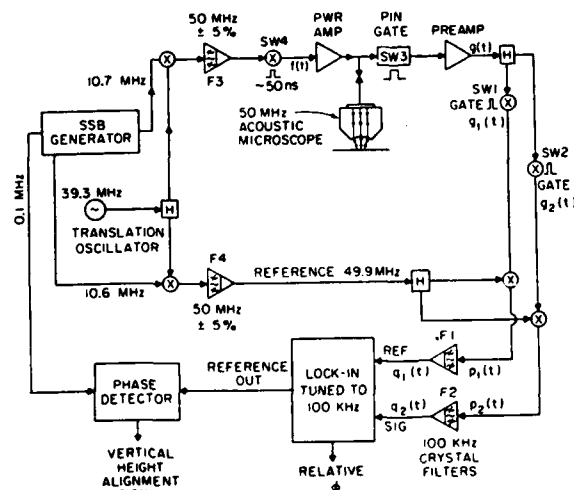


Fig. 1. Schematic of the phase measurement system.

We developed the phase measurement system described in more detail in reference 8, which is part of the Appendix. Suffice it to say that with pulses only two or three cycles

long, it is possible to measure the phase to an accuracy of the order 0.1^0 ; hence we were able to measure changes in velocity along the Rayleigh wave path, which is of the order of 1-2 mm long, to accuracies of one part in 10^5 .

In the accompanying papers in the Appendix,^{1,2,8} examples are given of the power of this device. We were able to measure the thickness of thin indium overlays of the order of 1000 \AA thick, with good accuracy and also the stress distribution in a glass plate. By using Fourier transforms with the phase and amplitude information obtained, we were able to measure the reflectance function as a function of angle for a plane wave incident on various types of substrates.

These techniques required considerable development of fundamental new phase measurement methods for short tone bursts. At the same time, we developed a considerable body of theory to interpret the measurements. This theory has been fundamental to our understanding of both scanning acoustic, and the later scanning optical, microscopes.

Electronically-Scanned Scanning Optical Microscope

This device has the capability of measuring both optical amplitude and phase. The ideas behind it are basic to much of the present work we are carrying out on new programs on phase contrast microscopy, and the work developed towards the end of the AFOSR program on mechanically-scanned scanning optical microscopes.^{3,6,7,9,10}

In the electronically-scanned microscope, shown in Fig. 2, a collimated laser beam passes through a Bragg cell and is diffracted into two beams, one of which may be scanned by varying the input frequency f_b to the Bragg cell. The other stationary undiffracted beam is used as a reference. Both beams are passed through transfer lenses into the microscope objective and are focused to two spots on the object. The light from the two spots passes back through the lenses and the Bragg cell. The reference beam is diffracted into a beam which travels in the same direction as the reflected, scanned beam. The two coincident beams, one of which is upshifted by a frequency f_b and the other, which is downshifted by f_b , pass into a detector and an output signal is obtained at a frequency $2f_b$.

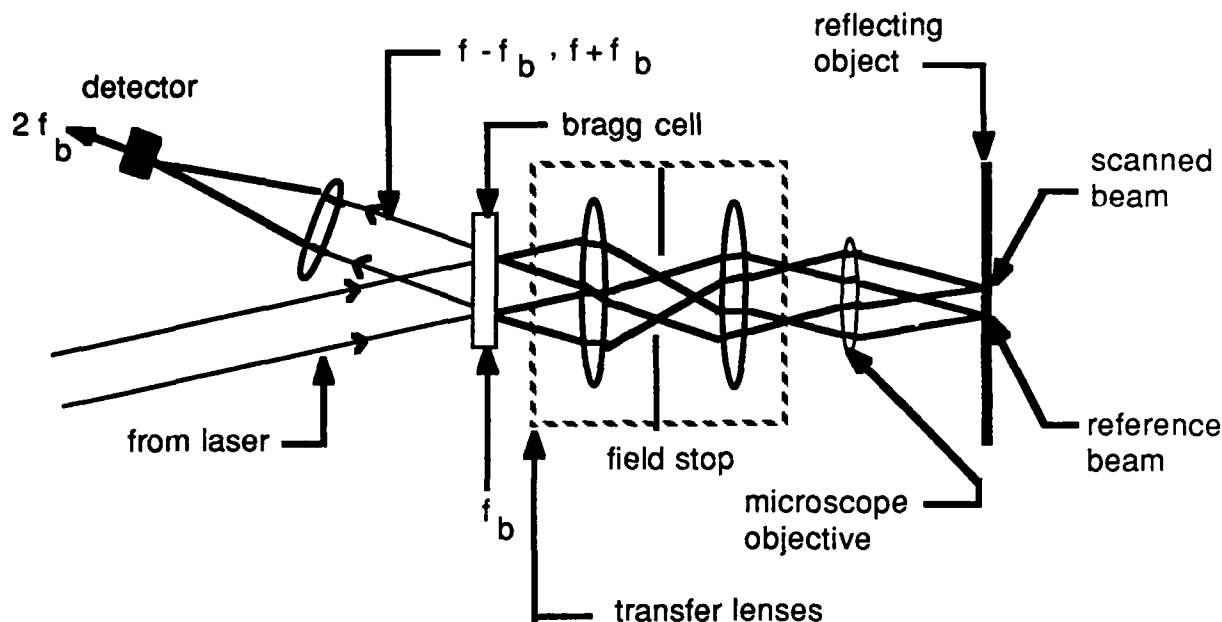


Fig. 2. Schematic of the electronically-scanned microscope.

As the beam is scanned across the object, the output signal from the detector at a frequency $2f_b$ in the 100-200 MHz range has an amplitude which varies with the reflectivity of the sample, and a phase which depends on the phase difference between the reference beam and the moving beam. Since phase can be measured to an accuracy of 0.1° , this implies that variations in height can be measured to an accuracy of the order of 1 \AA . In our experimental system, phase and amplitude can be measured to this accuracy at a rate of $20 \mu\text{s/spot}$. As far as we are aware, this system is one of the fastest for measuring phase and amplitude simultaneously that has been developed. The results obtained with it, and the method of digitization of the data, are described in the accompanying articles in the Appendix.^{9,11}

The advantages of phase contrast microscopy are already familiar. In reflection microscopy, measurement of phase makes it possible to measure profiles, or height, independently of changes in reflectivity. In addition, contrast between regions of different heights, but with the same reflectivity, such as a groove in metal, are greatly enhanced by the use of a phase image. As an example, a line scan of a titanium-gold line on silicon is shown in Fig. 3. It will be seen that phase measurements give better results than amplitude measurements in this case. Using a 0.95 N.A. objective lens, with argon laser illumination of a wavelength of 510 nm , the edge definition of the phase scan of a step of aluminum on aluminum, from the 10-90% height points, is 250 nm . Furthermore, because both

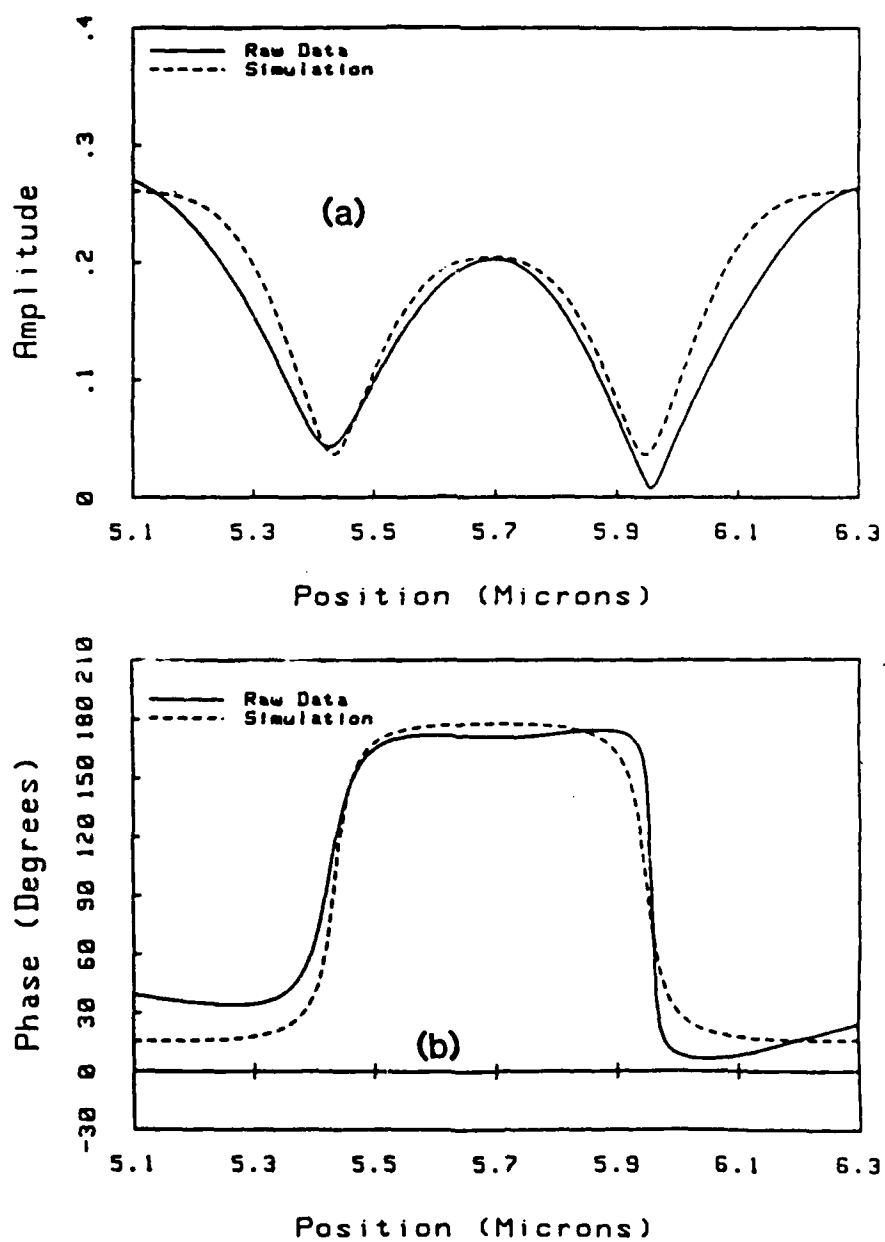


Fig. 3. Scan of a 160 nm thick by 610 nm wide Ti-Au line on silicon: (a) amplitude, (b) phase.

amplitude and phase information is available, a Fourier transform of the line scan can be taken, and inverse filtering processes carried out. In one example, the 10-90% definition was shown to be improved to 130 nm, with similar results for gratings and for finite width strips.

The Scanning Optical Microscope

We have mainly been concentrating on optical methods in the last few years, because the developments in our own and other laboratories of the *Confocal Scanning Optical Microscope* (CSOM), in addition to providing noncontacting, nondestructive methods of measurement, make it possible to measure depth and width at the same time with submicron resolutions. The transverse resolution is better than that of a standard optical microscope using the same lens. Optical techniques do not damage the material, they offer great flexibility, and are easy to use. Unlike the electron microscope, the optical techniques do not require a vacuum and it is easy to carry out sectioning, nondestructively, to obtain information on features at different depths in the interior of a translucent material or to find the profile of surface features. Confocal scanning microscopy, because of its excellent range and transverse definitions, can provide a facility for optical "cross-sectioning" that allows glare-free fluorescence imaging of fine biological structures and imaging of internal features in translucent materials.

New tools, with submicron resolution, are much needed for nondestructive measurements of small structures in semiconductors, integrated circuits, magnetic recording heads, and micromachined samples. The same tools are of great importance to manufacturing technology because they will make it possible to carry out precision metrology and detect faults in parts during the manufacturing process. Since they employ noncontacting, nondestructive methods, they can perform a large number of measurements in a short time. The basic principle of the scanning optical microscope is shown in Fig. 4. Light passes through a pinhole to a microscope objective lens and the pinhole is imaged on the object. The light reflected from the object passes through the objective lens and back through the pinhole. If the object is moved out of focus, the reflected light reaching the pinhole is defocused and the light does not pass through it. Consequently, if a detector is placed behind the pinhole and the amplitude of the signal received varies rapidly with the defocus distance z , the distance $d_z(3\text{ dB})$ between 3 dB points can be shown to be given by the approximate formula:¹²

$$d_z = \frac{0.45\lambda}{1 - \cos \theta_0}$$

where $\sin \theta_0 = \text{N.A.}$ is the numerical aperture of the lens.

Typically, with a wide aperture lens, the 3 dB points of this response are only 0.5 μm apart. At the same time, the transverse response of this microscope tends to be better than that of a standard optical microscope because the lens is used both on transmit and on receive. Consequently, the point spread function is squared, the spatial frequency response is doubled, and the 3 dB width of the transverse response is decreased by a factor of 0.7 from that of a standard microscope using the same lens. Either a laser source or an incoherent source can be used, since the sidelobe level of the response is so low that speckle caused by interference from regions outside the focused spot is no longer a problem.

We have constructed a scanning optical microscope based on this principle. We mechanically scan the object and construct a raster image which is stored in a computer and then displayed as a video image. It takes a few seconds to form one frame.¹¹ We have also constructed an optical range finder using the same technique.⁴ Results taken with both devices are described in the Appendix.

Towards the end of the program we devised new techniques for scanning differential contrast microscopy.¹⁰ These techniques are described in the Appendix. The basic purpose behind these techniques is to get a better definition of edges and of heights by using differential methods. When the object is moved in a direction z , the output in amplitude passes through a maximum. Obviously, it would be easier to find where this maximum is and on which side of the maximum the focus is by differentiating the curve. A very simple way of doing this is to move the object back and forth periodically at a frequency Ω . The signal output at this frequency Ω will essentially be the differential of the intensity as a function of distance. A better way to do this, which does not require mechanical movement, is to use an electro-optic cell made of PLZT and modulate the phase of the wave passing through the cell using transparent electrodes. This technique is somewhat equivalent to a Zernike microscope but has better contrast and better definition. Results obtained with this method are described in reference 10 in the Appendix.

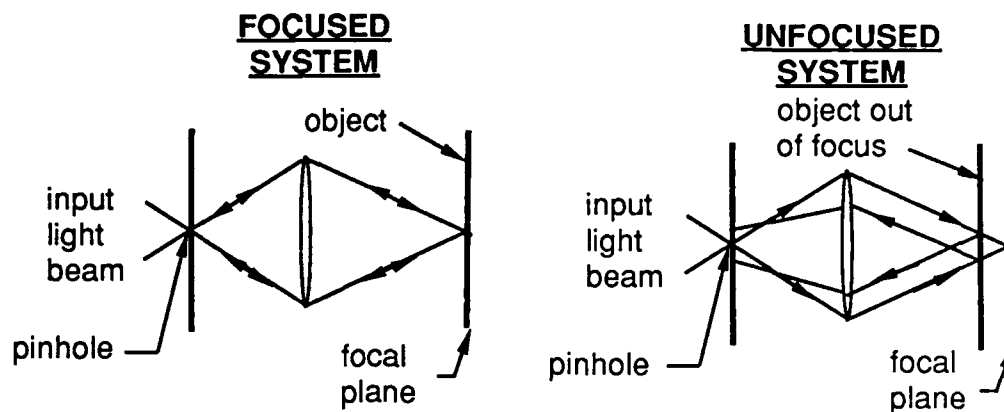


Fig. 4. An illustration of the principles of confocal microscopy.

A second technique involves using a Bragg cell with two spots placed side by side and moved with each other. This can give a differential output with respect to transverse position. Such a technique is very useful for measuring slope or the position or sharp edges.

Since the AFOSR program was on a cost-free extension from December 1986 to September 1987, this work was placed on another program in December 1986.

CONCLUSIONS

The work described here describes major advances in both acoustic and optical microscopy. New techniques for directly measuring phase and its range have been demonstrated. The use of these techniques gives excellent transverse definition, along with good range definition. The work is continuing on other programs and the new developments in optical microscopy have excited a great deal of interest in the semiconductor industry.

PUBLICATIONS

1. K. Liang, G. S. Kino, and B. T. Khuri-Yakub, "Application of Acoustic Microscopy to Surface Profiling and Material Characterization," Proc. IEEE Ultrasonics Symp. (1984).
2. K. K. Liang, G. S. Kino, and B. T. Khuri-Yakub, "Material Characterization by the Inversion of $V(z)$," IEEE Trans. on Sonics & Ultrasonics SU-32 (2) (March 1985).
3. K. K. Liang, S. D. Bennett, and G. S. Kino, "Precision Phase Measurement with Short Tone Burst Signals in Acoustic Microscopy," Rev. Sci. Instrum. 57 (3) (March 1986).
4. P. C. D. Hobbs, R. L. Jungerman, and G. S. Kino, "A Phase Sensitive Scanning Optical Microscope," Proc. of SPIE, Micron and Submicron Integrated Circuit Metrology 565 (1985).
5. P. C. D. Hobbs, "A Simple Expression for the Line Spread Function of a Confocal or Incoherent Microscope," J. Opt. Soc. Am. (Sept. 1985).
6. G. S. Kino, B. T. Khuri-Yakub, J. D. Fox, R. L. Jungerman, P. C. D. Hobbs, K. K. Liang, and R. G. Stearns, "Scanned Microscopy Techniques," Presented at the 14th Symp. on Acoustic Imaging, The Hague, The Netherlands (April 1985).
7. C-H. Chou and G. S. Kino, "The Evaluation of $V(z)$ in a Type II Reflection Microscope," IEEE Trans. on UFFC UFFC-34 (3) (May 1987).
8. T. R. Corle, C-H. Chou, and G. S. Kino, "Depth Response of Confocal Optical Microscopes," Opt. Lett. 11, 770 (December 1986).
9. G. Q. Xiao, D. B. Patterson, and G. S. Kino, "Optical Range Sensor," in Review of Progress in Quantitative Nondestructive Evaluation, Vol. 6A, Eds: D. O. Thompson and D. E. Chimenti (Plenum, 1987).
10. G. S. Kino, T. R. Corle, P. C. D. Hobbs, and G. Q. Xiao, "Optical Sensors for Range and Depth Measurements," Presented at ICALEO, Arlington, VA (November 1986).

11. T. R. Corle, J. T. Fanton, and G. S. Kino, "Distance Measurements by Differential Confocal Optical Ranging," *Appl. Opt.* 26 (12) (15 June 1987).
12. G. S. Kino, P. C. D. Hobbs, and T. R. Corle, "Phase Measurements with a Type 2 Microscope," *Proc. SPIE* 749, Metrology: Figure and Finish (1987).
13. P. C. D. Hobbs, "High-Performance Amplitude and Phase Digitizers at 60 MHz," *Rev. Sci. Instr.* 58 (8), 1518 (August 1987).

REFERENCES

1. K. K. Liang, S. D. Bennett, B. T. Khuri-Yakub, and G. S. Kino, "Precise Phase Measurements with the Acoustic Microscope," Invited Paper, *IEEE Trans. on Sonics and Ultrasonics* SU-32, 266-273 (1985).
2. K. K. Liang, G. S. Kino, and B. T. Khuri-Yakub, "Material Characterization by the Inversion of $V(z)$," *IEEE Trans. on Sonics and Ultrasonics* SU-32, 213-224 (1985).
3. R. L. Jungerman, P. C. D. Hobbs, and G. S. Kino, "Phase Sensitive Scanning Optical Microscope," *Appl. Phys. Lett.* 45, 846-848 (1984)
4. G. Q. Xiao, D. B. Patterson, and G. S. Kino, "Optical Range Finder," Review of Progress in Quantitative Nondestructive Evaluation, Vol. 6A, Eds: D. O. Thompson and D. E. Chimenti, Plenum Publishing Co. (1987).
5. K. K. Liang, "Precision Phase Measurements in Acoustic Microscopy," Ph.D. Dissertation, Stanford University, Stanford, CA (1985).
6. R. L. Jungerman, "Characterization of Surface Variations Using Optical Interferometry," Ph.D. Dissertation, Stanford University, Stanford, CA (February 1985).
7. P. C. D. Hobbs, "Heterodyne Interferometry with A Scanning Optical Microscope," Ph.D. Dissertation, Stanford University, Stanford, CA (August 1987).
8. K. K. Liang, S. D. Bennett, and G. S. Kino, "Precision Phase Measurements with Short Tone Burst Signals," *Rev. Sci. Instruments*, 57, 446-452 (1986)

9. P. C. D. Hobbs, R. L. Jungerman, and G. S. Kino, " A Phase Sensitive Scanning Optical Microscope," SPIE Proc. **565**, 71 (1985).
10. G. S. Kino, C-H. Chou, T. R. Corle, and P. C. D. Hobbs, "Scanning Differential Contrast Microscopy," Review of Progress in Quantitative Nondestructive Evaluation, Vol. 6B, Eds: D. O. Thompson and D. E. Chimenti (Plenum Publishing Corp. 1987).
11. P. C. D. Hobbs, "High-Performance Amplitude and Phase Digitizers at 60 MHz," Rev. Sci. Instr. **58** (8), 1518 (August 1987).
12. T. R. Corle, C-H Chou, and G. S. Kino, "Depth Response of Confocal Optical Microscopes," Opt. Lett. **11**, 770-772 (1986).

Precise Phase Measurements with the Acoustic Microscope

KENNETH K. LIANG, SIMON D. BENNETT, MEMBER, IEEE, BUTRUS T. KHURI-YAKUB, MEMBER, IEEE, GORDON S. KINO, FELLOW, IEEE

Abstract—The measurement and the use of phase in acoustic microscopy are discussed. It is demonstrated that in many applications phase can be used to provide sensitivity and information unparalleled by amplitude-only measurement methods. A technique capable of high-accuracy measurement of the phase of short RF acoustic pulses is described. The power of this phase measurement technique is illustrated in a number of applications. Surface material property measurements such as the Rayleigh-wave velocity and the inversion of the complex $V(z)$ to obtain the reflectance function of a liquid-solid interface are considered. Surface topography mapping based on phase measurement is examined. A Fourier transform approach for precision determination of linewidths comparable to the resolution spot size is also presented.

I. INTRODUCTION

THE SCANNING acoustic microscope is a high-resolution imaging system in which, unlike conventional optical microscopes, it is relatively straightforward to measure the phase of the return signal. With only a few exceptions [1]–[3], attention has centered only on the use of intensity information. In some of the main areas of application of the acoustic microscope, the phase of the received signal plays an important role. For example, in the so-called $V(z)$ measurements [4]–[7], the amplitude of the received signal $V(z)$ as a function of the separation between the lens and the substrate exhibits periodic peaks and nulls. This phenomenon is due to the beating between a specularly reflected signal from the substrate and a delayed leaky Rayleigh-wave signal, which reemits to the lens while propagating along the surface of the substrate. The phase difference between these two signal components is therefore of great importance, and in fact it controls the contrast of reflectional images. In addition, it has been shown that the independent measurement of phase and amplitude can be very useful in the determination of the elastic constants of tissue [8], [9]. However, little effort has been made to extract the phase of the return signal separately.

One reason for the reluctance to make use of the phase is that it is not generally trivial to measure the phase of a

high-frequency tone burst with sufficient accuracy. We will describe here an approach that is relatively easy to implement and capable of yielding high-precision phase data, even from very short tone bursts. The details of the phase measurement technique will be published elsewhere, and we will concentrate here on some of the applications of the system to acoustic microscopy.

There are many motivations for making measurements of this type. Firstly, they offer a direct indication of material properties as in the measurement of Rayleigh-wave velocity. Also, the results of the phase measurement can be used to infer the width and the height of surface features. Finally, the combination of amplitude and phase measurements can be used in the reconstruction processes in which complete information about the interaction between acoustic field and material is required, as in the inversion of $V(z)$ data to find the reflection coefficient as a function of angle [10].

II. PHASE MEASUREMENT SCHEME

A. Acoustic Lens Configuration

In making precise phase measurements that are related to physical properties, it is generally important to ensure that the reference signal, against which the phase of the probing signal is to be compared, and the probe itself share as many of the instrumental and environmental phase disturbances as possible. In other words, precise measurements are best done in an interferometer, where the two arms are closely matched.

In this work we have made use of two acoustic measurement configurations that largely satisfy this general condition. The first (Fig. 1(a)) is reminiscent of the defocused condition used in $V(z)$ measurements, except that here a fixed separation between the lens and the sample surface is maintained. Two components of the acoustic field returned to the lens contribute most significantly to the output signal: the on-axis specular reflection of the longitudinal wave in the water (L in Fig. 1a); and the off-axis rays (R), which satisfy the condition $v_w/v_R = \sin \theta_R$ for the conversion of longitudinal waves with velocity v_w in the water to leaky Rayleigh waves with velocity v_R on the surface of the sample [4], [5].

These two signals, L and R , differ slightly in path length in water but otherwise experience much the same environ-

Manuscript received September 1984; revised December 1984. This work was supported by the Air Force Office of Scientific Research under Contract F49620-79-C-0217.

K. Liang, B. T. Khuri-Yakub, and G. S. Kino are with the Edward L. Ginzton Laboratory, W. W. Hansen Laboratories of Physics, Stanford University, Stanford, California 94305, USA.

S. D. Bennett is with Datasonics Corp., 911 Del Avenue, Campbell, CA 95008, USA.

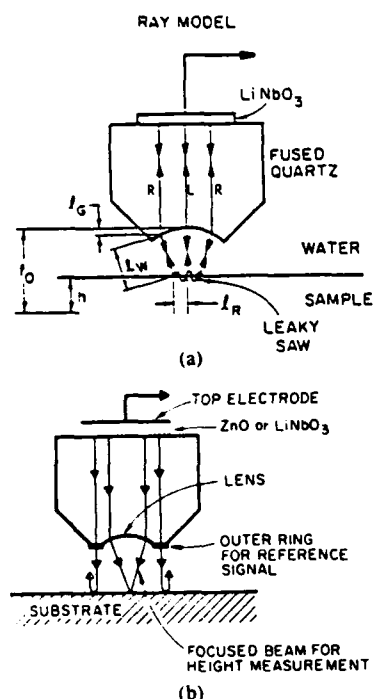


Fig. 1. Acoustic lens configurations. (a) Rayleigh-wave velocity perturbation measurement. (b) Topography mapping.

mental disturbances. However, the Rayleigh-wave component acquires substantial phase delay at the surface of the specimen, hence the effective path length for the R signal is longer than that of the specular reflection. Indeed in our experiments we use the different arrival time of these two return signals to facilitate their separation and subsequent phase comparison. The excitation signal is two to three cycles in duration, and the defocus distance is sufficient that there is no temporal overlap of the signals. It is clear that changes in the Rayleigh-wave velocity as a function of position along the surface of the specimen may be sensed in this way. By combining a high-accuracy phase measurement scheme with a suitably extended Rayleigh-wave path, remarkably sensitive measurements can be made.

The second configuration that concerns us is illustrated in Fig. 1(b). In this case the lens is positioned so that its focus is at the surface of the specimen or slightly above it so that no Rayleigh wave of importance is excited. A reference path is provided by an annular beam that propagates through the flat outer periphery of the lens. By exciting the lens with a short pulse, and once again using time discrimination to separate the signals from the two different paths, an interferometer is formed. Now small local changes in the surface topography result in large changes in the phase of the focused beam relative to the phase of the large diameter reference beam.

In both measurement configurations it is apparent that the signals of interest arrive at different times, and this would ordinarily make phase comparison impossible. However, the electronic system described in the next section essentially reconstructs two phase-coherent continu-

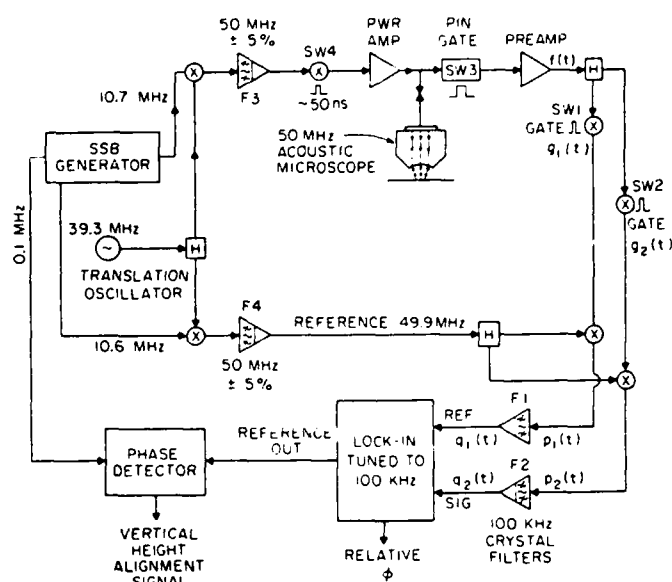


Fig. 2. Schematic for the phase measurement system.

ous signals that are directly related to the amplitudes and phases of the two time-distinct return signals.

The first configuration is also used where the signal of interest is the transducer output voltage, when the system is operated in the $V(z)$ mode. In this case the exciting signal has a much longer duration so that the return signals (L and R) overlap and interfere at the transducer even for large defocus distances. The idea here is to measure both the amplitude and the phase of the signal relative to some reference as a function of the axial separation z between the acoustic lens and the specimen. The resulting complex $V(z)$ can be inverted [10] to obtain the angular dependence of the reflectance of the liquid-specimen interface. From the reflectance function, various material property parameters can readily be extracted.

In the experiments described here, a center frequency of 50 MHz was used with an acoustic transducer having a bandwidth of 20 percent. The lens material was fused quartz and had a radius of curvature of 3.2 mm, giving a focal length in water of 4.24 mm. The opening aperture of the lens was 5.0 mm in diameter, corresponding to a maximum half angle of 36° or an f -number of 0.85.

Providing the same fractional bandwidth can be maintained, there should be little difficulty in applying the same techniques to a system operating at much higher frequency, perhaps up to 2 GHz. Beyond that frequency, limitations in the electronic-switching components presently available may present difficulties.

B. Electronics

The essential elements of the phase measurement electronics are shown schematically in Fig. 2. The system will be described in detail in a forthcoming paper [18], where various sources of error and an analysis of the ultimate performance are discussed. A more general review of the concepts will suffice here.

The basic scheme involves signal recovery by synchronous detection and subsequent phase measurement with a lock-in amplifier. The key component (Fig. 2) in the signal source is the single sideband generator (SSB) with synchronous outputs at 100 kHz, 10.6 MHz, and 10.7 MHz. The 10.7-MHz output is in fact the upper sideband of the product of the 100 kHz and 10.6-MHz signals. The lower sideband at 10.5 MHz is suppressed by at least 50 dB using a standard FM radio system IF filter. The translation oscillator shifts the operating frequency up to the desired center frequency of the acoustic system, which is 50 MHz in this case. A reference signal at 49.9 MHz is also generated. Again the lower sideband components of the product signals have to be removed. At this point however the filtering requirements are not as stringent as in the SSB generator and tunable bandpass filters (F3 and F4) with five-percent bandwidth are adequate, since the sidebands are now widely separated. This signal generation scheme is flexible in that the operating frequency is tunable over a fairly wide range, which is limited in this case to 100 MHz by the bandpass filters. For much higher frequency of operation, filters with greater selectivity would be needed or, alternatively, successive stages of heterodyning could be used with filtering at each stage to step up incrementally to the desired operating frequency.

As illustrated in Fig. 2 with a 50-MHz acoustic microscope, the 50-MHz continuous wave (CW) signal is time-gated to produce a short tone burst that excites the acoustic transducer. Switch SW3 is used as a time gate to pass the low-level acoustic return signals of interest and to block high-level extraneous ones, which may damage the preamplifier. The acoustic return signals are time-separated RF pulses, and they are electronically separated through time-gating into two channels as shown. Each of the resulting signals is mixed with the 49.9 MHz reference signal, and the product is narrow-band filtered to extract the 100-kHz component.

It can be shown [18] that the 100-kHz signals are essentially low-frequency CW replicas of the pulse modulated RF acoustic signals, bearing identical phase and amplitude information. With a biphasic lock-in amplifier tuned to 100 KHz, one can readily measure the phase difference between the two signals and also the amplitude of the signal being fed to the "signal" channel of the lock-in, if it is required. Phase sensitivity is basically limited by the lock-in amplifier because the problem of system noise can in most cases be overcome by increasing the integration time in the lock-in output stage. This effectively reduces the system noise bandwidth, but it also includes the obvious disadvantage of longer data acquisition time. Good-quality lock-in amplifiers routinely have phase resolution of the order of 0.1° , which corresponds to an overall system phase sensitivity of $1/3600$ of a wavelength.

In velocity perturbation measurements the measured phase is dependent on the distance between the lens and the specimen. This distance changes with the sample surface topography and is susceptible to thermal drift as well,

thus introducing phase error into the measurement. To minimize this error, a feedback mechanism is employed to keep the lens-to-specimen spacing constant. The acoustic lens is mounted on a piezoelectric (PZT) stack so that its vertical position can be adjusted continuously by an electronic control signal. The acoustic on-axis reflection pulse, whose phase is a direct measure of the lens to sample distance, is applied to the reference channel of the lock-in amplifier as shown in Fig. 2. The reference channel generates a 100-kHz constant-amplitude phase-locked replica of the reference input, which is then compared with the 100-kHz output of the SSB generator to produce the control signal for the PZT stack. The acoustic lens automatically tracks the surface topography of the sample during scanning to ensure that the measured phase change is due to material property variation alone. This feedback mechanism is also used effectively in such modes of operation as topography measurement to compensate for thermal effects.

III. APPLICATIONS

The power of this measurement scheme is illustrated in the following with a number of examples. We will consider both material property measurements, such as Rayleigh-wave velocity and complex reflectivity, and surface topography measurements.

A. Velocity Perturbation Measurements

In this section we will specifically deal with the perturbation to the Rayleigh-wave propagation velocity as a result of material property change and also the presence of surface residual stress.

1) *Velocity Perturbation Due to Thin-Film Overlay:* The sample in this example is a multiple-thickness indium film deposited on glass. The thicknesses are 240 Å and 620 Å, respectively. The objective was to measure the perturbation of the Rayleigh-wave velocity caused by the indium film. A line scan over the surface of the sample (Fig. 3) exhibits phase changes of 7° and 11° for the 240-Å and 380-Å step changes in film thickness. The spatial resolution of the system is defined by the Rayleigh-wave path length on the substrate and is determined to be about 0.8 mm from the step transition width in the line scan. It can be calculated from first order perturbation theory [11] that the velocity perturbation due to the indium film is 0.18 percent and 0.46 percent for the 240-Å and 620-Å layers, respectively. Based on these estimated parameters, one would expect phase changes of 7.6° and 12° for the 240-Å and 380-Å step transitions. Hence there is fairly good agreement between the experimentally obtained and theoretically predicted phase changes. It should also be noted that in the line scan, the small phase variations in the supposedly flat regions of the indium film are real and repeatable. The fluctuations are less than 0.5° and are due to nonuniformity in the thickness of the indium film. Since the phase sensitivity of the system is limited by the lock-in amplifier to 0.1° , this measurement technique can po-

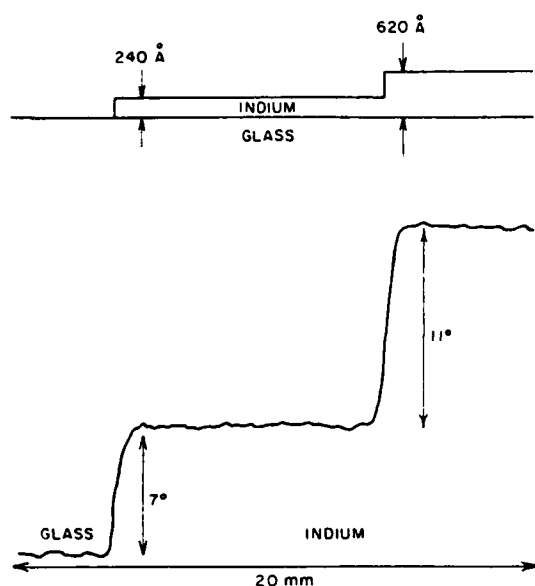


Fig. 3. Measurement of velocity perturbation due to indium film on glass.

tentially detect velocity perturbations on the order of one part in 10^5 .

2) *Residual Stress Measurement*: In nondestructive testing, knowledge of the surface residual stress distribution in a component plays an important role in the prediction of failure modes. One way of characterizing residual stress is by measuring the acoustic wave propagation velocity, which varies linearly with the local stress [12]. With the measurement configuration shown in Fig. 1(a) the measured change in the relative phase between the *L* and *R* signal pulses as the lens is scanned can be shown to be directly proportional to the residual stress on the object surface [13].

The sample used in the experiment is a glass disk of two inches in diameter that was heated and then thermally quenched with air jets to introduce a radial distribution of residual stress. Fig. 4(b) shows the radial variation of the measured phase perturbation. For comparison a destructive test was carried out on a similar sample to determine the actual residual stress distribution. A Vicker's indenter was used at a prescribed load to produce median cracks at different points on the glass disk. By measuring the crack lengths, the residual stress as a function of radial distance was calculated [14]. The result of the destructive test is shown in Fig. 4(a). The variation of the principal stresses are essentially the same, with the radial and tangential components tracking each other to within 20 MPa. Since the phase measurement is omnidirectional in that a spherical lens was used to launch Rayleigh waves propagating in all directions along the surface, the resulting phase perturbation is a measure of the sum of the principal stresses. Comparison of Figs. 4(a) and 4(b) shows that there is fairly good corroboration between the phase perturbation curve and the actual residual stress distribution. From these results we empirically deduce that 40 MPa of stress, which is the change from the center of the sample to the

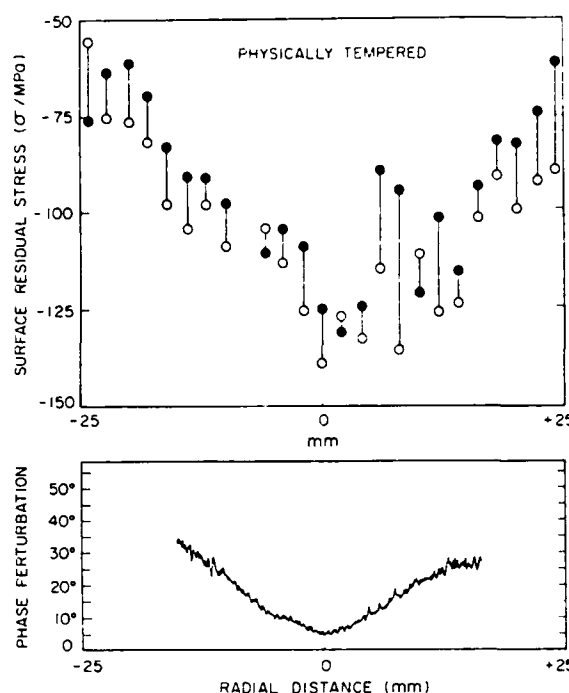


Fig. 4. Residual stress measurements on the surface of a tempered glass disk. (a) Variation of radial (open symbols) and tangential stresses (closed symbols) across a diameter of the glass disk estimated from indentation fracture tests. (b) Radial variation of measured phase perturbation.

limit of the line scan, corresponds to a phase variation of 30° .

B. Surface Topography Measurements

We have used the acoustic microscope in the measurement configuration shown in Fig. 1(b) as a high-resolution noncontacting profilometer [13], [15]. Besides being able to make use of phase profile to map the depth variation, we can also determine with high precision the transverse profile of surface features in special cases. Of particular interest in this regard is the measurement of the widths of long rectangular strips, which is a matter of great concern in the fabrication of semiconductor components. We will show here both experimentally and theoretically the advantages of utilizing phase to determine the linewidth. We will also introduce here a Fourier transform technique for linewidth measurement in cases where the strip width is comparable to the spot size.

1) *Depth Profiling*: Topography images of metallized stripe patterns on a fused-silica substrate are shown in Figs. 5(a), 5(b), and 5(d). The patterns have progressively finer pitches and the linewidths are 250, 125, and 62.5 μm , respectively. The metallization is gold with a thickness of about 3000 Å. The gold stripes show up as bright areas in the images. At 50 MHz, with an f-number of 0.85 and a uniformly excited aperture, the Rayleigh resolution of the acoustic lens is $1.13 F\lambda = 0.96 \lambda$ or 29 μm , while the 3-dB resolution is $0.64 F\lambda = 0.54 \lambda$ or 16 μm . The 62.5- μm line image in Fig. 5(d) is clearly resolved, as would be expected. The amplitude image of the 125- μm stripes is shown in Fig. 5(c) for comparison. There is vir-

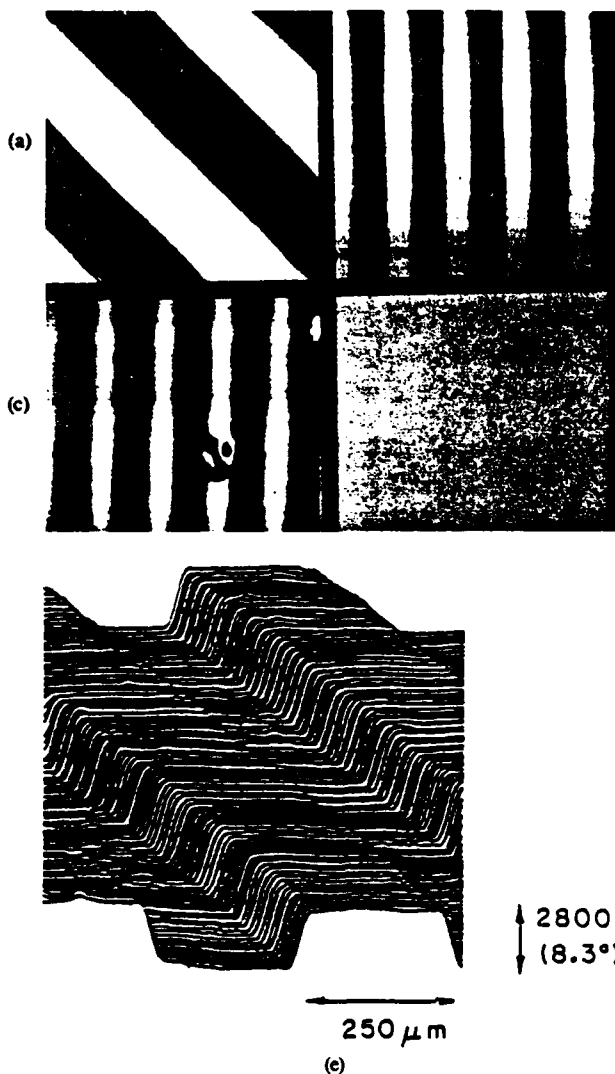


Fig. 5. Topography images of striped metallization patterns on a fused quartz substrate. The metallization is gold and the thickness is about 3000 Å. (a) Phase image of 250- μ m lines. (b) Phase image of 125- μ m lines. (c) Amplitude image of 125- μ m lines. (d) Phase image of 62.5- μ m lines. (e) Perspective plot of the measured topography map of the 250- μ m line pattern.

tually no contrast to suggest the presence of a striped pattern, clearly illustrating that phase is a far more sensitive means of gauging distances. The measured phase difference between the surface of the metallization and the surface of the fused-silica substrate is 8.3° , which corresponds to a film thickness of 2800 Å after taking into account the angular dependence of the complex reflectance function and the effect of focusing.

We will show here that, based on theoretical considerations, indeed the phase rather than the magnitude of the acoustic microscope output $V(x)$ is a more sensitive measure of the depth profile. Consider the simple case of a rectangular strip of width w on a substrate of identical material. Assume that the reflection coefficient Γ_0 of the surface is real. Then the spatial response of the strip structure is given by

$$R(x) = \Gamma_0 + \Gamma_0 (e^{j\phi} - 1) \text{rect}(x/w) \quad (1)$$

where ϕ is the phase change due to the thickness of the strip. Let the response of the imaging system to a line source be $h(x)$. Furthermore, suppose that the lens is uniformly illuminated in the back focal plane and the lens is aberration-free so that $h(x)$ is real. The acoustic microscope output is therefore given by

$$V(x) = R(x) * h(x) \quad (2)$$

or

$$V(x) = \Gamma_0 K + \Gamma_0 (e^{j\phi} - 1) s(x) \quad (3)$$

where

$$s(x) = h(x) * \text{rect}(x/w) \quad (4)$$

and

$$K = \int_{-\infty}^{+\infty} h(x) dx.$$

The first term on the right-hand side of (3) corresponds to the constant background reflection from the substrate, and the second term corresponds to the additional spatially varying contribution that is due to the strip. It can easily be shown that for a thin strip where $\phi \ll 1$, to second order in ϕ , the magnitude and the phase of $V(x)$ are given respectively by the relations

$$V_{\text{mag}}(x) = \Gamma_0 K + \frac{\Gamma_0 s(x)}{2} [s(x) - K] \phi^2 \quad (5)$$

and

$$V_{\text{phase}}(x) = \frac{\phi}{K} s(x). \quad (6)$$

The $V_{\text{phase}}(x)$ is directly proportional to ϕ , whereas the spatially varying part of $V_{\text{mag}}(x)$ depends on ϕ to the second order. Thus for thin strips, phase is a much more sensitive measure of the depth profile.

2) *Linewidth Measurement:* A major advantage of scanned confocal imaging systems such as ours is that because the point spread function is always positive and falls off rapidly at large distances, there is hardly any ripple in the amplitude of the step response [16], [17]. A similar smooth transition in the phase of the step response can also be observed in the perspective plot shown in Fig. 5(e). For the purpose of comparison, we have carried out a numerical analysis for the step phase responses of different imaging configurations. For small step heights, or equivalently small phase changes, the normalized phase step response is of the form

$$\beta(x) = \int_x^\infty g(r) \cos^{-1}(x/r) r dr \quad (7)$$

where x is the distance between the center of the beam and the step, and $g(r)$ is the point response function of the imaging system. It is assumed that regions on either side of the step are of equal reflectivity. The step response function is plotted in normalized form in Fig. 6 for two

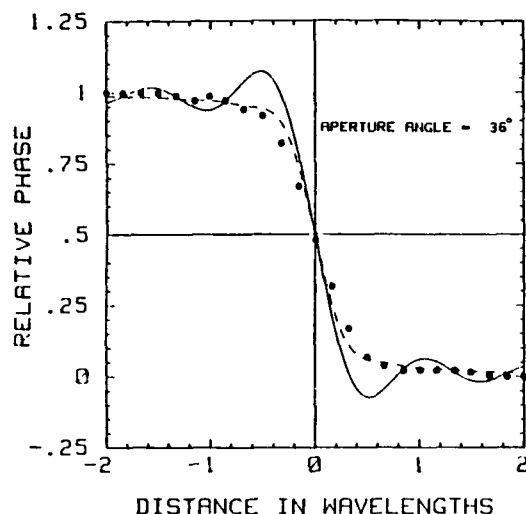


Fig. 6. Step phase response of a normal phase interference microscope (solid curve) and a confocal imaging system (theory in dashed curve, experimental result in closed circles).

different cases. The solid curve corresponds to $g(r) = \text{jinc}(2r \sin \theta/\lambda)$, which is the point response of a normal phase interference microscope where the illumination is a plane wave. Here θ is the maximum half angle of the objective lens; λ is the wavelength of the illumination; and $\text{jinc}(x)$ is defined as $2J_1(\pi x)/\pi x$. Note that in this case $g(r)$ reverses in sign and its corresponding step phase response does not change monotonically with distance. The dashed curve corresponds to $g(r) = \text{jinc}^2(2r \sin \theta/\lambda)$, the point response of a confocal system. The confocal response shows a distinct lack of ripples. The experimentally measured step phase response is also plotted in closed circles showing close agreement with theory. In both imaging configurations, the 50-percent threshold of the phase profile demarcates the location of the edge. It is obvious, however, that the smooth transition of the confocal step phase response enables a straightforward and unambiguous determination of not only the strip thickness but also the strip width.

The 50-percent threshold criterion used to locate the edges of a strip for estimating the linewidth is a valid one for wide strips. For strip widths comparable to the spot size of the imaging system, the step responses of the two edges are in close proximity and tend to interfere with each other, making the establishment of a general criterion for locating the strip edges difficult. We will describe here a Fourier-transform method that circumvents these difficulties.

Applying Fourier transform to (6) and using the definition of $s(x)$ in (4), the spatial frequency spectrum of $\tilde{V}_{\text{phase}}(f_x)$ is given by

$$\tilde{V}_{\text{phase}}(f_x) = \frac{\phi}{K} H(f_x) \cdot w \text{sinc}(wf_x) \quad (8)$$

where $H(f_x)$ is the Fourier transform of $h(x)$. The term with the sinc function corresponds to the Fourier trans-

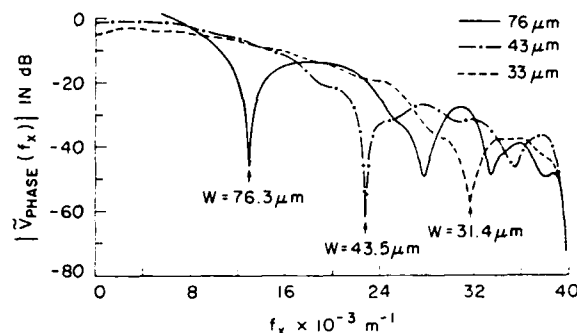


Fig. 7. Spectral responses of 5000-Å-thick gold lines on a fused-quartz substrate. The nominal linewidths are 76 μm , 43 μm , and 33 μm , respectively.

form of the spatial variation of the strip and its zeroes are located at

$$f_x = n/w, \quad n = 1, 2, 3, \dots \quad (9)$$

The term $H(f_x)$ represents the angular spectral response of the imaging system. For a confocal system $|H(f_x)|$ is maximum at $f_x = 0$ and generally falls off monotonically, until it becomes zero at the upper cutoff frequency of

$$f_{x\text{max}} = 1/(F\lambda)$$

where F is the f-number of the lens, and λ is the wavelength of the illumination [16], [17]. Hence the zeroes of $\tilde{V}_{\text{phase}}(f_x)$ are those of the strip response within the pass-band of the imaging system. As long as

$$w > F\lambda \quad (10)$$

the strip width w can be determined using (8) from the locations of the zeroes of $\tilde{V}_{\text{phase}}(f_x)$. In our case $F = 0.85$, so in principle we can determine linewidths as small as 0.85λ or 25 μm at 50 MHz in water.

The merit of this Fourier-transform technique lies in its simplicity. Given *a priori* knowledge of the strip geometry, one does not need to know the exact nature of imaging system. The mere location of the zeroes for the spectral response of the object suffices for the accurate determination of the linewidth.

Fig. 7 illustrates the experimental $|\tilde{V}_{\text{phase}}(f_x)|$ for $w = 76 \mu\text{m}$, 43 μm , and 33 μm , respectively. The strips are 5000-Å-thick gold lines on a fused-quartz substrate. The acoustic microscope operates at 50 MHz ($\lambda = 30 \mu\text{m}$) with $F = 0.85$, and the acoustic beam is focused on the surface of the fused-quartz substrate. The $|\tilde{V}_{\text{phase}}(f_x)|$ is plotted on a log scale. The weighting due to the imaging system response $|H(f_x)|$ all the way out to the resolution limit is very much in evidence. The linewidths estimated from the position of the first zero of $\tilde{V}_{\text{phase}}(f_x)$ are 76.3, 43.5, and 31.4 μm , respectively. They agree very well with the optically measured widths. The minor discrepancies are mainly due to the nonuniformity in the widths of the gold lines.

In addition, this Fourier transform approach is essentially insensitive to defocusing. It is obvious from (8) that

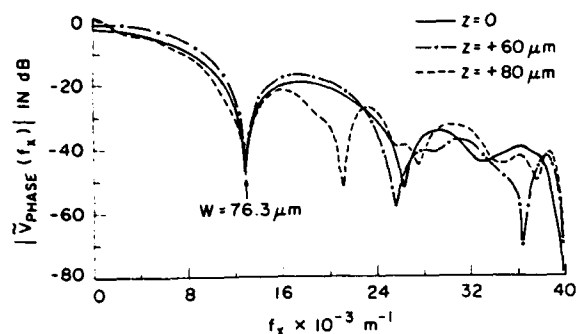


Fig. 8. Spectral responses of 2000-Å-thick 76-μm-wide chrome line on a fused quartz substrate at various defocusing distances: $z = 0$ μm, +60 μm, and +80 μm, respectively.

defocusing only changes the spectral response of the imaging system $H(f_x)$ slightly and does not introduce any new zeroes to nor does it affect the zeroes of $|\tilde{V}_{\text{phase}}(f_x)|$. Fig. 8 shows the experimental $|\tilde{V}_{\text{phase}}(f_x)|$ for a 2000-Å-thick and 76-μm-wide chrome line on fused quartz at various defocusing distances. The focus was located on the substrate, and 60 μm and 80 μm above the substrate, respectively. The locations of the first zero in all three cases are essentially coincident, giving a width estimate of 76.3 μm.

3) *Independent Measurement of Velocity Perturbation and Topography:* In conventional acoustic micrographs, surface topography and material property both contribute to contrast in the image, and their respective effects are generally indistinguishable from one another. With the topography tracking mechanism described in Section II-2 built into our phase measurement system, surface topography and material property change can essentially be obtained independent of each other.

Fig. 9(a) is the topographic line scan of an aluminum film step on glass with a nominal thickness of 5000 Å. The initial and trailing slow phase changes are due to the large spatial extent of the reference signal as it traverses the step, whereas the abrupt phase change is due to the focused beam as it crosses the step. Fig. 9(b) is the same profile on an expanded scale. The phase change caused by the step is 11.25°, which corresponds to a thickness of 4688 Å. With a limiting phase resolution of 0.1°, the ultimate height sensitivity of the system is about 50 Å.

Fig. 9(c) shows a velocity perturbation scan of the same sample. The phase change measured is 7.75°, corresponding to a velocity perturbation of 0.25 percent, which is in fair agreement with the theoretically calculated value of 0.21 percent.

C. Reflectance by Inversion of Complex $V(z)$

It has been demonstrated that the reflectance function at a liquid-solid interface can be obtained by inverting the corresponding complex $V(z)$ data [10]. The principle motivation behind this endeavor is that one can obtain much more useful material property information from the reflectance function than the usual and rather limited treatment of measuring the periodicity of the nulls in the $V(z)$

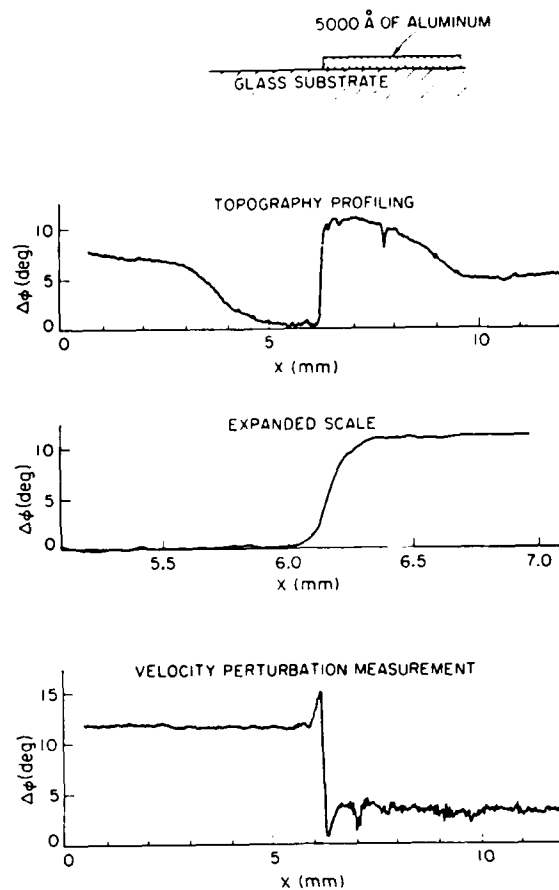


Fig. 9. Independent measurements of velocity perturbation and topography profile due to a 5000-Å aluminum film step. (a) Topography profile scan. (b) Topography profile scan on an expanded scale. (c) Velocity perturbation scan.

curve to determine only the Rayleigh-wave velocity. The solid curves in Fig. 10 show the magnitude and the phase of the theoretical reflectance function of a water-fused-silica interface. The reflectance function contains information on the longitudinal and shear critical angles, and thus the velocities of propagation of the respective modes in fused silica. Also, the Rayleigh critical angle corresponds to the point at which the phase is π radians in the region, where the phase curve undergoes a rapid 2π radian change.

It can be shown that the relation between $V(z)$ and the reflectance function $R(\theta)$ is essentially one of Fourier transformation [10]. The inversion formula is given by

$$R(t) = \frac{\mathcal{F} \{ V(u) \exp [j\pi u \sin^2 (\alpha/2)] \}}{[U_1^+(t)]^2 P^2(t) [1 - 2t \sin^2 (\alpha/2)]} \quad (11)$$

where

$$u = \frac{4z \sin^2 (\alpha/2)}{\lambda}$$

and

$$t = \frac{\sin^2 (\theta/2)}{\sin^2 (\alpha/2)}.$$

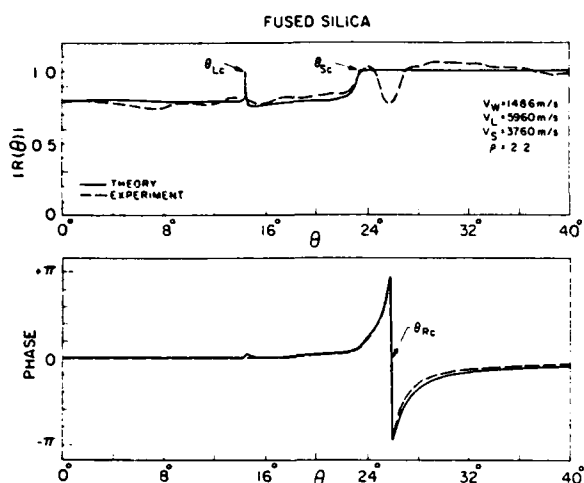


Fig. 10. Theoretical and experimental reflectance function for a water-fused-quartz interface obtained by inversion of the corresponding complex $V(z)$.

The α is the maximum half angle of the lens; θ is the incident angle with respect to the liquid-solid interface; and λ is the wavelength of the acoustic wave in the liquid medium. In addition, U_1^+ is the back focal plane illumination, and P is the pupil function of the lens. Generally these two lens parameters are not known, but $[U_1^+]^2 P^2$ in the denominator of (11) can be calibrated by measuring the $V(z)$ for a material whose reflectance function has uniform amplitude and phase over the range of angular spectral components excited by the acoustic lens.

The $V(z)$ measurements were conducted at 10 MHz. A water-lead interface, in which the reflectance function is uniform in magnitude and phase out to $\theta = 40^\circ$, was used to calibrate the $[U_1^+]^2 P^2$ term. The experimental reflectance function of fused silica, obtained from the inversion procedure, is superposed on Fig. 10 in dashed lines. There is good agreement between theory and experiment in both magnitude and phase. The measured shear critical angle at $\theta = 23.5^\circ$ and the Rayleigh critical angle at $\theta = 25.85^\circ$ compare extremely well with theoretical values.

IV. CONCLUSION

We have demonstrated that phase information is a useful asset in acoustic microscopy. Phase can be used to provide sensitivity and information in surface material characterization unparalleled by amplitude-only measurement techniques. Most of the concepts described in this work have complete generality and can readily be used in other applications. In fact, many ideas presented in this work have been applied to a new scanning optical microscope [19] developed by Jungerman and Kino for surface topography measurement. In the optical case both the amplitude and the phase of the reflected beam can be measured as in the acoustic microscope. Preliminary results from the scanning optical microscope give further confirmation of most of the concepts put forth in this paper.

REFERENCES

- [1] H. K. Wickramasinghe and M. Hall, "Phase imaging with the scanning acoustic microscope," *Electron. Lett.*, vol. 12, pp. 637-638, Nov. 1976.
- [2] C. C. Lee, C. S. Tsai, and X. Cheng, "Complete characterization of thin- and thick-film materials using wideband reflection acoustic microscopy," *IEEE Trans. Sonics Ultrason.*, vol. SU-32, no. 2, pp. 248-258, Mar. 1985.
- [3] S. D. Bennett and E. A. Ash, "Differential imaging with the acoustic microscope," *IEEE Trans. Sonics Ultrason.*, vol. SU-28, pp. 59-69, 1981.
- [4] A. Atalar, "An angular spectrum approach to contrast in reflection acoustic microscopy," *J. Appl. Phys.*, vol. 49, pp. 5130-5139, Oct. 1978.
- [5] H. K. Wickramasinghe, "Contrast and imaging performance in the scanning acoustic microscope," *J. Appl. Phys.*, vol. 50, pp. 664-668, Feb. 1979.
- [6] R. D. Weglein, "Metrology and imaging in the acoustic microscope," in *Scanned Image Microscopy*, E. A. Ash, Ed. London: Academic, 1980.
- [7] J. Kushibiki and N. Chubachi, "Material characterization by line-focus-beam acoustic microscopy," *IEEE Trans. Sonics Ultrason.*, vol. SU-32, no. 2, pp. 189-212, Mar. 1985.
- [8] I. R. Smith, D. A. Sinclair, and H. K. Wickramasinghe, "Acoustic microscopy of elastic constants," in *Proc. 1980 IEEE Symp. Sonics Ultrason.*, Boston, MA, Oct. 1980.
- [9] D. A. Sinclair and I. R. Smith, "Tissue characterization using acoustic microscopy," in *Acoustic Imaging*, vol. 12, E. A. Ash and C. R. Hill, Ed. New York: Plenum, 1982.
- [10] J. A. Hildebrand, K. Liang, S. D. Bennett, "Fourier transform approach to material characterization with the acoustic microscope," *J. Appl. Phys.*, vol. 54, no. 12, pp. 7016-7019, Dec. 1983.
- [11] B. A. Auld, *Acoustic Fields and Waves in Solids*, vol. 2. New York: John Wiley & Sons, 1973, p. 278.
- [12] D. Husson and G. S. Kino, "A perturbation theory for acoustoelastic effects," *J. Appl. Phys.*, vol. 53, p. 7250, Nov. 1982.
- [13] K. Liang, S. D. Bennett, B. T. Khuri-Yakub, and G. S. Kino, "Precision measurement of Rayleigh wave velocity perturbation," in "DARPA/AF Review of Progress in Quantitative NDE," La Jolla, CA, Aug. 1982.
- [14] D. B. Marshall and B. R. Lawn, "Measurement of nonuniform distribution of residual stresses in tempered glass disks," *Glass Tech.*, vol. 19, no. 3, June 1978.
- [15] K. Liang, S. D. Bennett, B. T. Khuri-Yakub, and G. S. Kino, "Precision measurement of Rayleigh wave velocity perturbation," *Appl. Phys. Lett.*, vol. 41, no. 12, pp. 1124-1126, 1982.
- [16] R. A. Lemons, "Acoustic microscopy by mechanical scanning," Ph.D. Thesis, Stanford University, Stanford, CA, 1975.
- [17] J. W. Goodman, *Introduction to Fourier Optics*. New York: McGraw-Hill, 1968.
- [18] K. Liang, S. D. Bennett, and G. S. Kino, "Precision phase measurement for acoustic microscopy," to be submitted to *Rev. Sci. Instr.*
- [19] R. L. Jungerman, P. C. D. Hobbs, and G. S. Kino, "Phase sensitive scanning optical microscope," submitted to *Appl. Phys. Lett.*, vol. 45, pp. 846-848, Oct. 1984.

Kenneth K. Liang, for a photograph and biography please see page 223 of the March 1985 issue of this TRANSACTIONS.

Simon D. Bennett (S'73-M'78), for a photograph and biography please see page 131 of this TRANSACTIONS.

Butros T. Khuri-Yakub, (S'70-M'76) for a photograph and biography please see page 224 of the March 1985 issue of this TRANSACTIONS.

Gordon S. Kino (S'52-A'54-SM'63-F'66), for a photograph and biography please see page 224 of the March 1985 issue of this TRANSACTIONS.

Material Characterization by the Inversion of $V(z)$

KENNETH K. LIANG, GORDON S. KINO, FELLOW, IEEE,
AND BUTRUS T. KHURI-YAKUB, MEMBER, IEEE

Abstract—It is demonstrated that the reflectance function $R(\theta)$ of a liquid-solid interface can be obtained by inverting the complex $V(z)$ data collected with an acoustic microscope. The inversion algorithm is based on a nonparaxial formulation of the $V(z)$ integral, which establishes the Fourier transform relation between $R(\theta)$ and $V(z)$. Examples are given to show that with this measurement technique, the acoustic phase velocities of the propagating modes in the solid medium can easily be determined and material losses can be estimated. The same technique is also used for characterizing imaging performance of focused systems. Applications in thin-film measurement are also discussed.

I. INTRODUCTION

A NEW TECHNIQUE for measuring and interpreting the acoustic material signature or the so-called $V(z)$ in acoustic microscopy will be presented in this paper. $V(z)$ refers to the variation of the normalized voltage output of an acoustic microscope as a function of the separation distance z between the focal point of the acoustic lens and the plane surface of a reflecting object [1]–[4]. This variation of voltage response with distance is characteristic of the material being examined and is an important source of contrast in acoustic micrographs. The $V(z)$ effect is a well-understood phenomenon, and various models have been put forth to explain how it is related to acoustic material properties [1], [2], [5], [6], [9]. So far, practical application revolves around the inverse process of determining acoustic-property-dependent parameters by interpreting selective features of the magnitude of the $V(z)$ function. For example, the leaky surface acoustic wave velocity can be obtained directly from the periodicity of the interference peaks and nulls of the magnitude of the $V(z)$ function in the negative z region [4]–[7], where the object surface is located between the focal point and the lens. Another approach involves the Fourier transform of the negative z portion of the magnitude of the $V(z)$ function in order to identify propagating modes at the liquid-solid interface and to determine their respective phase velocities [8].

The basic theory and experimental result of a more general Fourier transform technique, which utilizes both the magnitude and phase of the $V(z)$ function for material property characterization, will be given in this paper. The theoretical treatment is a combination of angular spectra and ray optics formalisms. It is carried out specifically for

the case where the acoustic transducer is a spherical shell that radiates directly into the liquid coupling medium and hence forms a focusing lens by itself. An integral expression relating the complex $V(z)$ and the reflectance $R(\theta)$ of the liquid-solid specimen interface as a function of the angle θ between the direction of an incident plane wave and the normal to the interface surface is derived. It will be shown that by a suitable transformation of variables, $R(\theta)$ can be obtained by an inverse Fourier transform of $V(z)$.

The primary motivation behind this work is that the complex reflectance function $R(\theta)$ contains a wealth of readily available acoustic material property information. The solid curves in Fig. 7 show the theoretical magnitude and phase of the reflectance function of a water-fused-silica interface. The longitudinal and shear critical angles, θ_{Lc} and θ_{Sc} , show up as distinctive features on the magnitude curve and their locations give the propagation velocities of the respective modes directly. In addition the Rayleigh critical angle θ_{Rc} corresponds to the point where the phase curve becomes π in a region where it undergoes a rapid 2π radian change. Also, as will be shown in Section IV, the effect of loss in the solid medium can readily be observed in and estimated from the reflectance function $R(\theta)$. There are other potential areas of application involving film thickness measurement and the thin-film acoustic matching between two media of vastly different impedances, which will also be explored in Section IV.

II. NONPARAXIAL FORMULATION OF THE $V(z)$ INTEGRAL

The derivation of the relation between $V(z)$ and $R(\theta)$ in the literature [1], [2], [6], [9] can be classified into two general categories: those involving Fourier spectral decomposition [1], [2], [6] and those based on ray optic models [9]. The angular spectrum approach is more amenable to inversion since $V(z)$ can be expressed as an integral involving $R(\theta)$, and the integral can easily be manipulated to establish a Fourier transform relation between $V(z)$ and $R(\theta)$. The ray optic approach essentially regards $V(z)$ as the interference between a family of specularly reflected rays and a family of laterally displaced leaky surface acoustic wave rays. It is not complete in that it neglects the contributions from regions near the longitudinal and shear critical angles. Also, since it does not take diffraction into account, it is not valid near the focal plane. In addition, the ray optic formalism in the form usually given is incompatible with inversion procedures for finding $R(\theta)$. A common drawback to both kinds of formula-

Manuscript received November 1984; revised November 1984.

This work was supported by the Air Force Office of Scientific Research under Contract AFOSR-84-0063.

The authors are with Edward L. Ginzton Laboratory, W. W. Hansen Laboratories of Physics, Stanford University, Stanford, CA 94305, USA.

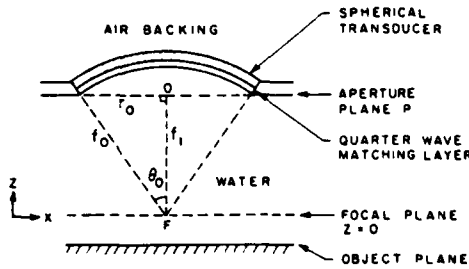


Fig. 1. Schematic of spherical focused transducer used in $V(z)$ measurements.

tions is that they both make use of the paraxial approximation.

An alternative hybrid formulation of the relation between $V(z)$ and $R(\theta)$ will be given in the following treatment. This approach combines features from the angular spectrum as well as the ray optic models and is valid for all z including the focal plane. Moreover, no paraxial assumption has to be made in its development. The special case of a focused spherical transducer radiating directly into water with no buffer medium, as shown in Fig. 1, is considered. The practical significance of this acoustic lens configuration will be discussed in Section IV. The elimination of the buffer rod simplifies the derivation. However, the final solution is valid for any lens configuration that generates a converging spherical wave, and can be generalized for use with other systems.

Using the notation given in Fig. 1, the potential or pressure field emitted by a transducer of diameter $2r_0$ is equivalent to that produced by a perfect converging spherical wave impinging on a circular aperture of radius r_0 . All acoustic field terms will be assumed to vary as $\exp(j\omega t)$. Referring to the aperture plane P in Fig. 1, the potential field distribution in cylindrical coordinates is given by the relation

$$\phi(r) = P(r) \frac{\exp[jk\sqrt{r^2 + f_1^2}]}{\sqrt{r^2 + f_1^2}} \quad (1)$$

where $f_1 = \sqrt{f_0^2 - r_0^2}$ or $f_1 = f_0 \cos \theta$; f_0 is the focal length; θ_0 is the maximum half angle subtended by the aperture at the focus; and k is the propagation constant in the liquid medium. $P(r)$ is the pupil function of the lens, which in the most general case takes into account the non-uniform excitation of the transducer and any aberration effects. In the simplest case for an ideal lens

$$P(r) = \begin{cases} 1 & 0 < r < r_0 \\ 0 & r > r_0 \end{cases} \quad (2)$$

Making use of the circular symmetry of the field distribution, $\phi(r)$ can be decomposed into cylindrical radial waves of wave number k , by applying the Hankel transform

$$A(k_r) = \int_0^\infty P(r) \frac{\exp[jk\sqrt{r^2 + f_1^2}]}{\sqrt{r^2 + f_1^2}} J_0(k_r r) r dr. \quad (3)$$

Here $k^2 = k_z^2 + k_r^2$. Since the transducer diameter is normally many wavelengths wide and the integrand is weighted by r , the contribution to the integral by $J_0(k_r r)$ comes mainly from regions where $k_r r$ is large. Therefore $A(k_r)$ can be approximated by replacing $J_0(k_r r)$ with its large argument asymptotic form

$$J_0(k_r r) \sim \frac{\exp\left[-j\left(k_r r - \frac{\pi}{4}\right)\right] + \exp\left[j\left(k_r r - \frac{\pi}{4}\right)\right]}{\sqrt{2\pi k_r r}} \quad (4)$$

Thus, it follows that

$$A(k_r) \sim \int_0^\infty P(r) \frac{\exp[j\psi_1(r)] + \exp[j\psi_2(r)]}{\sqrt{2\pi k_r r(r^2 + f_1^2)}} r dr \quad (5)$$

where

$$\begin{aligned} \psi_1(r) &= \left(k\sqrt{r^2 + f_1^2} - k_r r + \frac{\pi}{4}\right) \\ \psi_2(r) &= \left(k\sqrt{r^2 + f_1^2} + k_r r - \frac{\pi}{4}\right). \end{aligned}$$

The method of stationary phase will now be applied to evaluate (5) [10]. Consider the phase of the first term of the integrand $\psi_1(r)$. The contribution to the integral comes from the region near where $\psi_1'(r) = 0$

$$\psi_1'(r) = \frac{kr}{\sqrt{r^2 + f_1^2}} - k_r = 0$$

or where $r = r'$

$$r' = \frac{k_r}{\sqrt{k^2 - k_r^2}} f_1 = \frac{k_r}{k_z} f_1. \quad (6)$$

Note that r' is positive in this case.

Next, consider the phase of the second term of the integrand $\psi_2(r)$. Setting $\psi_2'(r)$ to zero yields the result

$$\frac{kr'}{\sqrt{r'^2 + f_1^2}} = -k_r \quad (7)$$

which implies that r' is negative. Since in a cylindrical coordinate system r is always positive, there is no contribution to $A(k_r)$ from the second term of the asymptotic form of $J_0(k_r r)$.

Equation (5) therefore becomes

$$A(k_r) = \left(\frac{2\pi}{|\psi_1''(r')|}\right)^{1/2} P(r') \frac{\exp[jk\psi_1(r')]}{\sqrt{2\pi k_r r'(r'^2 + f_1^2)}} \frac{k_r}{k_z} f_1 \quad (8)$$

where r' is given by (6) and

$$\psi_1''(r') = \frac{k}{\sqrt{r'^2 + f_1^2}} - \frac{kr'^2}{(r'^2 + f_1^2)^{3/2}} = \frac{k_z^3}{k^2 f_1}$$

Substituting (6) into (8) gives the result

$$A(k_r) = P(k_r) k \exp[jk_z f_1]/k_z \quad (9)$$

where

$$k_z = \sqrt{k^2 - k_r^2}. \quad (10)$$

To find the corresponding angular spectrum at a plane of distance $z + f_1$ from the aperture plane P , each spectral component is multiplied by the propagation factor $\exp[-jk_z(z + f_1)]$. For instance, at the focal plane $z = 0$

$$A(k_r; 0) = P(k_r) k/k_z \quad (11)$$

which simply means that with an ideal pupil function all angular spectral components arrive in phase at the focal point. In general, for any arbitrary z

$$A(k_r; z) = P(k_r) k \exp[-jk_z z]/k_z. \quad (12)$$

Suppose the plane reflector specimen is placed at z , and the reflectance function of the liquid-specimen interface is $R(k_r)$. The reflected angular spectrum at z is

$$B(k_r; z) = R(k_r) A(k_r; z). \quad (13)$$

The reciprocity principle of Kino and Auld given in the Appendix is employed to find the normalized voltage response $V(z)$ of the focused transducer to the reflected wave in which the spectrum is given by (13). $V(z)$ is equal to the scattering coefficient s_{11}

$$V(z) = s_{11} = \frac{j}{2} \frac{\int (\phi^i u_z^i - \phi^i u_z^{i*}) dS}{\int \phi^i u_z^{i*} dS} \quad (14)$$

where u_z is the normal displacement at the liquid-solid interface, and the integration is evaluated over the same. The superscripts i and r designate the incident and the reflected fields respectively, and

$$\begin{aligned} u_z^i &= \frac{\partial \phi^i}{\partial z} \\ u_z^r &= \frac{\partial \phi^r}{\partial z}. \end{aligned} \quad (15)$$

For the circularly symmetric incident and reflected radial wave components, the Hankel transforms of the u_z components are

$$\begin{aligned} U_z^i(k_r) &= -jk_z A(k_r) \\ U_z^r(k_r) &= jk_z B(k_r). \end{aligned} \quad (16)$$

By applying Parseval's Theorem and substituting in (16), (14) can be written in the form

$$V(z) = \frac{\int A(k_r; z) B(k_r; z) k_z k_r dk_r}{\int A(k_r; z) A^*(k_r; z) k_z k_r dk_r}. \quad (17)$$

Substituting (12) and (13) into (17), the final result is

$$V(z) = \frac{\int P^2(k_r) R(k_r) \frac{\exp[-j2k_z z]}{k_z} k_r dk_r}{\int \frac{P^2(k_r)}{k_z} k_r dk_r} \quad (18)$$

By making the following substitution of variables, a comparison can be made between (18) and Atalar's paraxial angular spectrum formulation of the $V(z)$ integral [1]. Let

$$k_r/k = r/f_0. \quad (19)$$

Equation (18) can be written in the form

$$V(z) = \frac{\int P^2(r/f_0) R(r/f_0) \frac{\exp[-j2kz\sqrt{1-(r/f_0)^2}]}{\sqrt{1-(r/f_0)^2}} r dr}{\int P^2(r/f_0) \frac{r dr}{\sqrt{1-(r/f_0)^2}}} \quad (20)$$

which differs from Atalar's solution by the factor $1/\sqrt{1-(r/f_0)^2}$ in the denominator of each integrand. In the limit of the paraxial approximation where $(r/f_0)^2$ is assumed to be small, this additional factor tends to unity, and (18) becomes the expression derived by Atalar.

III. FOURIER TRANSFORM RELATION BETWEEN $V(z)$ AND $R(\theta)$

The possibility of obtaining $R(\theta)$ by inverting $V(z)$ has been alluded to in optical microscopy [11], and the inversion has been demonstrated in acoustic microscopy [12] based on Atalar's paraxial $V(z)$ integral. The Fourier transform relation between $V(z)$ and $R(\theta)$ for the nonparaxial formulation given in (18) can be established as follows. Since $k_z^2 = k^2 - k_r^2$, it follows that

$$k_z dk_z = -k_r dk_r \quad (21)$$

Equation (18) becomes

$$V(z) = C \int_k^{k \cos \theta_0} P^2(k_z) R(k_z) \exp(-j2k_z z) dk_z \quad (22)$$

where C is the normalization factor given by

$$C = \left[\int_k^{k \cos \theta_0} P^2(k_z) dk_z \right]^{-1} \quad (23)$$

Noting that $k_z = k \cos \theta$, where $k = 2\pi/\lambda$, and making the following change of variables

$$\begin{aligned} u &= \frac{z}{\lambda} \\ t &= 2 \cos \theta \end{aligned} \quad (24)$$

we obtain the result

$$V(u) = C \int_2^{2 \cos \theta_0} P^2(t) R(t) \exp(-j2\pi ut) dt. \quad (25)$$

In short-hand notation

$$V(u) = \mathcal{F}\{P^2(t) R(t)\} \quad (26)$$

where $\mathcal{F}\{\}$ denotes the Fourier transform. The inversion to obtain $R(t)$ is given by

$$R(t) = \begin{cases} \frac{\mathcal{F}^{-1}\{V(u)\}}{P^2(t)}, & 2 > t > 2 \cos \theta_0 \\ 0, & \text{otherwise.} \end{cases} \quad (27)$$

Note that $R(t)$ is only determined for the angular range of insonification covered by the pupil function of the lens. In general $P(t)$ is not known *a priori*. However, $P^2(t)$ can conveniently be calibrated by inverting the $V(z)$ function for a liquid-solid interface in which the reflectance has uniform magnitude and phase over the angular extent of the lens pupil function. In particular, if a perfectly reflecting surface with $R(t) \equiv 1$ is used

$$P^2(t) = \mathcal{F}^{-1}\{V_0(u)\} \quad (28)$$

where $V_0(u)$ is the $V(z)$ of the "ideal" reflector.

This inversion approach to material characterization is different in that it requires the measurement of $V(z)$ in both amplitude and phase whereas previous work [1]–[8] utilized only the amplitude or intensity of $V(z)$. It is generally not trivial to conduct high-accuracy phase measurement in acoustic microscopy. A special phase-measurement system [13] has been developed to enable the precise acquisition of phase data and the subsequent experimental demonstration of the inversion technique.

It is interesting at this point to examine the range resolution of a confocal imaging system such as the reflection acoustic microscope for an ideal plane reflector; i.e., $R(\theta) \equiv 1$. Assuming an ideal lens pupil function of the form in (2), the voltage response of the acoustic microscope as a function of defocusing distance can be calculated from (25) to be

$$V(u) = C \int_2^{2 \cos \theta_0} \exp[-j2\pi ut] dt$$

or

$$V(u) = -C \exp[-j\pi u(1 + \cos \theta_0)] \cdot \text{sinc}[2u(1 - \cos \theta_0)]. \quad (29)$$

The 3-dB point of $|V(u)|$ is given by the relation

$$2(1 - \cos \theta_0) u_{3dB} = 0.45\pi$$

or

$$z_{3dB} = \frac{0.225\lambda}{1 - \cos \theta_0}$$

Therefore the 3-dB range resolution or the focal depth for a plane reflector is

$$\Delta z_{3dB} = \frac{0.45\lambda}{1 - \cos \theta_0}. \quad (30)$$

IV. EXPERIMENTAL RESULTS

In the $V(z)$ measurement a special acoustic transducer is used. The piezoelectric element is a spherical shell with an air backing and a quarter-wave matching layer on the front face. The transducer radiates directly into water, and thus forms an aberration-free spherical lens that focuses the emitted acoustic beam into a diffraction-limited spot at the center of curvature of the transducer. This acoustic lens configuration is advantageous for $V(z)$ measurements because the elimination of the buffer rod removes the systematic noise due to reverberations inside the buffer rod that tend to overlap in time with the reflected signal from the object. With such a construction the acoustic lens can be translated over a wide range of z to collect $V(z)$ data in an essentially noise-free environment. The maximum limit to the vertical movement is imposed by how far the lens can be moved towards the specimen. The problem with multiple echoes in the water path between the transducer and the specimen is overcome by exciting the transducer with a short tone burst and time-gating the first arrival return signal.

Two transducers of this type with $F/1$ and $F/0.7$ apertures, respectively, are used in the experiment. The radius of curvature or focal length f_0 is 16 mm in both cases. From geometric considerations, the maximum possible negative defocusing distance is given by

$$z_{\min} = -f_1 = -f_0 \sqrt{1 - 1/(2F)^2} \quad (31)$$

where F is the f -number of the lens. For the $F/0.7$ lens $|z_{\min}| = 11.2$ mm, and for the $F/1$ lens $|z_{\min}| = 13.9$ mm. The importance of z_{\min} will be discussed in Section V.

Both transducers have a fundamental frequency of approximately 3 MHz. For $V(z)$ measurements, they are operated at the third harmonic frequency of 10.17 MHz for the $F/0.7$ lens and 10.7 MHz for the $F/1$ lens. Many practical considerations go into this particular choice of operating frequency range. The inversion formalism is most conveniently applied to a lossless liquid medium. The loss in water is essentially negligible at 10 MHz and so satisfies this requirement. Moreover, the wavelength in water of about 150 μm is sufficiently large to render any irregularity and instability in the vertical translation mechanism insignificant. By the same token the measurement is less subject to error as a result of surface finish imperfections in the sample.

A lead sample is used to calibrate the pupil function of the lens. With a longitudinal velocity $v_L = 2200$ m/s, the longitudinal critical angle for the water-lead interface occurs at $\theta = 43^\circ$, as illustrated in the theoretical plot in Fig. 2. The reflectance function is essentially flat in both amplitude and phase from $\theta = 0^\circ$ to 40° . Fig. 3 shows the magnitude and phase of the $V(z)$ for lead from $z = -8$ mm to $z = +8$ mm. The phase displayed is in fact that of $V(z)$ with the linear phase term $2kz$ subtracted out. Fig. 4 shows $P^2(\theta)$ for the $F/0.7$ lens obtained by inverting the experimental $V(z)$ for lead. The pupil function is not uniform in either magnitude or phase especially near the edge

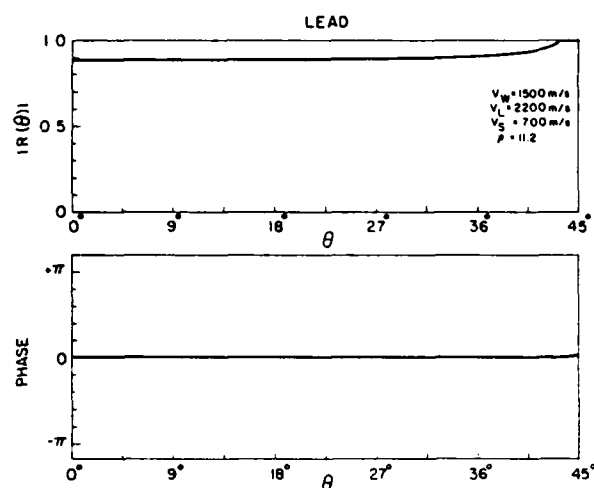


Fig. 2. Magnitude and phase of the theoretical reflectance function of a water-lead interface.

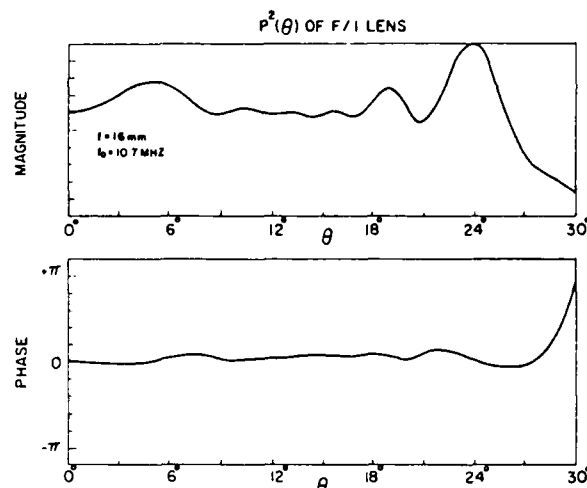


Fig. 5. Calibration of the pupil function of the 10.7 MHz $F/1$ focused transducer.

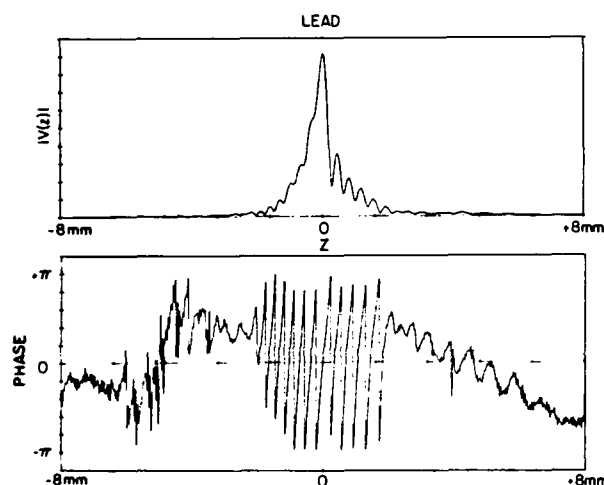


Fig. 3. Experimental $V(z)$ of a water/lead interface measured with a 10.17 MHz $F/0.7$ focused transducer.

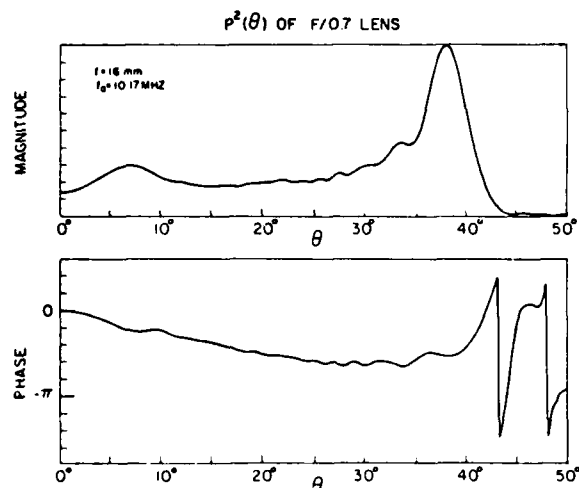


Fig. 4. Calibration of the pupil function of the 10.17 MHz $F/0.7$ focused transducer.

of the lens where an accentuated peak occurs around $\theta = 38^\circ$. Premature roll-off of the lens angular response is also evident, and the illumination from the outer periphery of the lens is weak. The experimental $P^2(\theta)$ for the $F/1$ lens

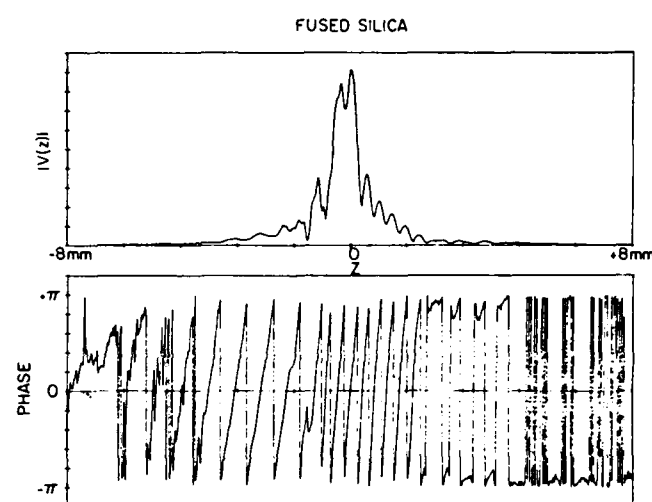


Fig. 6. Experimental $V(z)$ of water-fused-silica interface at 10.17 MHz.

shown in Fig. 5 exhibits a similar, though less pronounced, peak at $\theta = 23.5^\circ$. These anomalies in the lens response are due to nonuniformity in the thickness of the matching layer as a result of difficulties encountered in the fabrication process [23].

It should be pointed out that this simple calibration procedure can be utilized as an alternative method for characterizing and predicting imaging performance of focused systems. Instead of measuring the point spread function at the focal plane as is the case in most conventional techniques, the characterization is done in terms of the pupil function illumination. This approach has direct relevance and application in the fabrication of spherical acoustic lenses, where the sphericity of the lens and the uniformity of the matching layer are of primary concern.

Fused Silica

The experimental $V(z)$ for fused silica is shown in Fig. 6. Fig. 7 displays the corresponding $R(\theta)$, which is obtained by inverting the $V(z)$ and then dividing out the calibrated value of $P^2(\theta)$ for the $F/0.7$ lens. The theoretical

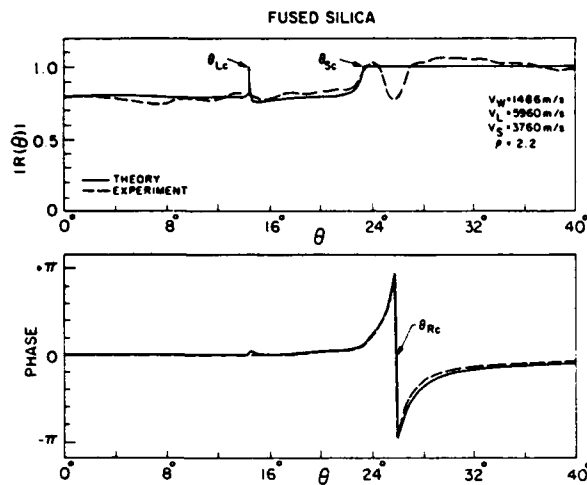


Fig. 7. Comparison of the theoretical and experimental reflectance function for a water-fused-silica interface.

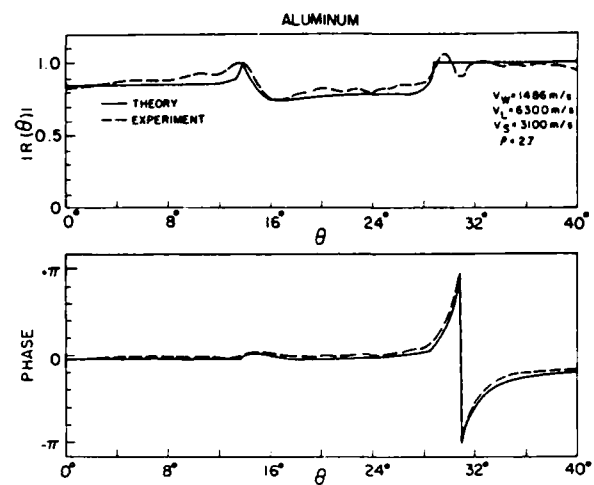


Fig. 9. Comparison of the theoretical and experimental reflectance function for a water-aluminum interface.

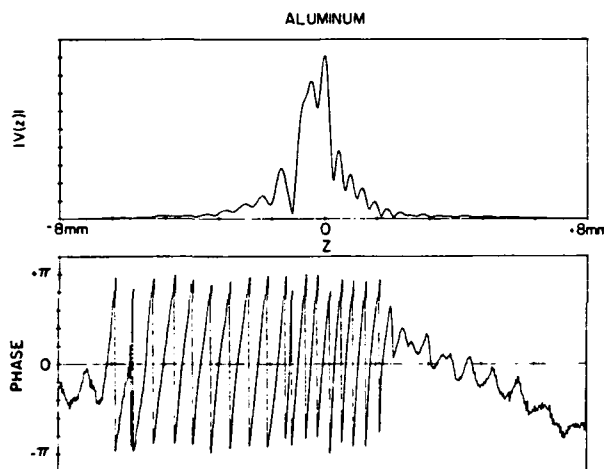


Fig. 8. Experimental $V(z)$ of a water-aluminum interface at 10.17 MHz.

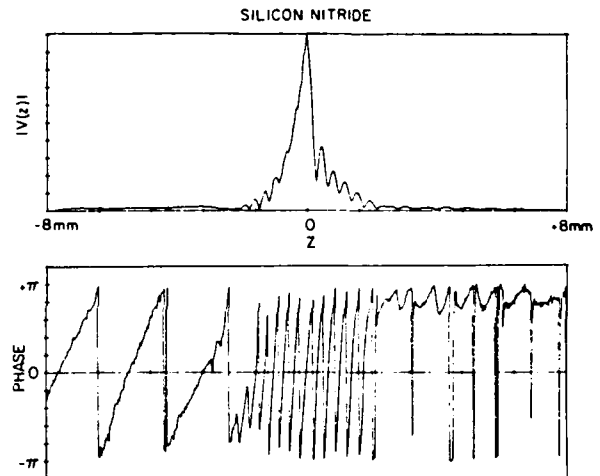


Fig. 10. Experimental $V(z)$ of a water-silicon-nitride interface at 10.17 MHz.

reflectance is also shown for comparison. A value of $v_W = 1486$ m/s is used as the velocity in water in the inversion algorithm. There is good general agreement between theory and experiment in both magnitude and phase. The experimental shear critical angle at $\theta = 23.5^\circ$ and the Rayleigh critical angle at $\theta = 25.85^\circ$ compare extremely well with the theoretical values. The longitudinal critical angle is not reproduced in the experimental result due to the problem of degradation angular resolution caused by the spatial truncation of the $V(z)$ data. This difficulty will be elaborated upon in Section V.

Aluminum

Figs. 8 and 9 are the $V(z)$ and $R(\theta)$ for aluminum. Again the agreement between theory and experiment is very good. The longitudinal and shear critical angles show up clearly in the experimental result, in this case at $\theta = 13.64^\circ$ and $\theta = 28.64^\circ$, respectively. The Rayleigh critical angle is located at $\theta = 30.86^\circ$, which gives a phase velocity of 2897 m/s for the leaky surface acoustic wave.

Silicon Nitride

Figs. 10 and 11 show the $V(z)$ and $R(\theta)$ for hot-pressed silicon nitride, which is a ceramic material with high acoustic velocity. All the critical angles occur at low-incidence angles, and only the Rayleigh critical angle at $\theta = 15.0^\circ$ is reproduced in the experimental phase curve. It should be noted that the dip in the experimental magnitude curve for silicon nitride and smaller dips at the Rayleigh critical angle in Figs. 7 and 9 for fused quartz and aluminum are only an artifact introduced by the spatial truncation of the experimental $V(z)$ data. Similar dips can occur as a result of shear loss in the solid, an effect widely known as the Rayleigh critical-angle phenomenon [14], [15]. However, the acoustic losses in all three materials are known to be negligible at 10 MHz, therefore the experimental dips cannot possibly be associated with loss. As will be shown in the following section on error analysis, this experimental artifact is well understood and in some cases can be alleviated. Hence, the inversion tech-

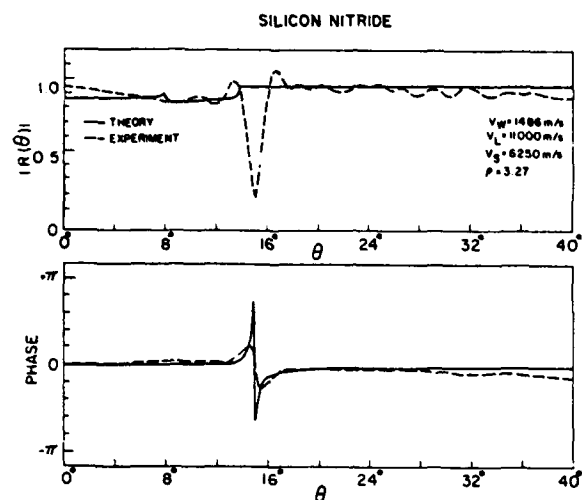


Fig. 11. Comparison of the theoretical and experimental reflectance function for the water-silicon-nitride interface.

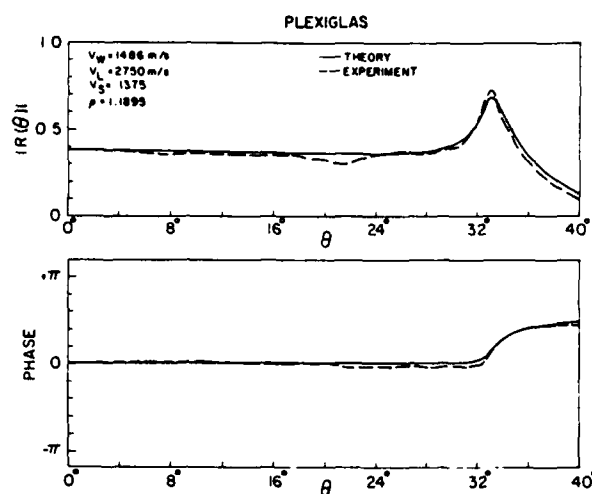


Fig. 13. Comparison of the theoretical and experimental reflectance function for a water-Plexiglas interface.

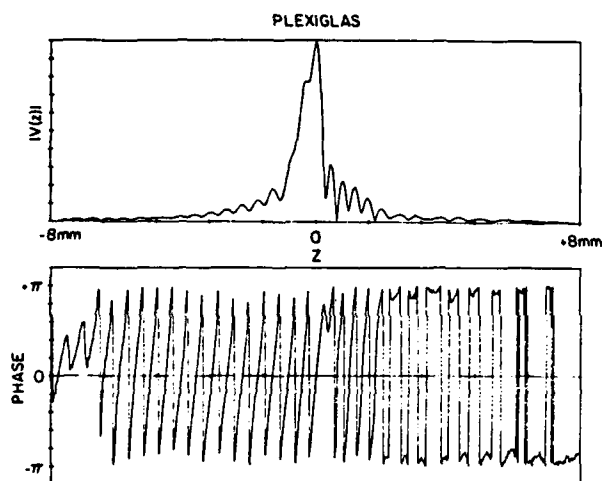


Fig. 12. Experimental $V(z)$ of a water-Plexiglas interface at 10.17 MHz.

nique does not preclude the characterization of such acoustic properties as shear loss, temperature dependence of the Rayleigh-wave velocity, and various contributing factors to the Rayleigh critical-angle phenomenon.

Plexiglas

Figs. 12 and 13 are the $V(z)$ and $R(\theta)$, respectively, for plexiglas or lucite, a low-acoustic velocity and high loss material. This example illustrates how material loss can be determined. The longitudinal critical angle is located at $\theta = 32.7^\circ$, which corresponds to a longitudinal wave velocity of 2750 m/s. The magnitude of the reflectance peaks at 0.7 rather than one, as it would be for a lossless substrate. The amount of diminution of the peak level depends on the loss for the longitudinal mode. The theoretical curve is fitted to the experimental one by varying the longitudinal loss factor Q_L . The Q_L is found to be about 50, which translates into an attenuation coefficient of 232 Np/m or 20 dB/cm at 10 MHz, which agrees well with other published values [16].

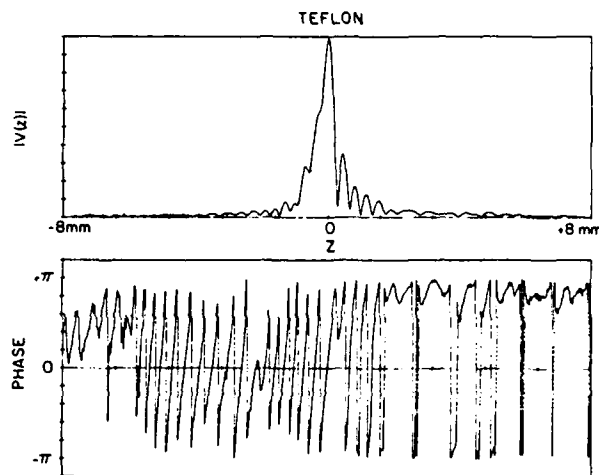


Fig. 14. Experimental $V(z)$ of a water-teflon interface at 10.17 MHz.

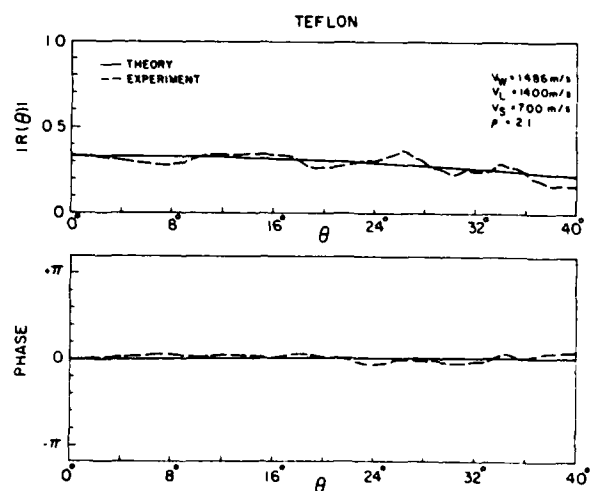


Fig. 15. Comparison of the theoretical and experimental reflectance function for a water-teflon interface.

Teflon

$V(z)$ and $R(\theta)$ for teflon are displayed in Figs. 14 and 15. As expected no critical angle is observed, since teflon

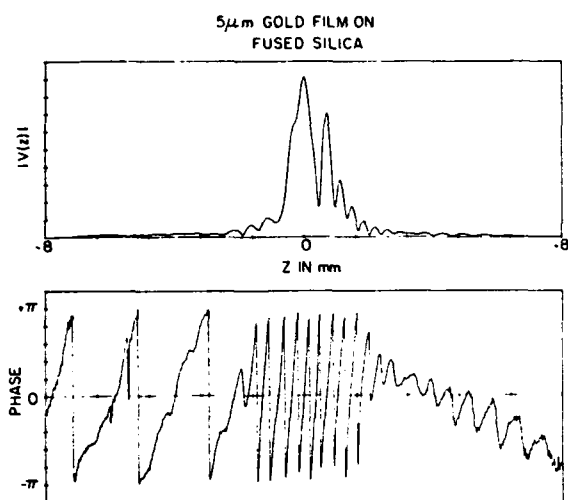


Fig. 16. Experimental $V(z)$ of a water and 5- μ m gold film on a fused-silica interface at 10.7 MHz.

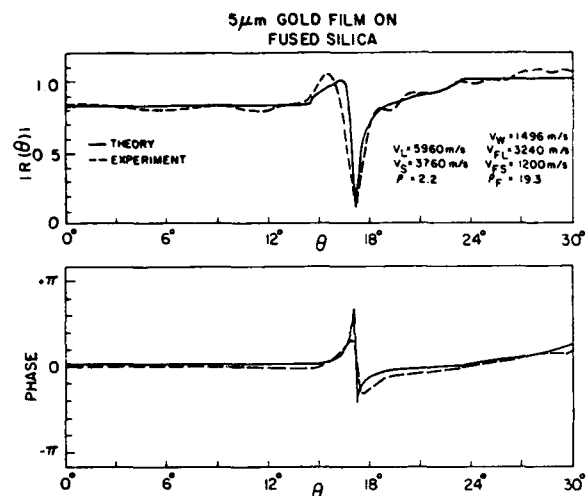


Fig. 17. Comparison of the theoretical and experimental reflectance function for a water and 5- μ m gold film on a fused-silica interface.

has a longitudinal velocity of 1400 m/s, which is lower than that of water.

Thin-Film Measurement

The following example demonstrates the potential application of acoustic microscopy in thin-film characterization and also confirms a thin-film matching phenomenon predicted by numerical computation. The thin-film structure used in this example is a 5- μ m-thick gold film deposited on a fused-silica substrate. At 10 MHz the thickness of the gold film corresponds to about 1.5 percent of the longitudinal wavelength. Figs. 16 and 17 are the plots of $V(z)$ and $R(\theta)$, respectively. The agreement with the theoretically generated $R(\theta)$ is good. $R(\theta)$ shows a null at $\theta = 17.23^\circ$, an angle between the longitudinal and shear critical angles of the fused silica substrate. Physically this means that the incident longitudinal mode in water couples very strongly into a bulk propagating mode in the fused silica substrate. The physics of this coupling is not well understood, but it is believed that the longitudinal

wave in water converts in the gold film to a leaky Sezawa wave, which leaks into the fused silica substrate in the form of a propagating shear wave. The coupling efficiency and the angle of incidence, at which maximum transmission occurs, have been shown to be functions of the film thickness by numerical analysis. Thus by measuring the reflectance, one can get information about the film thickness. The experimental demonstration of this thin-film phenomenon also opens up the possibility of using the thin-film matching technique in the design of acoustic transducers to improve the transmission efficiency between two media with vastly different acoustic impedances.

V. ERROR ANALYSIS

The introduction of experimental artifacts in the experimental $R(\theta)$ due to the spatial truncation of the $V(z)$ curve is treated in this section. This problem arises because of the finite distance over which $V(z)$ data can be collected. Equation (26) shows that $V(u)$ and $[P^2(t)R(t)]$ form a Fourier-transform pair. It can be shown by Fourier-transform theory that since $[P^2(t)R(t)]$ is finite in the t domain, $V(u)$ has to be infinite in the u domain. Experimentally $V(z)$ can only be obtained for some finite-width data window. Therefore the actual waveform $V'(z)$ used in the inversion is a truncated version of $V(u)$. Thus

$$V'(u) = V(u) \text{rect}(u/D) \quad (32)$$

where $u = z/\lambda$, and D is the width of the data window defined in terms of the number of wavelengths in water. Noting that multiplication in the u domain corresponds to convolution in the transform domain t , the reflectance function obtained by inverting $V'(u)$ is

$$[P^2(t)R(t)]' = [P^2(t)R(t)] * D \text{sinc}(Dt) \quad (33)$$

where $*$ denotes convolution.

The effects of the convolution between the reflectance function and the waveform $\text{sinc}(Dt)$ are twofold. First, the angular resolution in the t domain is degraded. Second, because of the oscillatory nature of $\text{sinc}(Dt)$, sharp features in $P^2(t)R(t)$ tend to generate ripples in the resulting $[P^2(t)R(t)]'$. The resolution degradation effect can be estimated as follows. The full width between zeroes of the main lobe of $\text{sinc}(Dt)$ is

$$\Delta t = 2/D. \quad (34)$$

The Δt is essentially the transition width of the response to a sharp step in $P^2(t)R(t)$ and hence can be regarded as the worst case resolution in t . Using the relation $t = 2 \cos \theta$ given in (24), we get the following expression for the angular resolution in terms of the angle of incidence θ

$$\Delta \theta = \frac{\Delta t}{2 \sin \theta}. \quad (35)$$

Combining (34) and (35), the resolution in θ in terms of the width of the data window D is found to be

$$\Delta \theta = \frac{1}{D \sin \theta}. \quad (36)$$

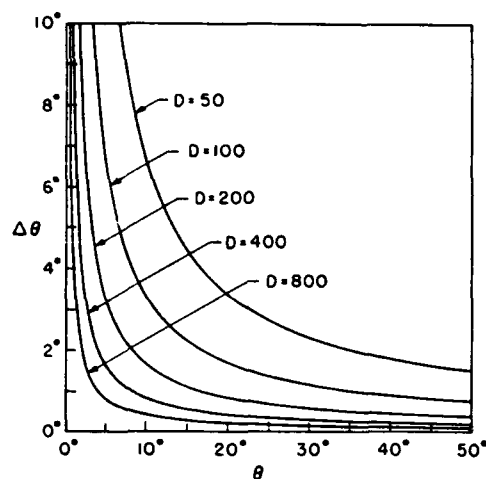


Fig. 18. Variation of angular resolution degradation as a function of the incident angle and the normalized data window width D .

Equation (36) is plotted in Fig. 18 with D as a parameter. The data window D used in the experiment is about 100. This implies angular resolution of about 3.3° at $\theta = 10^\circ$, 1.7° at $\theta = 20^\circ$, and 1.1° at $\theta = 30^\circ$. The experimental reflectance of silicon nitride in Fig. 11 is a pathological example of the degradation effect of this angular resolution. The Rayleigh critical angle occurs at a low value of $\theta = 15.0^\circ$ and in the vicinity of this angle, the magnitude of the reflectance is unity but the phase goes through a rapid 2π radian change over a 2° angular range. The net result of the convolution with $\text{sinc}(D\theta)$ is a sharp dip in the magnitude of the experimental reflectance and a smoothing of the phase curve near the Rayleigh critical angle. The effect of the convolution is much less serious at angles of high incidence as shown in Fig. 18 and as evidenced by the experimental $R(\theta)$'s of fused silica and aluminum, where only a slight dip occurs in the reflectance magnitude.

A computer simulation has been carried out where the theoretical $R(\theta)$ for silicon nitride is used to generate the $V(z)$, which is truncated and then inverted in an identical manner to the experimental data. The result is shown in Fig. 19. The simulated $R(\theta)$ exhibits exactly the same behavior in both amplitude and phase as the experimental one in Fig. 11.

The locations of the critical angles are generally used to determine the phase velocities of propagating modes, which are given by

$$v_* = v_w / \sin \theta_*$$

where v_w is the velocity in water; the asterisk stands for L (longitudinal), S (shear), or R (Rayleigh); and the subscript c denotes critical angle. The percentage error in the estimation of v_* as a consequence of the truncation of $V(z)$ can be shown to be

$$\left| \frac{\Delta v_*}{v_*} \right| = \frac{1}{2} \frac{\cos \theta_*}{\sin \theta_*} \Delta \theta_* = \frac{1}{2} \frac{\cos \theta}{D \sin^2 \theta}. \quad (37)$$

Equation (37) is plotted in Fig. 20 with D as a parameter.

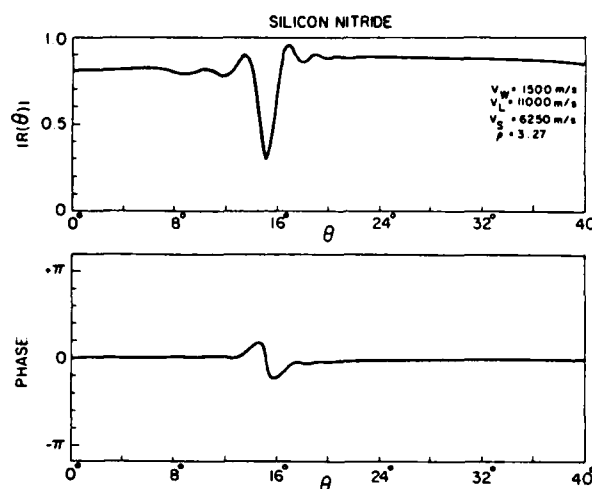


Fig. 19. Simulated reflectance function of a water-silicon nitride interface obtained by inverting spatially truncation $V(z)$ data.

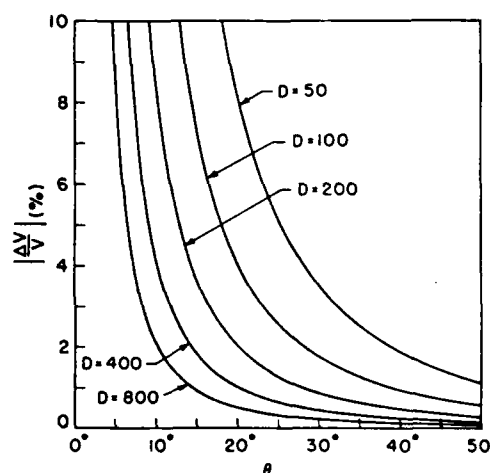


Fig. 20. Phase velocity estimation error as a function of angle of incidence due to degradation of the angular resolution.

The error decreases drastically with increasing incidence and increasing D . For $D = 100$, $|\Delta v/v|$ is four percent at $\theta = 20^\circ$ and 1.75 percent at $\theta = 30^\circ$. One should bear in mind that (37) represents the worst-case estimation, and the actual error could well be substantially smaller, especially for the Rayleigh critical angle θ_{Rc} . The determination of θ_{Rc} involves locating the point, where the phase of $R(\theta)$ is π radians. Around θ_{Rc} the magnitude of the reflectance function for a lossless material is constant while the phase Ψ can be shown to have the form [9]

$$\tan \Psi = 2 \frac{k_r - k \sin \theta_{Rc}}{\alpha} \quad (38)$$

where α is the leak rate of the Rayleigh wave. The phase function Ψ is the antisymmetric in k_r about $\Psi = \pi$ around the point $k_r = k \sin \theta_{Rc}$. It is similarly antisymmetric in k_z or t in the neighborhood of $k_z = k \cos \theta_{Rc}$. Since the sinc function with which $[P^2(t)R(t)]$ is convolved is symmetric, the phase function Ψ around the Rayleigh critical angle remains essentially unchanged by the convolution,

provided that the width of the main lobe of the sinc function Δr is smaller than the transition width of Ψ through the Rayleigh critical-angle region. For example, in the case of fused silica and aluminum, the respective leaky surface-acoustic-wave velocities calculated from the experimental phase curve are almost identical to those predicted by theory.

The second problem associated with the generation of ripples can be partly remedied, though with some further loss in angular resolution, by applying a smooth apodization function for the $V(z)$ data before inversion takes place. The apodization function used in processing the $V(z)$ data is

$$a(u) = \frac{\sin^2(\pi u/D)}{n + \sin^2(\pi u/D)} \quad (38)$$

where n is a free parameter for adjusting the tapering characteristics of the apodization. The $n = 0.1$ is used to process the experimental data shown here. The resulting apodization essentially leaves the data in the center of the window unchanged, but it behaves much like Hamming weighting at the edges of the data window.

The obvious solution to both the resolution degradation and ripple problems is to increase the data window width D of $V'(u)$. Equation (31) shows that this can be realized by increasing the radius of curvature f_0 or reducing the aperture size or both. Also D can be increased by increasing the frequency of operation. For silicon nitride, $R(\theta)$ can be reproduced much more faithfully if $\Delta\theta$ is reduced to $\frac{1}{4}^\circ$, which can be achieved by using an $F/1.5$ lens with a focal length of 32 mm operating at 20 MHz.

Another important source of error is in the estimation of the velocity of water. Since

$$u = z/\lambda = zf/v$$

then

$$du = -\frac{zf}{v^2} dv = -u dv/v. \quad (39)$$

Suppose the wrong velocity is used in the inversion. In (25) this is equivalent to changing u to

$$u' = u + \Delta u = u(1 - \Delta v/v). \quad (40)$$

The resulting inversion is given by

$$[P^2(t)R(t)]' = \int V(u) \exp[j2\pi u(1 - \Delta v/v)t] du$$

or

$$[P^2(t)R(t)]' = P^2R[(1 - \Delta v/v)t]. \quad (41)$$

Therefore using an erroneous v results in a stretched reflectance function in t . Since the velocity of water has a large temperature coefficient, 4 m/s per $^\circ\text{C}$, this error can be significant. It may cause enough misalignment of the inversions of the sample material of interest and the calibration lead sample to have a serious effect on the determination of $R(\theta)$. From (35) and (41) it can easily be shown

that the shift distortion as a function of incidence angle is of the form

$$|\Delta\theta| = \cot\theta \Delta v/v \quad (42)$$

which shows that the most serious errors occur at low angles of incidence.

The problem of determining the true transform $P^2(\theta)R(\theta)$ from a finite segment $V'(z)$ of $V(z)$ is a common one in Fourier analysis and spectral estimation. Various techniques exist in the literature for extrapolating $V'(z)$ so that a more accurate determination of $P^2(\theta)R(\theta)$ can be made. Since $P^2(\theta)R(\theta)$ is a bandlimited function, the maximum spatial frequency being limited by the angular extent of the pupil function, $V(z)$ is analytic in the entire z axis [17]. In principle, an iterative algorithm proposed by Papoulis [18] can be used to improve the accuracy of the estimation of $P^2(\theta)R(\theta)$.

CONCLUSION

We have demonstrated that the reflectance function of a liquid-solid interface can be determined by inverting the corresponding complex $V(z)$ data from an acoustic microscope. This inversion technique represents a more complete approach to material characterization than previous $V(z)$ -related work. The phase velocities of the various propagating modes in the solid medium can be obtained directly from the reflectance function. The effect of material loss can also be observed and quantified. Moreover, this measurement technique provides a means of gauging imaging performance of focused systems by directly measuring the pupil function illumination. In addition, there are useful practical applications in the area of thin-film characterization, and many interesting possibilities exist for more complex structures, such as multi-layered films. The nonparaxial formulation of the $V(z)$ integral is important in that it lays a sound theoretical foundation for the inversion measurement technique. The excellent agreement between the theoretically and experimentally obtained reflectance functions further supports the validity of the nonparaxial theory.

Although this work has been carried out and discussed in the context of acoustic microscopy, the validity and applicability of many of the underlying concepts extend to optical microscopy as well. Provided one can accurately measure the optical phase, which is not trivial but certainly realizable [22], the inversion algorithm described here can be used to obtain the optical reflectance function from the corresponding complex optical $V(z)$ function.

ACKNOWLEDGMENT

The authors would like to thank Dr. Simon Bennett and Dr. Ian Smith for the stimulating discussions related to this work.

APPENDIX

Auld and Kino [19]–[21], by using the reciprocity theorem, were able to determine the normalized reflected signal or reflection coefficient s_{11} from an object. The theory

for longitudinal waves in a liquid can be stated in the form

$$s_{11} = \frac{j\omega \int (u^i p - u p^i) n dS}{4P} \quad (A1)$$

where the integral is taken over the surface of the object, u is the displacement, and p is the pressure fields associated with an incident wave of temporal frequency ω . Here $\exp(j\omega t)$ time dependence is assumed. The superscript i denotes the incident or transmitted wave when the object is not present, and the unsuperscripted terms denote the total field at the obstacle. The parameter P is the power exciting the transducer for a given incident signal u^i, p^i .

The total fields can be written in the form

$$u = u^i + u^r \quad (A2)$$

$$p = p^i + p^r \quad (A3)$$

where the superscript r denotes the waves reflected from the object. Substituting (A2) and (A3) into (A1) yields

$$s_{11} = \frac{j\omega \int (u^i p^r - u^r p^i) n dS}{4P} \quad (A4)$$

If the object is a semi-infinite plane normal to the z direction, s_{11} can be written in the normalized form

$$V(z) = \frac{\int (u_z^i p^r - u_z^r p^i) dS}{2 \int u_z^i p^{i*} dS} \quad (A5)$$

where the asterisk denotes the complex conjugate. Finally it is convenient to write the pressure in terms of the potential. For a liquid with $u = \nabla\phi$, it can be shown that $p = j\omega\rho\phi$. Hence it follows that

$$V(z) = \frac{\int (u_z^i \phi^r - u_z^r \phi^i) dS}{2 \int u_z^i \phi^{i*} dS} \quad (A6)$$

Note that for a perfect plane reflector located at the focal plane $z = 0$ of a lens, $\phi^r = \phi^i = \phi^{i*}$, and $u_z^r = -u_z^i$; therefore $V(z) = 1$.

REFERENCES

- [1] A. Atalar, "An angular spectrum approach to contrast in reflection acoustic microscopy," *J. Appl. Phys.*, vol. 49, pp. 5130-5139, Oct. 1978.
- [2] H. K. Wickramasinghe, "Contrast and imaging performance in the scanning acoustic microscope," *J. Appl. Phys.*, vol. 50, pp. 644-668, Feb. 1979.
- [3] R. D. Weglein, "Metrology and imaging in the acoustic microscope," in *Scanned Image Microscopy*, E. A. Ash, Ed. London: Academic, 1980.
- [4] J. Kushibiki and N. Chubachi, "Material characterization by line-

focus-beam acoustic microscopy," *IEEE Trans. Sonics Ultrason.*, vol. SU-32, pp. 189-212, Mar. 1985.

- [5] W. Parmon and H. L. Bertoni, "Ray interpretation of the material signature in the acoustic microscope," *Elect. Lett.*, vol. 15, pp. 684-686, 1979.
- [6] A. Atalar, "A physical model for acoustic material signature," *J. Appl. Phys.*, vol. 50, pp. 8237-8239, 1979.
- [7] J. Kushibiki, A. Ohkubo, and N. Chubachi, "Acoustic anisotropy detection of materials by acoustic microscope using line-focus-beam," in *Proc. IEEE Ultrason. Symp.*, 1981, pp. 552-556.
- [8] J. Kushibiki, K. Horii, and N. Chubachi, "FFT velocity measurement of multiple leaky waves by line-focus-beam acoustic microscope," in *Proc. IEEE Ultrason. Symp.*, 1983, pp. 637-640.
- [9] H. L. Bertoni, "Ray-optical evaluation of $V(z)$ in the reflection acoustic microscope," *IEEE Trans. Sonics Ultrason.*, vol. SU-31, no. 2, pp. 105-116, Mar. 1984.
- [10] P. M. Morse and H. Feshbach, *Method of Theoretical Physics*. New York: McGraw-Hill, 1953.
- [11] I. J. Cox, D. K. Hamilton, and C. J. R. Sheppard, "Observation of optical signature of materials," *Appl. Phys. Lett.*, vol. 41, no. 7, pp. 604-606 Oct. 1982.
- [12] J. A. Hildebrand, K. Liang, and S. D. Bennett, "Fourier-transform approach to material characterization with the acoustic microscope," *J. Appl. Phys.*, vol. 54, no. 12, pp. 7016-7019, Dec. 1983.
- [13] K. Liang, S. D. Bennett, B. T. Khuri-Yakub, and G. S. Kino, "Precision phase measurements with the acoustic microscope," *IEEE Trans. Sonics Ultrason.*, vol. SU-32, pp. 000-000, Mar. 1985.
- [14] G. Mott, "Reflection and refraction coefficients at a fluid-solid interface," *J. Acoust. Soc. Am.*, vol. 50, no. 3, pp. 819-829, 1971.
- [15] F. L. Becker and R. L. Richardson, "Influence of material properties or Rayleigh critical-angle reflectivity," *J. Acoust. Soc. Am.*, vol. 51, no. 5, pp. 1609-1617, 1972.
- [16] T. Bourbie, "Effects of attenuation on reflections," Ph.D. Thesis, Stanford University, Stanford, CA, April 1982.
- [17] N. I. Akhiezer, *Theory of Approximations*. New York: Ungar, 1956.
- [18] A. Papoulis, "A new algorithm in spectral analysis and band-limited extrapolation," *IEEE Trans. Circuits and Systems*, vol. CAS-22, no. 9, pp. 735-742 Sept. 1975.
- [19] G. S. Kino and B. A. Auld, "Reciprocity theories for flaw analysis," ARPA/AFML annual review of progress in quantitative NDE, Cornell University, Ithaca, NY, 1977.
- [20] B. A. Auld, "General electromechanical reciprocity relations applied to the calculation of elastic-wave scattering coefficients," in *Wave Motion*, vol. 1. Amsterdam: North-Holland, 1979, pp. 3-10.
- [21] G. S. Kino, "The application of reciprocity theory to scattering of acoustic waves by flaws," *J. Appl. Phys.*, vol. 49, no. 6, pp. 3190-3199, June 1978.
- [22] R. L. Jungerman, P. C. D. Hobbs, and G. S. Kino, "Phase sensitive scanning optical microscope," *Appl. Phys. Lett.*, vol. 45, no. 8, pp. 846-848, Oct. 1984.
- [23] J. Fraser and C. Desilets, Precision Acoustic Devices, Inc., Palo Alto, CA, private communication.

Kenneth K. Liang was born in Hong Kong in 1954. He received the B.S.E.E. degree from the University of Minnesota, Minneapolis, MN, in 1976.

He is currently finishing his doctoral dissertation in electrical engineering at Stanford University, Stanford, CA. His current interests are in the application of acoustic imaging techniques to non-destructive testing.





Gordon S. Kino (S'52-A'54-SM'63-F'66) was born in Melbourne, Australia on June 15, 1928. He received the B.Sc. and M.Sc. in mathematics at London University, England, and the Ph.D. in electrical engineering at Stanford University, Stanford, CA.

He is Professor of Electrical Engineering and Professor by Courtesy of Applied Physics at Stanford University. He has worked on microwave tubes, electron guns, plasmas, and the Gunn effect. His current interests are in microwave acous-

tics and acoustic and fiber optic techniques for medical instrumentation, nondestructive testing, and signal processing.

Dr. Kino was a Guggenheim Fellow in 1967 and is a Fellow of the American Physical Society, AAAS, and a member of the National Academy of Engineering.



Butrus T. Khuri-Yakub (S'70-M'76) was born in Beirut, Lebanon. He received the B.S. degree in 1970 from the American University of Beirut, the M.S. degree in 1972 from Dartmouth College, Hanover, NH, and the Ph.D. degree in 1975 from Stanford University, Stanford, CA, all in electrical engineering.

He joined the research staff at the E. L. Ginzton Laboratory of Stanford University in 1976 as a Research Associate. He was promoted to a Senior Research Associate in 1978, and to a Professor of Electrical Engineering (research) in 1982. His current research interests include thin-film deposition, surface acoustic wave devices, bulk-wave transducers and arrays, nondestructive evaluation of structural materials, acoustic imaging, and photo-acoustic interactions.

Dr. Khuri-Yakub is a member of the Acoustical Society of America.

446

These two signals L and R differ slightly in path length in the water, but otherwise experience much the same environmental disturbances. However, the Rayleigh wave component has substantial phase delay over the surface of the solid material. Hence, the effective path length for the R signal is longer than that for the specular reflection L. Indeed, in our experiments, we use the different arrival times of these two return signals to facilitate their separation and subsequent phase comparison. The exciting signal is two to three cycles in duration, and the defocus distance is sufficient so that there is no temporal overlap of the signals. It is clear that changes in the Rayleigh wave velocity as a function of position along the surface of the specimen may be sensed in this way. By combining a high-accuracy phase measurement scheme with a suitably extended Rayleigh wave path, remarkably sensitive measurements can be made.

The second operating configuration is illustrated in Fig. 1(b). In this case the lens is positioned so that its focus is at the surface of the specimen, or slightly above it, so that no Rayleigh wave of importance is excited. A reference path is provided by an annular beam that propagates through the flat outer periphery of the lens. By exciting the lens with a short pulse, and once again using time discrimination to separate the signals from the two different paths, an interferometer is formed. Small local changes in the surface topography result in large changes in the phase of the focused beam relative to the phase of the large diameter reference beam.

In both measurement configurations, it is apparent that the reference and signal pulses arrive at different times. This would ordinarily make phase comparison impossible; however, the phase measurement system described in the next section essentially reconstructs two phase-coherent, continuous signals which are directly related to the amplitudes and phases of the two time-distinct return signals.

The first configuration is also used where the signal of interest is the transducer output voltage when the system is being operated in the so-called $V(z)$ mode.⁶ In this case, the exciting signal has a much longer duration so that the return signals (L and R) overlap and interfere at the transducer, even for large defocus distances. The idea here is to measure both the amplitude and the phase of the signal relative to some reference as a function of the axial separation z between the acoustic lens and the specimen. The resulting complex $V(z)$ can be inverted^{7,8} to obtain the angular dependence of the reflectance of the liquid/specimen interface. From the reflectance function, various material property parameters can be extracted.

In most of the experiments described here, a center frequency of 50 MHz was used with an acoustic transducer having 20% bandwidth. The lens material was fused quartz and had a radius of curvature of 3.2 mm, giving a focal length in water of 4.24 mm. The opening aperture of the lens was 5.0 mm in diameter, corresponding to a maximum half angle of 36° or an f number of 0.85.

II. PHASE MEASUREMENT SYSTEM

The phase of a short rf pulse is difficult to measure directly because the corresponding Fourier spectrum is a con-

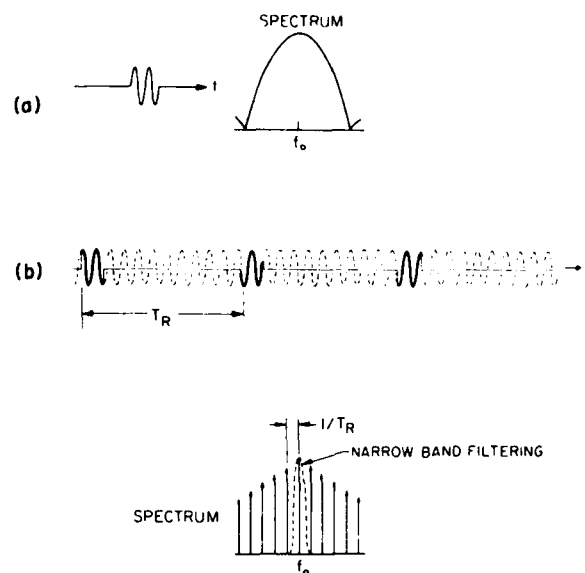


FIG. 2. Fourier spectra of a single rf pulse and a synchronous pulse train.

tinuous spread of spectral components, as shown in Fig. 2(a). Only a minute amount of power is associated with the frequency ω_0 of the rf carrier from which the pulse is derived. An acoustic microscope, however, is excited repetitively at a constant rate and the rf pulses occur as a pulse train. If the pulses are coherent in the sense that they originate from a single cw signal, as depicted in Fig. 2(b), the time waveform can be regarded as a periodically sampled cw signal. The corresponding Fourier spectrum consists of discrete frequency components spaced by the repetition rate ω_r . The frequency component situated at ω_0 can easily be extracted by narrow-band filtering, as shown. In essence, a cw replica of the pulse-modulated rf signal is generated to facilitate phase measurement.

Figure 3 shows the configuration of the phase measurement system used to carry out precision phase measurement with a 50-MHz acoustic microscope. The basic scheme involves signal recovery by synchronous detection and subsequent phase measurement with a lock-in amplifier.

The signal source is a single sideband (SSB) generator with synchronous cw outputs at 100 kHz, 10.6, and 10.7

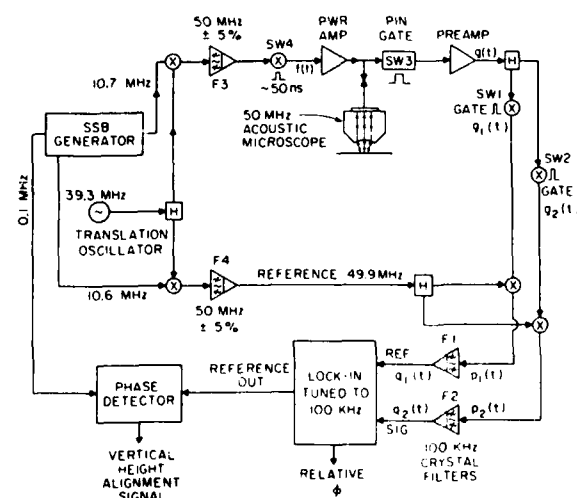


FIG. 3. Schematic for the phase measurement system.

MHz. The 10.7-MHz output is derived from the upper sideband component of the product of the 100 kHz and 10.6 MHz signals. The companion lower sideband at 10.5 MHz is suppressed by at least 50 dB using a standard FM radio system IF filter. The translating oscillator shifts the operating frequency up to the center frequency of the acoustic transducer, which is 50 MHz in this example. A 49.9-MHz reference signal is also generated. Again the lower sideband components of the product signals have to be removed. However, the filtering requirement is not as stringent as in the SSB generator and tunable bandpass filters (F3 and F4) with 5% bandwidth are adequate since the sideband components are well separated in this case. This signal generation scheme is flexible in that the operating frequency is tunable over a fairly wide range, up to 100 MHz. For a higher frequency of operation, F3 and F4 can be replaced with bandpass filters with better selectivity. An alternative approach is to add successive heterodyning and filtering stages to step up incrementally to the desired operation frequency.

The 50-MHz cw signal is time gated (SW4) to produce a short tone burst to excite the acoustic transducer. Switch SW3 is used as a time gate to pass only the low-level acoustic return signals of interest, and to block high-level extraneous ones which might damage the preamplifier. The gated acoustic return signal $g(t)$ typically consists of two time-separated rf pulses $g_1(t)$ and $g_2(t)$, whose relative phases are to be measured. For example, in the case of surface acoustic wave velocity perturbation measurements, the relative phase between the on-axis return pulse and the converted leaky Rayleigh wave pulse is measured. Alternatively, for topography measurements, the relative phase between the focused beam signal and the unfocused ring beam signal gives the local height of the sample. In either case, the non-overlapping pulses are electrically separated through time gating by SW1 and SW2 into two channels, as shown. Each of them is mixed with the 49.9 MHz reference, and the product is narrowband filtered (F1 and F2) to extract the 100-kHz component.

It will be shown in Sec. IV that the 100-kHz signals $q_1(t)$ and $q_2(t)$ are essentially low-frequency cw replicas of the pulse-modulated rf acoustic signals $g_1(t)$ and $g_2(t)$, bearing identical amplitude and phase information. With a bi-phase lock-in amplifier tuned to 100 kHz, we can measure the phase difference between the two signals, and also the amplitude of the signal fed to the signal channel of the lock-in, if it is required. The phase sensitivity of the system is essentially limited by the lock-in amplifier since, in most cases, the problem of system noise can be overcome by increasing the integration time in the lock-in output stage, thus effectively reducing the noise bandwidth, with the obvious disadvantage of longer data acquisition time. Good quality lock-in amplifiers routinely have phase resolutions of 0.1° , which translates into an overall system phase sensitivity of $1/3600$ of a wavelength.

III. APPLICATIONS

A. Velocity perturbation due to thin-film overlay

The operating configuration shown in Fig. 1(a) is used to determine the change in Rayleigh wave propagation ve-

locity as a result of material property change. The sample in this example is a multiple-thickness indium film deposited on glass. The thicknesses are 240 and 620 Å, respectively. The objective was to measure the perturbation of the Rayleigh wave velocity caused by the indium film. A line scan over the surface of the sample (Fig. 4) exhibits phase changes of 7° and 11° for the 240- and 380-Å step changes in film thickness. The spatial resolution of the system is defined by the Rayleigh wave path length on the substrate and is determined to be about 0.8 mm from the step transition in the line scan. It can be calculated from first-order perturbation theory⁹ that the velocity perturbation due to the indium film is 0.18% and 0.46%, respectively, for the 240- and 620-Å layers. Based on these estimated parameters, one would expect phase changes of 7.6° and 12° for the 240- and 380-Å step transitions. Hence, there is fairly good agreement between the experimentally obtained and theoretically predicted phase changes. It should also be noted that in the line scan, the small phase variations in the supposedly flat regions of the indium film are real and repeatable. The fluctuations are less than 0.5° and are due to nonuniformity in the thickness of the indium film. Since the phase sensitivity of the system is limited by the lock-in amplifier to 0.1° , this measurement technique can potentially detect velocity perturbations on the order of one part in 10^5 . Conversely, if the material property parameters are known, we can determine film thicknesses accurately from the velocity perturbation measurements.

In this operating configuration, the measured phase is dependent on the distance between the lens and the specimen. This distance changes with the sample surface topography and is susceptible to thermal drift as well, thus introducing phase error into the measurement. To minimize this error, a feedback mechanism is employed to keep the lens-to-specimen spacing constant. The acoustic lens is mounted on

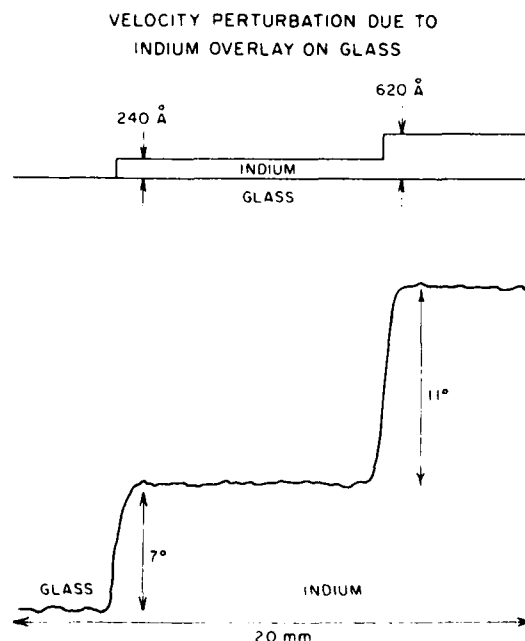


FIG. 4. Measurement of velocity perturbation due to indium film on glass.

a piezoelectric (PZT) stack so that its vertical position can be adjusted continuously by an electronic control signal. The acoustic on-axis reflection pulse, whose phase is a direct measure of the lens-to-sample distance, is applied to the reference channel of the lock-in amplifier, as shown in Fig. 3. The reference channel generates a 100-kHz constant-amplitude, phase-locked replica of the reference input, which is then compared with the 100-kHz output of the SSB generator to produce the control signal for the PZT stack. In operation, the acoustic lens automatically tracks the surface topography of the sample during scanning to ensure that the measured phase change is due to material property variation alone.

B. Surface topography measurements

We have used the acoustic microscope in the measurement configuration shown in Fig. 1(b) as a high-resolution noncontacting profilometer.^{10,11} Topography images of metallized stripe patterns on a fused silica substrate are shown in Figs. 5(a), 5(b), and 5(d). The patterns have progressively finer pitches and the linewidths are 250, 125, and 62.5 μm , respectively. The metallization is gold with a thickness of about 3000 Å. The gold stripes show up as bright areas in the images. At 50 MHz, with an F# of 0.85 and a uniformly excited aperture, the Rayleigh resolution of the acoustic lens is $1.13F\lambda = 0.96\lambda$ or 29 μm , while the 3-dB resolution is $0.64F\lambda = 0.54\lambda$ or 16 μm . The 62.5- μm line image in Fig. 5(d) is clearly resolved, as would be expected. The amplitude image of the 125- μm stripes is shown in Fig. 5(c) for comparison. There is virtually no contrast (less than 1%) to suggest the presence of a striped pattern, clearly illustrating that phase is a far more sensitive means of gauging distances. The measured phase difference between the surface of the metallization and the surface of the fused silica substrate is 8.3°, which corresponds to a film thickness of 2800 Å after taking into account the angular dependence of the complex reflectance function and the effect of focusing.

Providing the same fractional bandwidth can be maintained, there should be little difficulty in applying the same measurement techniques to acoustic microscopes operating

at a much higher frequency, perhaps up to 2 GHz. Beyond that frequency, limitations in the presently available electronic switching components may present difficulties.

C. Reflectance by inversion of complex $V(z)$

It has been demonstrated that the reflectance function at a liquid/solid interface can be obtained by inverting the corresponding complex $V(z)$ data.^{7,8} The principal motivation behind this endeavor is that one can obtain a lot of useful material property information from the reflectance function. The solid curves in Fig. 6 show the magnitude and the phase of the theoretical reflectance function of a water/fused silica interface. The reflectance function contains information on the longitudinal and shear critical angles, and thus the velocities of propagation of the respective modes in fused silica. Also, the Rayleigh critical angle corresponds to the point at which the phase is π radians in the region where the phase curve undergoes a rapid 2π radian change.

It can be shown that the relation between $V(z)$ and the reflectance function $R(\theta)$ is essentially one of Fourier transformation. The inversion formula is given by⁸

$$R(t) = \mathcal{F}^{-1}[V(u)]/P^2(t), \quad (1)$$

where $u = z/\lambda$ and $t = 2k_z/k$. The parameter k is the propagation constant in water, and k_r and $k_z = \sqrt{k^2 - k_r^2}$ are the corresponding propagation constants in the r and z directions, respectively. The parameter $P(t)$ is the pupil function of the acoustic lens; it describes the complex amplitude distribution of the focused acoustic beam as a function of angle θ where $\sin \theta = k_r/k_0$.

Generally, the lens pupil function P is not known *a priori*. However, it can be calibrated by measuring and then inverting the complex $V(z)$ for a material whose reflectance function has uniform amplitude and phase over the range of angular illumination covered by the acoustic lens.

The $V(z)$ measurements were conducted at 10 MHz. A water/lead interface, whose reflectance function is uniform in magnitude and phase out to $\theta = 40^\circ$, was used to calibrate the lens pupil function P . The experimental reflectance function of fused silica, which results from the inversion procedure, is superposed on Fig. 6 in dashed lines. The agreement is good between theory and experiment in both magnitude and phase. The measured shear critical angle at $\theta = 23.5^\circ$ and the Rayleigh critical angle at $\theta = 25.85^\circ$ compare extremely well with theoretical values.

IV. FOURIER ANALYSIS OF THE PHASE MEASUREMENT SYSTEM AND NOISE CONSIDERATIONS

Consider the signal recovery portion of the system in Fig. 3, starting from where the acoustic signal is received to the 100-kHz crystal filter output. Suppose the acoustic microscope is excited with a coherent rf pulse train of the form

$$f(t) = \cos \omega_0 t \sum_T \text{rect}\left(\frac{t - lT_p}{T_w}\right), \quad (2)$$

where ω_0 is the rf carrier frequency and $f_s = 1/T_p$ is the repetition rate of the system. The width of the excitation pulse T_w is made sufficiently short so that the acoustic re-

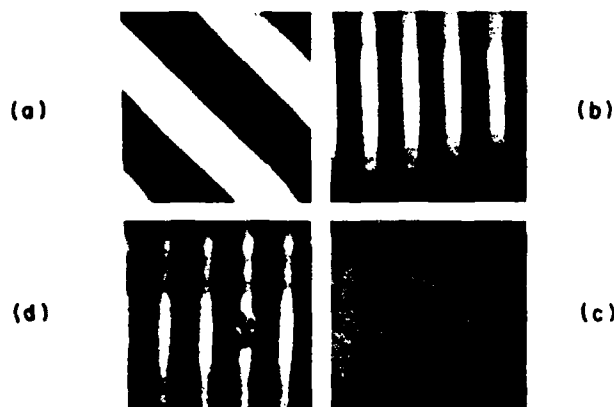


FIG. 5. Topography images of striped metallization patterns on a fused quartz substrate. The metallization is gold and the thickness is about 3000 Å. (a) phase image of 250- μm lines, (b) phase image of 125- μm lines, (c) amplitude image of 125- μm lines, (d) phase image of 62.5- μm lines.

FUSED SILICA

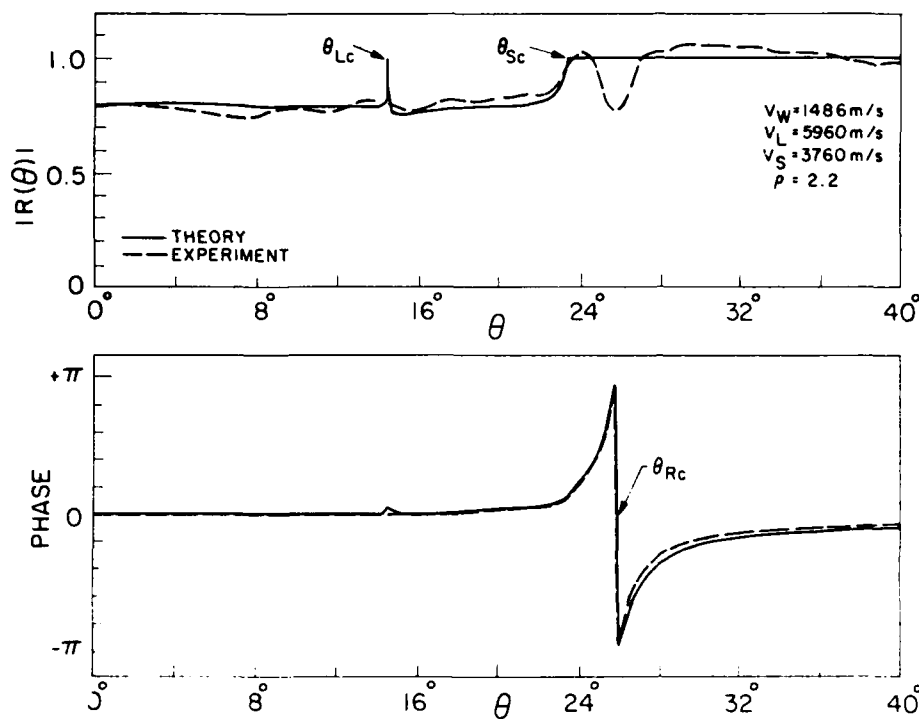


FIG. 6. Theoretical and experimental reflectance function for a water/fused silica interface obtained by the inversion of the corresponding complex $V(z)$.

turn pulses of interest are time separated. Typically, we would measure the relative phase between two such pulse trains, $g_1(t)$ and $g_2(t)$. In general, $g_1(t)$ and $g_2(t)$ are different acoustic responses to the excitation signal $f(t)$ and can be modeled by

$$g_1(t) = f(t) * h_1(t), \quad (3)$$

$$g_2(t) = f(t) * h_2(t),$$

where $h_1(t)$ and $h_2(t)$ are the respective impulse response functions, and "*" denotes convolution. $g_1(t)$ and $g_2(t)$ are separated by time gating for processing in parallel channels, as shown in Fig. 3.

The frequency spectrum of the signal in each processing channel is given by

$$G_i(\omega) = \frac{A \operatorname{sinc}[T_w(\omega + \omega_0)/2\pi] H_i(\omega)}{2} \times \sum \delta(\omega + \omega_0 - l\omega_s) + \frac{A \operatorname{sinc}[T_w(\omega - \omega_0)/2\pi] H_i(\omega)}{2} \times \sum \delta(\omega - \omega_0 - l\omega_s), \quad (4)$$

where $H_i(\omega)$ is the Fourier transform of $h_i(t)$, and i is the channel index. The magnitude spectrum $|G_i(\omega)|$ is depicted in Fig. 7(a).

The multisideband signal $g_i(t)$ is heterodyned down to a center frequency of $\omega_{IF} = \omega_0 - \omega_R$. The corresponding spectrum $|P_i(\omega)|$ is shown in Fig. 7(b). We have to be careful about aliasing because of the overlap between the discrete

spectral islands centered at $\pm \omega_{IF}$. With a correct choice of ω_{IF} and the repetition rate ω_s , as discussed below, the discrete frequency components situated at $\pm \omega_{IF}$ can be extracted by a narrow bandpass filter to produce a cw output $q_i(t)$,

$$q_i(t) = K |H_i(\omega_0)| \cos[\omega_{IF}t + \theta_i(\omega_0)], \quad (5)$$

where $\theta_i(\omega_0) = \arg H_i(\omega_0)$. The signal $q_i(t)$ is in essence a low-frequency cw replica of the rf pulse $g_i(t)$ in the sense that it contains the same amplitude and phase information as the rf carrier frequency ω_0 of the acoustic signal. The signals $q_1(t)$ and $q_2(t)$ are then used as the reference and signal inputs to a lock-in amplifier where the relative phase $\theta_1(\omega_0) - \theta_2(\omega_0)$ is measured.

It is evident from Fig. 7(b) that the choice of the repeti-

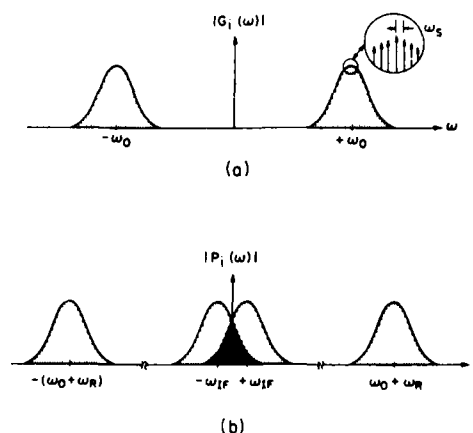


FIG. 7. Magnitude spectra (a) of the gated periodic rf signal, (b) after mixing with the reference frequency.

tion rate ω_s of the phase measurement system is crucial to the faithful extraction of the discrete frequency components at $\pm \omega_{IF}$ in $P_i(\omega)$. The following condition needs to be satisfied to avoid aliasing:

$$2\omega_{IF} \neq n\omega_s, \quad n = 1, 2, 3, \dots \quad (6)$$

Practical narrowband filters have finite bandwidth that must be taken into account in aliasing considerations. Since filter response time is inversely proportional to the bandwidth, it is desirable to utilize the largest bandwidth possible in order to minimize settling time. Therefore, ω_s should be chosen so that

$$\omega_s = 2\omega_{IF}/n + 1/2 \quad (7)$$

to give a maximum bandwidth of ω_s for F1 and F2.

Next we consider the effect of additive, Gaussian noise on the phase resolution of the measurement system. A detailed noise analysis of the system is omitted for brevity. It is well known that the signal-to-noise ratio (S/N) is conserved in heterodyning, and that removing the unnecessary bandwidth from a narrowband signal improves the S/N.

Let S_i/N_i be the signal-to-noise ratio of the acoustic input signal to the time gate SW2 in Fig. 3. It can be shown that the S/N at the output of the 100-kHz crystal filter F2 is given by the relation¹²

$$\frac{S_F}{N_F} = \frac{1}{2} \frac{B_i}{B_F} \frac{S_i}{N_i}, \quad (8)$$

where B_F is the bandwidth of the filter. Equation (8) clearly shows the improvement in S/N by reducing the noise bandwidth from B_i to B_F , as one would expect.

It can also be shown that the corresponding root-mean-square phase noise at the output of the crystal filter F2 is given by the relation¹²

$$(\Delta\theta_{RMS})^2 = 1/(S_F/N_F). \quad (9)$$

The low-pass filter at the output stage of the lock-in amplifier can further reduce the phase noise if its equivalent noise bandwidth B_L is such that $2B_L < B_F$. If the reference channel input is noise free, $\Delta\theta_{RMS}$ at the lock-in output is given by

$$(\Delta\theta_{RMS})^2 = \frac{\min(B_F, 2B_L)}{B_F} \frac{1}{S_F/N_F} = \frac{1}{S_0/N_0}, \quad (10)$$

where S_0/N_0 , defined as the equivalent output signal-to-noise ratio, is

$$\frac{S_0}{N_0} = \frac{1}{2} \frac{B_i}{\min(B_F, 2B_L)} \frac{S_i}{N_i}. \quad (11)$$

When the reference channel input is also noisy, the phase noise power spectrum is simply the sum of the power spectra of the signal and reference channel inputs

$$\begin{aligned} (\Delta\theta_{RMS})_{TOTAL}^2 &= (\Delta\theta_{RMS})_{SIG}^2 + (\Delta\theta_{RMS})_{REF}^2 \\ &= \frac{1}{S_0/N_{0SIG}} + \frac{1}{S_0/N_{0REF}} = \frac{1}{S_0/N_{0TOTAL}}, \end{aligned} \quad (12)$$

where $(S_0/N_0)_{REF}$ is the equivalent output S/N of the ref-

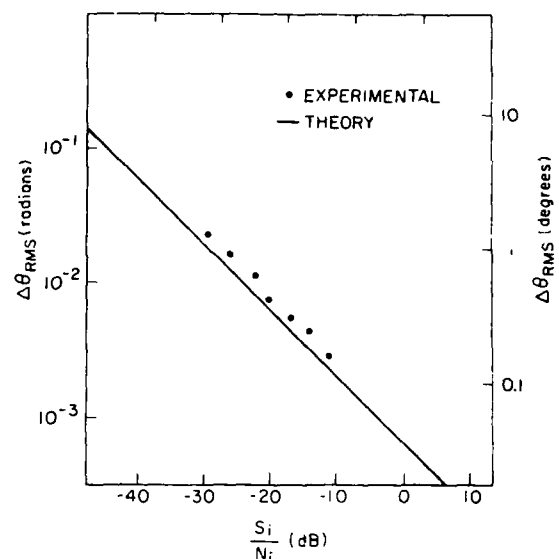


FIG. 8. Experimentally measured phase noise as a function of the equivalent input noise.

ference channel input, and $(S_0/N_0)_{TOTAL}$ is the total equivalent output S/N.

Figure 8 shows the experimentally measured phase noise as a function of S_i/N_i . The measurement system is set up for $B_i = 300$ MHz, $B_F = 100$ Hz, $B_L = 25$ Hz; only the signal channel input is noisy. The input-to-output S/N improvement, as given by Eq. (11), is 65 dB, which is within 2 dB of our measurement. The experimental data exhibit clearly the inverse relationship between $\Delta\theta_{RMS}$ and S_i/N_i as predicted by theory.

The typical operating parameters for the 50-MHz acoustic microscope system are $B_F = 100$ Hz, pulse width $T_w = 100$ ns, and repetition period $T_p = 64$ μ s. The dominant source of noise is the thermal noise in the preamplifier following SW3 in Fig. 3. Suppose the preamplifier has a noise bandwidth of $B_i = 100$ MHz and a noise figure (NF) of 10 dB. Let us assume that there is a further 10-dB degradation in S/N ratio due to noise contribution along the signal path from the inputs of SW1 and SW2 to the inputs of the 100-kHz crystal filters F3 and F4. The effective NF referred to the input of the preamplifier is therefore 20 dB. At the preamplifier input, typically the signal level A is about 5 mV. The effective input S/N ratio is given by

$$\frac{S_i}{N_i} = \frac{A^2/2}{F_p \times 4kTB_iR} \frac{T_w}{T_p}, \quad (13)$$

where F_p is the total noise figure (power) and $k = 1.38 \times 10^{-23}$ J/K is Boltzmann's constant. At room temperature ($T = 300$ K), and for a 50- Ω system, S_i/N_i is about +4 dB. The corresponding S/N ratio at the crystal filter output is +62.7 dB from Eq. (8), which translates to a root-mean-square phase noise of $\Delta\theta_{RMS} = 0.04^\circ$ according to Eq. (10). Suppose that we have the same amount of phase noise at the outputs of F3 and F4. The theoretical phase resolution limit as given by Eq. (12) is 0.06° . Thus, under typical measurement conditions, we are operating fairly close to the phase resolution limit of the lock-in amplifier, which is 0.1° . In certain situations where the input S/N ratio

can be improved by increasing the signal duty cycle T_w/T_p , as in $V(z)$ measurements where signal pulses are several microseonds long, the lock-in amplifier becomes the limiting factor in the phase resolution of the measurement system. The lock-in amplifier has to be replaced by more precise phase measurement instrumentations in such cases in order to take full advantage of the corresponding reduction in phase noise.

V. DISCUSSION

We have described the basic principle and demonstrated the operation of a precision phase measurement system. Although the system is specifically designed for acoustic microscopy, its application can readily be extended to situations where precision phase measurement is required for synchronous periodic rf pulses as short as two or three cycles.

ACKNOWLEDGMENT

This work was supported by the Air Force Office of Scientific Research under Contract No. AFOSR-84-0063.

- ¹H. K. Wickramasinghe and M. Hall, *Electron. Lett.* **12**, 637 (1976).
- ²C. C. Lee, C. S. Tsai, and X. Cheng, *IEEE Trans. Sonics Ultrason.* **SU-32**, 248 (1985).
- ³S. D. Bennett and E. A. Ash, *Trans. Sonics Ultrason.* **SU-28**, 59 (1981).
- ⁴A. Atalar, *J. Appl. Phys.* **49**, 5130 (1978).
- ⁵H. K. Wickramasinghe, *J. Appl. Phys.* **50**, 664 (1979).
- ⁶A. Atalar, *J. Appl. Phys.* **50**, 8237 (1979).
- ⁷J. A. Hildebrand, K. Liang, and S. D. Bennett, *J. Appl. Phys.* **54**, 7016 (1983).
- ⁸K. Liang, G. S. Kino and B. T. Khuri-Yakub, *IEEE Trans. Sonics Ultrason.* **SU-32**, 213 (1985).
- ⁹B. A. Auld, *Acoustic Fields and Waves in Solids*, Vol. 2 (Wiley, New York, 1973), p. 278.
- ¹⁰K. Liang, S. D. Bennett, B. T. Khuri-Yakub, and G. S. Kino, DAR-PA/AF Review of Progress in Quantitative NDE, La Jolla, California, August 1982.
- ¹¹K. Liang, S. D. Bennett, B. T. Khuri-Yakub, and G. S. Kino, *Appl. Phys. Lett.* **41**, 1124 (1982).
- ¹²K. Liang, Ph.D. thesis, Stanford University, 1985.

Phase sensitive scanning optical microscope

R. L. Jungerman, P. C. D. Hobbs, and G. S. Kino

Edward L. Ginzton Laboratory, W. W. Hansen Laboratories of Physics, Stanford University, Stanford, California 94305

(Received 5 June 1984; accepted for publication 31 July 1984)

An electronically scanned optical microscope which quantitatively measures amplitude and phase is described. The system is insensitive to mechanical vibrations. The phase information makes it possible to measure surface height variations with an accuracy of better than 100 Å and can also be used to improve the lateral resolution.

Optical microscopy is widely used as a method of evaluating small scale surface features. In examining these features, both the lateral dimensions as well as the height are of interest. Conventional optical microscopy gives little quantitative information on surface height. Nomarski differential phase contrast,¹ as well as conventional phase contrast microscopy,² provides qualitative contrast for objects differing from their surroundings in optical phase rather than amplitude. However, it is very difficult to extract precise height information from these images.³ Interference microscopy⁴ involves the counting of fringes to evaluate surface height, but again the fringe maps are difficult to interpret.

We present here an electronically scanned optical microscope which directly measures the optical amplitude and phase of light reflected from a sample. The system incorporates internal references which make it insensitive to environmental vibrations which are a common problem in interferometers. Information from the linear scan is obtained in a form which is directly compatible with digital processing. Since both amplitude and phase are measured, it is possible to take a Fourier transform of the complex spatial variation. This can be used to remove aberrating effect in the optical system by Weiner filtering with the measured point spread function of the system. This should make it possible to more accurately determine the lateral dimensions of surface features,⁵ such as linewidths on integrated circuits.

On a sample of uniform composition, the optical phase can be simply calibrated to yield the height of surface features. Thus, the scanning microscope can be used as a non-contacting optical profilometer which provides height information similar to that obtained using a mechanical stylus profilometer. On inhomogeneous samples, compensation is required for phase and polarization changes on reflection.

Earlier work on optical profilometry using a differential technique,⁶ or by heterodyning, using a Zeeman laser⁷ does not make use of electronic scanning. In our system, a Bragg cell is used to frequency shift as well as to scan the optical beam. Line scan rates of over 10 kHz are possible with the present Bragg cell, provided the detection electronics can be designed to be sufficiently fast. This makes rapid image processing a possibility.

Two schematics of the optical system are shown in Fig. 1. A simplified version of the basic system, shown in Fig. 1(a), illustrates how a Bragg cell can be used to split and frequency shift the optical beam. Similar optical heterodyning with a Bragg cell has been used to detect acoustic surface vibrations.⁸ The acoustic intensity is adjusted so that the input beam is split equally between an undiffracted optical

beam of frequency f_0 and a Bragg diffracted beam upshifted to frequency $f_0 + f_B$, where f_B is the frequency of the input signal to the Bragg cell. A combination of a field lens to image the center place of the Bragg cell to the back focal plane of a microscope objective, and the objective itself, converts the angular deviation produced by the Bragg cell into a displacement of one of the optical spots on the sample. After reflection from the sample, the beams retrace their paths and reenter the Bragg cell. Half of the previously undiffracted beam is now down shifted by the Bragg cell to $f_0 - f_B$ and falls on a detector. In addition, half of the previously deflected beam passes through the Bragg cell with no further frequency shift and follows the same path to the detector. Thus, two signals at frequencies $f_0 + f_B$ and $f_0 - f_B$ interfere

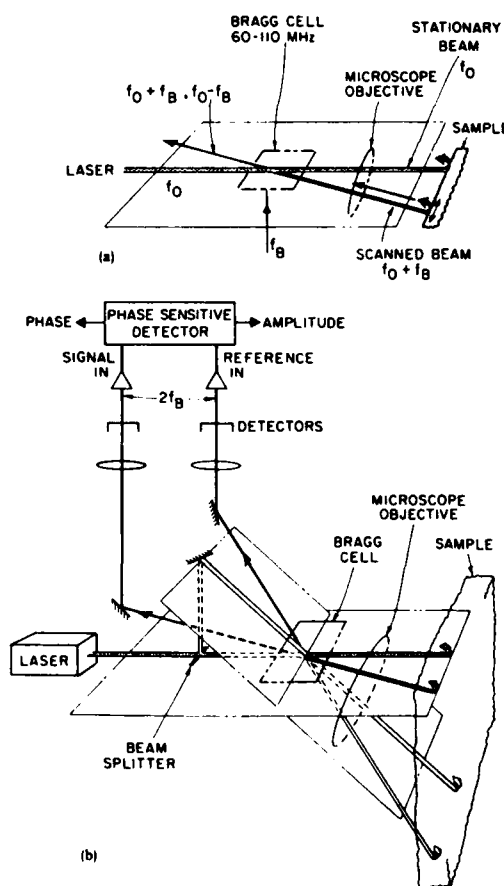


FIG. 1. Scanning optical microscope. The Bragg cell splits the input beam and scans the deflected and frequency shifted beam across the sample. The undiffracted beam is used as a reference. (a) Simplified schematic. (b) Secondary reference on sample to compensate for surface tilt.

at the detector to produce a difference frequency of $2f_B$. The phase of the signal at $2f_B$ depends on the optical path length difference between the two beams impinging on the sample, since the optical signals at $f_0 + f_B$ and $f_0 - f_B$ originate from the scanned and stationary spots on the sample, respectively.

For plane wave illumination, a surface height variation of h will introduce an optical phase change of $2kh$ as the beam is scanned over a feature of height h . For a tightly focused beam, the observed phase change is less since much of the incident light arrives at the sample at off-normal incidence. By integrating over a uniformly illuminated spherical lens aperture, it can be shown that the feature introduces a phase change of

$$\Delta\phi = kh(1 + \cos \theta_0), \quad (1)$$

where θ_0 is the half-angle of the objective aperture, and $k = 2\pi/\lambda$. As θ_0 approaches zero, this formula reduces to the phase change for a plane wave. Changes in the distance from the lens to the sample do not affect the measurement since only path length differences between the two beams are important. Thus, mechanical vibrations in the lens spacing do not disturb the measurements so long as they are less than the depth of focus of the objective. In the simplest configuration [Fig. 1(a)], the measurement is sensitive to surface tilt.

To measure the phase shift in the interference signal at $2f_B$ as the Bragg cell frequency f_B is varied over the scan range, an electronic reference signal is required. Simply frequency doubling the Bragg cell drive signal is not sufficient since the finite acoustic delay in the Bragg cell will produce a large linear phase shift as the Bragg frequency is changed. Instead, a second optical signal is generated [Fig. 1(b)] by splitting the beam incident on the Bragg cell in a direction perpendicular to the direction of acoustic wave propagation. Thus, four spots are focused on the sample. If the sample geometry is chosen so that the second set of spots is located on a uniform flat section of the sample, then they can be used for a reference. Alternatively, the second set of spots can be magnified to be much larger than the size of surface features of interest and placed anywhere on the sample.

The Bragg cell is imaged on a photodiode detector to compensate for the variation of the Bragg angle with frequency. Due to the use of a coherent detection scheme, the system is a type II confocal microscope.⁹ The Rayleigh resolution of $0.57 \lambda / \text{NA}$ is slightly better than the resolution of $0.61 \lambda / \text{NA}$ of the incoherent microscope.¹⁰ The ripples observed while scanning across a discontinuity are reduced over that of an incoherent type I system.¹⁰

Figure 2 shows the signal processing used to detect the amplitude and phase of the optically derived signals at $2f_B$. Since it is advantageous to detect phase at a fixed frequency, the reference signal is first limited and then single sideband modulated at an intermediate frequency of 60 MHz. Mixing this reference with the signal photodetector output gives a fixed frequency signal at 60 MHz which contains all the amplitude and phase information. In our initial experiments, a vector voltmeter is used to compare this signal to an electronic reference.

Calibration scans are performed on an optical flat and amplitude and phase variations due to the electronics as well

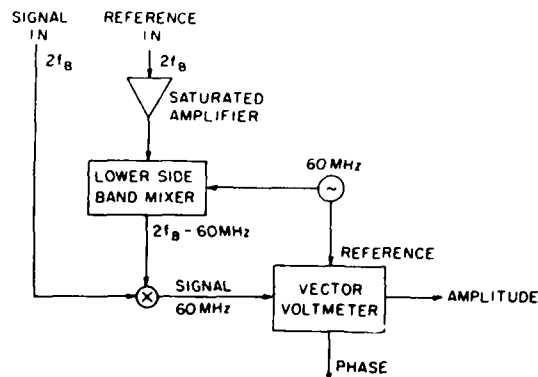


FIG. 2. Phase measurement system. Phase detection is performed at a fixed frequency of 60 MHz.

as optical aberrations are divided out and subtracted out, respectively. After this calibration, scans across a flat uniform sample show amplitude variations less than 3% and phase variations of less than 5° , suggesting a minimum surface height sensitivity of better than 100 Å.

In our experiments, 5 mW from an etalon controlled single-frequency argon-ion laser at 510 nm was used. The TeO_2 Bragg cell¹⁰ has a bandwidth of 60–110 MHz and deflection angles of 3° – 6° . Microscope objectives with numerical apertures in the range of 0.1–0.86 were used. The length of the scan on the sample is proportional to the frequency change times the objective focal length. With the higher numerical aperture, a $1/e^2$ spot radius of $1 \mu\text{m}$ was measured by examining the reflection from a metallized edge.

Figure 3 demonstrates an initial experiment on the application of the microscope to optical profilometry. In order to check the system performance, our aim was to eliminate phase changes due to the use of a wide aperture lens caused by polarization effects and changes in phase of the reflection coefficient. A step of aluminum 900 Å thick (as measured

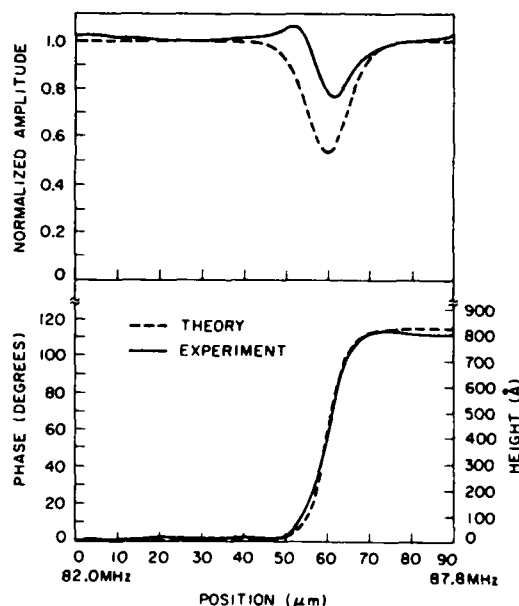


FIG. 3. Amplitude and phase variation across an aluminum step on a metallized substrate. The phase step indicates a height of 820 Å.

with a mechanical stylus) was deposited on a glass substrate metallized with 500 Å of aluminum. To simulate plane wave illumination, a long focal length microscope objective (16-mm focal length) was illuminated with a narrow beam less than 1 mm in diameter. This yields an effective numerical aperture of less than 0.03 and $\theta_0 \approx 0$ in Eq. (1). The Bragg cell frequency was scanned over the range of 82.0–87.8 MHz, causing the focused beam to scan across 90 μm on the sample. In Fig. 3, the amplitude and phase of the scanned spot are shown. After calibration, 5° of phase offset has been subtracted from the experimental phase curve. The theoretical curves are evaluated numerically for a Gaussian beam with a $1/e^2$ radius of 9 μm , which is consistent with the small numerical aperture of the lens used. The beam is assumed to have constant optical phase and is convolved across the phase step. Due to aberrations and misfocusing, there may be phase variations across the beam which could account for the discrepancy between the experimental and theoretical amplitude curves.¹²

The phase curve indicates a step height of 820 Å, which is in fair agreement with the mechanical stylus measurement of 900 Å, and demonstrates the ability to obtain good quantitative contrast on samples with features differing only in optical phase.

In conclusion, an electronically scanned optical microscope which can quantitatively measure amplitude and phase is demonstrated. Surface height variations can be accurately measured with the system. In addition, the ability to

measure optical phase promises to make possible digital filtering to remove the effect of aberrations and to accurately determine lateral dimensions on the sample.

The authors wish to thank B.T. Khuri-Yakub, S.D. Bennett, K. Liang, M. Amano, R. Stoddard, and J. Fox for their informative discussions. E. Roos provided the Bragg cell used in these experiments. This work supported by the Air Force Office of Scientific Research under contract No. F49620-79-C-0217.

¹D. L. Lessor, J. S. Hartman, and R. L. Gordon, *J. Opt. Soc. Amer.* **69**, 357 (1979).

²A. H. Bennett, H. Osterberg, H. Jupnik, and O. W. Richards, *Phase Microscopy, Principles and Applications* (Wiley, London, 1951).

³F. Beltrame, B. Bianco, and A. Chiabrera, *Proc. IEEE* **71**, 270 (1983).

⁴W. Krug, J. Rienitz, and G. Schulz, *Contributions to Interference Microscopy* (Hilger and Watts, London, 1951).

⁵M.E. Guillaume, N. M. Noailly, J. C. Reynaud, and J. L. Buevoz, presented at Fiber Optics and Laser Sensors II, Society of Photo-Optical Instrumentation Engineers, Arlington, Virginia, May 1984.

⁶H. K. Wickramasinghe, S. Ameri, and C. W. See, *Electron Lett.* **18**, 975 (1982).

⁷G. E. Sommargren, *Appl. Opt.* **20**, 610 (1981).

⁸R. M. De La Rue, R. F. Humphries, I. M. Mason, and E. A. Ash, *Proc. IEE* **119**, 117 (1972).

⁹C. J. R. Sheppard and A. Choudhury, *Opt. Acta.* **24**, 1051 (1971).

¹⁰G. S. Kino, in *Scanned Image Microscopy*, edited by E. A. Ash (Academic, London 1980), p. 1.

¹¹Crystal Technology, Palo Alto, California.

¹²K. Liang, R. L. Jungerman, and G. S. Kino (unpublished).

Depth response of confocal optical microscopes

T. R. Corle, C.-H. Chou, and G. S. Kino

Edward L. Ginzton Laboratory, W. W. Hansen Laboratories of Physics, Stanford University, Stanford, California 94305

Received July 7, 1986; accepted September 1986

The on-axis intensity response of a confocal scanning optical microscope was measured for an objective of numerical aperture 0.9. The data compare favorably with theoretical calculations obtained by numerical integration of the standard theory, provided that lens aberrations are taken into account. The invariance of the shape of the central lobe to surface roughness and tilt is also demonstrated.

The confocal scanning optical microscope (CSOM)¹ has been the subject of much recent study. One of the potentially most useful properties of this type of microscope for making film-thickness and -profile measurements is its shallow depth of field. We have measured the intensity response, $|V(z)|^2$, of a CSOM as a function of the amount of defocus of a plane reflector from the focal plane. We have found good agreement between the experimental results and the theory. We have also found that the shape of the central lobe is invariant to surface roughness and tilt in the sample. This property is potentially useful for remote distance sensing and other applications.

The amplitude $V(z)$ of the wave reaching a coherent detector in a confocal system has been determined by Liang *et al.*² and Sheppard *et al.*³ for the acoustic microscope and in scalar form by Wilson and Sheppard⁴ for the scanning optical microscope. We have derived a nonparaxial form of the vector field theory. This can be summarized as follows.

We assume a lens with a pupil function $P(\theta)$, where θ is the angle between the ray from the pupil plane to the focal point and the axis. By following the derivation of Richards and Wolf,⁵ with some minor changes, it can be shown that the transverse electric field associated with a plane wave focused by the lens to a point on axis a distance z beyond the focal plane is of the form

$$E(\theta, z) = \int_0^{\theta_0} \frac{(1 + \cos \theta) \sin \theta}{(\cos \theta)^{1/2}} \exp(ikz \cos \theta) P(\theta) d\theta. \quad (1)$$

It will be noted that there is a $(\cos \theta)^{1/2}$ term in the denominator rather than in the numerator, as in the theory of Richards and Wolf, in order to conserve power at a flat exit plane from the lens.

The integrand of Eq. (1) expresses the amplitude and phase of the plane wave components of the E field at an angle θ to the axis. When a focused beam is reflected from a plane mirror, its image will be a distance $2z$ away from the focus. In our apparatus, the reflected image is refocused onto the pinhole in front of the detector. Thus it is the field *on axis* at the focal plane of the objective lens that is imaged at the pinhole. This field is of the form

$$V(z) = \int_0^{\theta_0} \frac{(1 + \cos \theta) \sin \theta}{(\cos \theta)^{1/2}} \times \exp(-2ikz \cos \theta) P(\theta) R(\theta) d\theta. \quad (2)$$

In these expressions, $R(\theta)$ is the reflection coefficient of the plane reflector, k is the wave number ($2\pi/\lambda$), f is the focal length of the lens, and $\sin \theta_0$ is the numerical aperture of the lens. Given a lens of radius a with uniform excitation, $[P(\theta) = 1 \text{ for } \theta < \theta_0]$ for large ka and a plane reflector $[R(\theta) = 1]$. An approximate expression for $|V(z)|$ has been derived by Liang *et al.*²:

$$|V(z)| = \left| \frac{\sin kz(1 - \cos \theta_0)}{kz(1 - \cos \theta_0)} \right|. \quad (3)$$

This expression accurately predicts the shape of the central lobe; however, it fails to account for asymmetries in the sidelobes. The depth of focus is given by the 3-dB points of the central lobe in Eq. (3) (Ref. 2):

$$(\Delta z)_{3\text{ dB}} = \frac{0.45\lambda}{1 - \cos \theta_0}. \quad (4)$$

The basic technique for measuring optical $|V(z)|^2$ was outlined by Cox *et al.*⁶ In Fig. 1, the laser ($\lambda = 633 \text{ nm}$), the beam expander, and the iris diaphragm pro-

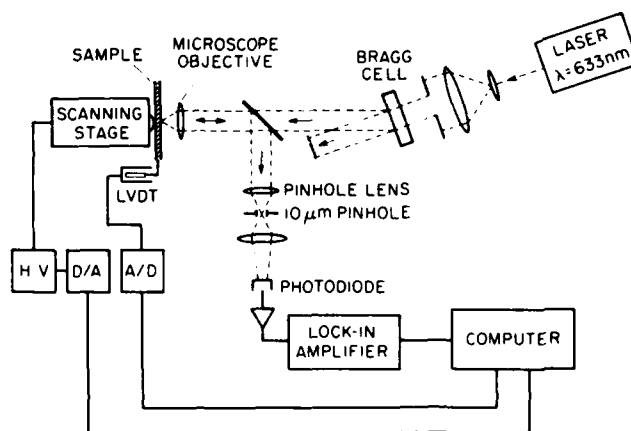


Fig. 1. Schematic diagram of apparatus. H.V., high-voltage power supply to drive scanning stage; D/A, digital-to-analog converter; A/D, analog-to-digital converter.

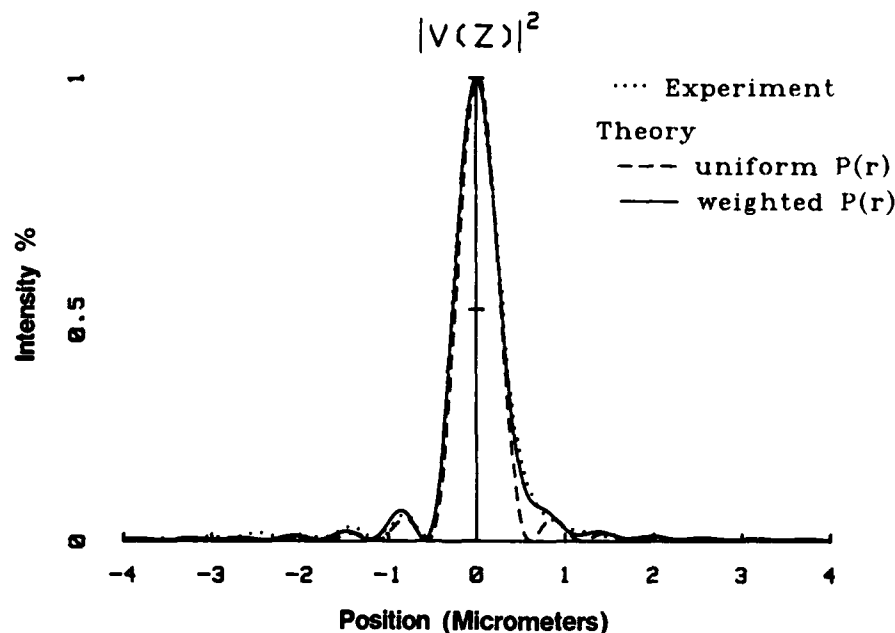


Fig. 2. $|V(z)|^2$ curve for objective of N.A. 0.9. Experimental data, dotted curve. Theoretical calculations, solid and dashed curves.

duce plane waves. The Bragg cell modulates the signal so that ac detection techniques may be employed. The plane waves are focused by a microscope objective onto an aluminum front-surface mirror. The light reflected from the mirror is then focused by another lens onto a pinhole and eventually onto a photodetector. The output of the photodetector is measured by a lock-in amplifier. The mirror is mounted on a piezoelectric transducer so that it can be scanned in the axial (z) direction. Its relative position is measured by using a linear variable differential transformer (LVDT).

The apparatus is computer controlled. The computer reads the mirror position and signal intensity. It then increments the voltage to the piezoelectric transducer, thereby moving the mirror and once again taking a data set. The computer repeats this operation for the full range of the piezoelectric transducer (about 12 m), taking data points approximately every 0.02 μm .

We present data for a microscope objective with a numerical aperture (N.A.) of 0.9 in air (dotted curve in Fig. 2). The z axis (position) is taken to be zero at the position of best focus, with positive values of z representing increased objective-sample separation. The 0.9-aperture data are similar to data published by Cox *et al.*⁶

The theoretical data were calculated by numerical integration of Eq. (2). In the integration, a uniform $R(\theta)$ was assumed. If the nonuniform $R(\theta)$ for aluminum is used, a more complex and time-consuming integral is generated. When evaluated, this integral does not noticeably change the results of Fig. 2. If a uniform pupil function $P(\theta)$ is assumed, the calculated $|V(z)|^2$ curves are nearly symmetrical about the position of best focus, as shown by the dashed lines in Fig.

2.⁶ This assumption, however, is not valid in our apparatus. Optical reflections due to antireflection-coating mismatches at 633 nm within a thick lens should generate some amplitude apodization. In addition, we expect that with a system focused on axis, there will be some spherical aberration. We therefore used a trial apodization function of the form

$$P(\theta) = \exp(A \sin^2 \theta) \exp(-jB \sin^4 \theta) \quad (\theta < \theta_0),$$

$$P(\theta) = 0 \quad (\theta > \theta_0), \quad (5)$$

where A is the amplitude coefficient and B is related to the Seidel coefficient for spherical aberration. We used $\sin \theta$ rather than θ in these approximations since the aperture is so large. We tried different values of A and B to obtain the best fit with the experimental results. The calculated result for $A = 0.2$ and $B = 6$ is shown by the solid curve in Fig. 2.

The phase error at the edge of the lens corresponds to 1.25π , well within the expected values for primary spherical aberration.⁷ The value of A indicates that the amplitude is increased by 17% at the edge of the lens. These curves illustrate that a relatively small amount of aberration can give rise to asymmetry in the $|V(z)|^2$ curves. With no aberrations, the $|V(z)|^2$ curves are symmetric. However, with aberrations, the $|V(z)|^2$ curves become asymmetric around $z = 0$, and the asymmetry reverses its shape with the sign of the aberration.

An interesting and important feature of the $|V(z)|^2$ curves, for sensing applications with low-numerical-aperture long-focal-length lenses, is their insensitivity to surface roughness and tilt. This insensitivity arises because the point illuminated on the reflector is still a point, even if the reflector is a rough surface. In this case, the reflected light is scattered over a wide angu-

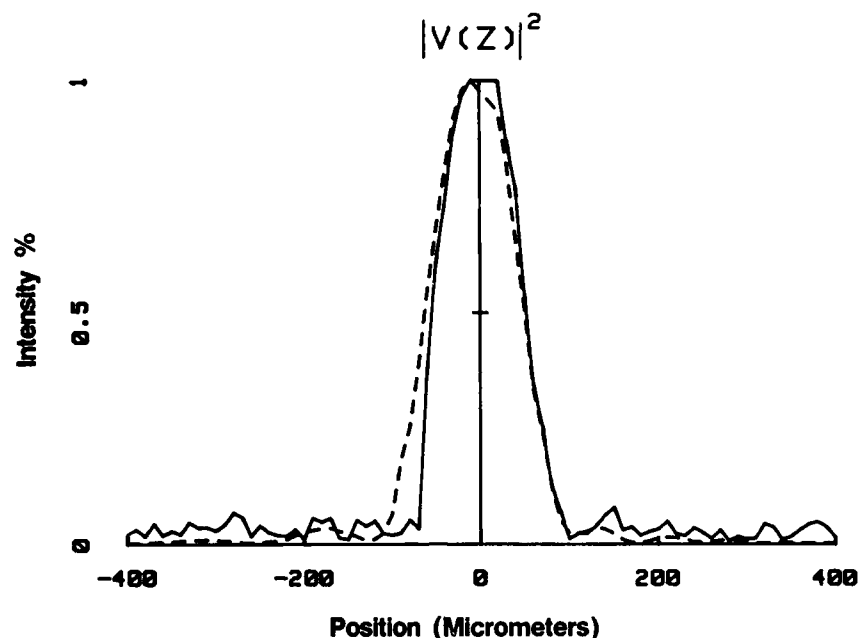


Fig. 3. $V(z)$ curve for a rough substrate tilted at an angle of 5° (solid curve). Reflections from a mirror, dashed curve.

lar range, but an image of the focal point, albeit reduced in intensity, is obtained at the pinhole. In our apparatus, the mirror in Fig. 1 was replaced with a quartz flat, which had been roughened using $5\text{-}\mu\text{m}$ grit and coated with 150 nm of gold. This sample is typical of a machined surface. The sample was then tilted at an angle of 5° from a plane normal to the z axis of our system.

A $|V(z)|^2$ trace was made using a N.A. = 0.07 lens (solid curve in Fig. 3). A 0.07 lens was used because it had a spot size considerably larger than the average surface roughness and hence would generate a diffuse reflection. The central lobe of this curve is unchanged from the central lobe obtained using an aluminum mirror, as shown by the dashed curve in Fig. 3. The peak value is, however, 66 dB below the value obtained with a mirror, indicating that this signal is generated primarily by diffuse reflection. The result in Fig. 3 also gives a signal-to-noise ratio of approximately 90 dB for this system. The stability and sharpness of the $|V(z)|^2$ curves make these curves useful in remote distance sensing applications on a variety of surfaces.

A depth-of-focus curve, $|V(z)|^2$, for a CSOM has been presented for a numerical aperture of 0.9. Theoretical calculations based on reasonable assumptions are presented as well and are shown to be in good agreement with the experimental data. The $|V(z)|^2$

curves are invariant to surface roughness and tilt. This feature has potentially far-reaching applications in the areas of optical range finding for distances from micrometers to meters.

This research was supported by the U.S. Air Force Office of Scientific Research under contract no. AFOSR-84-0063C. The research of T. R. Corle was supported by an IBM Graduate Predoctoral Fellowship for the duration of the research.

References

1. C. J. R. Sheppard, in *Imaging Modes of Scanning Optical Microscopy*, E. A. Ash, ed. (Academic, New York, 1980).
2. K. Liang, G. S. Kino, and B. T. Khuri-Yakub, *IEEE Trans. Sonics Ultrason.* **SU-32**, 213 (1985).
3. C. J. R. Sheppard and T. Wilson, *Appl. Phys. Lett.* **38**, 858 (1981).
4. T. Wilson and C. J. R. Sheppard, *Theory and Practice of Scanning Optical Microscopy* (Academic, London, 1984).
5. B. Richards and E. Wolf, *Proc. R. Soc. London Ser. A* **253**, 358 (1959).
6. I. J. Cox, D. K. Hamilton, and C. J. R. Sheppard, *Appl. Phys. Lett.* **41**, 604 (1981).
7. M. Born and E. Wolf, *Principles of Optics*, 6th ed. (Pergamon, Oxford, 1983).

From: REVIEW OF PROGRESS IN QUANTITATIVE
NONDESTRUCTIVE EVALUATION, Vol. 6A
Edited by Donald O. Thompson and Dale E. Chimenti
(Plenum Publishing Corporation, 1987)

OPTICAL RANGE FINDER

G. Q. Xiao, D. B. Patterson, and G. S. Kino

Edward L. Ginzton Laboratory
W. W. Hansen Laboratories of Physics
Stanford University
Stanford, California 94305

INTRODUCTION

Recently, a great deal of interest has been shown in making accurate range measurements with good transverse definition. This capability makes it possible, in machine vision systems, to extract geometrical shape information from the images. In robot position sensing, it is important to determine the absolute distance instead of distance change so that noncontinuous measurements can be made without the need for calibration at start-up. A third application of great importance is to measure the shape and size of machined parts with a noncontacting sensor.

Research in the area of distance measurements has been carried out for many years using several different techniques.¹ One technique is to use interferometry, which requires a high-quality laser. The method yields excellent range accuracy, but suffers from phase wraparound; thus, without additional complexity, such as the use of two laser frequencies or the employment of extremely high-frequency modulation, it is not possible to make noncontinuous distance measurements.² An alternative technique is to use a triangulation; this method does not usually provide very good transverse resolution and is attractive only when the accuracy requirement is on the order of 100 μm or greater.

In this paper, we describe a new optical technique which is based upon the type II microscope.^{3,4} With this system, we have made absolute distance measurements with a range accuracy of 2 μm and a transverse definition of 10 μm at a working distance of 15 cm. The system is stable, easy to align, and largely insensitive to the tilt and roughness of the object.

THEORY AND EXPERIMENTAL SET-UP

A schematic diagram of the optical range finder is shown in Fig. 1. The objective lens focuses the laser beam to a spot of the order of 5 μm diameter, so that most of the beam passes through a 10 μm diameter pinhole. A camera lens placed beyond the pinhole focuses the

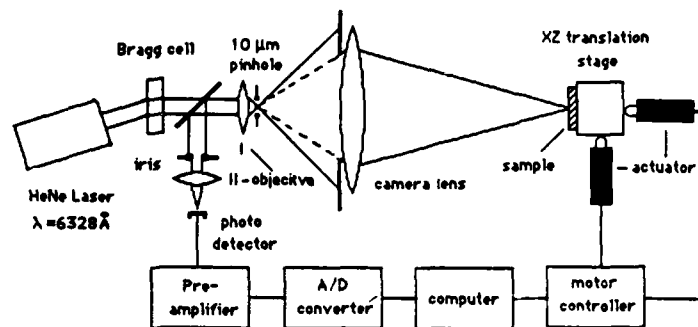


Fig. 1. Experimental arrangement of optical range finder.

light onto a point on the object. An image of this point is, in turn, focused on the pinhole. The reflected light passes back through the pinhole and is detected by the photodetector. When the object is located exactly at the focus of the transmitted light, the maximum amount of light passes through the pinhole. Otherwise, when the system is partially defocused, the amount of light passing through the pinhole is reduced. We therefore expect the signal output from the detector to have a strong dependence on the position of the object.

Because a focused beam is employed and the phase changes between the different rays comprising the beam are very small, the phase fluctuations of the laser are unimportant; therefore, a semiconductor laser, or even an incoherent source, can be used. Furthermore, the employment of a focused beam implies that the transverse definition of the system is excellent.

It will be noted that the system shown is deceptively simple. In confocal scanning microscopy, it is common to employ two pinholes so as to eliminate the reflected light from the transmitting pinhole, or to use a collimated input beam to the objective lens instead of a pinhole.^{3,4} In both cases, the light passes through the pinhole only once. The optical alignment procedure required for an optical range finder, which has a much longer working distance than the microscope, is extremely difficult with such a two-pinhole system. Thus, our system uses the single pinhole technique in which the light beam passes through the pinhole twice. It is easy to align and very stable. In this case, the light reflected back from the 10 μm pinhole is eliminated by focusing the beam to a spot size of 5-6 μm.

We assume a lens with a pupil function $P(\theta)$ where θ is the angle between the ray from the pupil plane to the focal point and the axis. By following the derivation of Richards and Wolf⁵ for vector fields, with some minor changes, it can be shown that the transverse electric field associated with a plane wave focused by the lens to a point on axis a distance z beyond the focal plane is of the form

$$D(z) = \int_0^{\theta_0} \frac{(1 + \cos \theta) \sin \theta}{(\cos \theta)^{1/2}} e^{jkz \cos \theta} P(\theta) d\theta \quad (1)$$

It will be noted that there is a $(\cos \theta)^{1/2}$ term in the denominator rather than in the numerator, as it is in Wolf's theory, in order to conserve power at a flat exit plane from the lens.

The integrand of Eq. (1) expresses the amplitude and phase of the plane wave components of the E field at an angle θ to the axis. When a focused beam is reflected from a plane mirror, its image will be a distance $2z$ away from the focus. In our apparatus, the reflected image is refocused onto the pinhole in front of the detector. Thus, it is the field on axis at the focal plane of the objective lens which is imaged at the pinhole. This field is of the form

$$V(z) = \int_0^{\theta_0} \frac{(1 + \cos \theta) \sin \theta}{(\cos \theta)^{1/2}} e^{2jkz \cos \theta} P(\theta) R(\theta) d\theta \quad (2)$$

where the output signal from the detector is proportional to

$$I(z) = |V(z)|^2 \quad (3)$$

In these expressions, $R(\theta)$ is the reflection coefficient of the plane reflector, k is the wave number ($2\pi/\lambda$), f is the focal length of the lens, and $\sin \theta_0$ is its numerical aperture, where $\sin \theta_0 = a/f$, and the radius of the lens is a . With uniform excitation, $[R(\theta) = 1]$ for $\theta < \theta_0$, $ka \gg 100$, and a plane reflector $[R(\theta) = 1]$. An approximate expression for $|V(z)|$ has been derived by Liang et al.⁶

$$|V(z)| = \left| \frac{\sin kz(1 - \cos \theta_0)}{kz(1 - \cos \theta_0)} \right| \quad (4)$$

This expression accurately predicts the shape of the central lobe; however, it fails to account for asymmetries in the sidelobes. The depth of focus is given by the 3 dB points of the central lobe in Eq. (4).

$$(\Delta z)_3 \text{ dB} = \frac{0.443 \lambda}{1 - \cos \theta_0} \quad (5)$$

For small θ_0 , the numerical aperture (N.A.) of the lens is given by the relation $[N.A. = \sin(\theta_0) \approx \theta_0]$. With $\cos \theta_0 \approx 1 - \theta_0^2/2$, we can write Eq. (5) in the form

$$(\Delta z)_3 \text{ dB} \approx \frac{0.886 \lambda}{(N.A.)^2} \quad (6)$$

We used a 4 mW He-Ne laser with a wavelength of 6328 Å in these experiments. A semiconductor laser could have been employed equally well; we chose to work with the gas laser initially only because of its availability and the greater ease of working with visible light in the early experiments. We found it convenient to use a Bragg cell for amplitude modulation of the incident light; with a semiconductor laser, we could directly modulate the laser itself. Since the objective lens is not specially coated for the He-Ne wavelength, there is still some light reflected back from the objective lens. To reduce the amount of the reflected light reaching the detector, we simply place an iris diaphragm

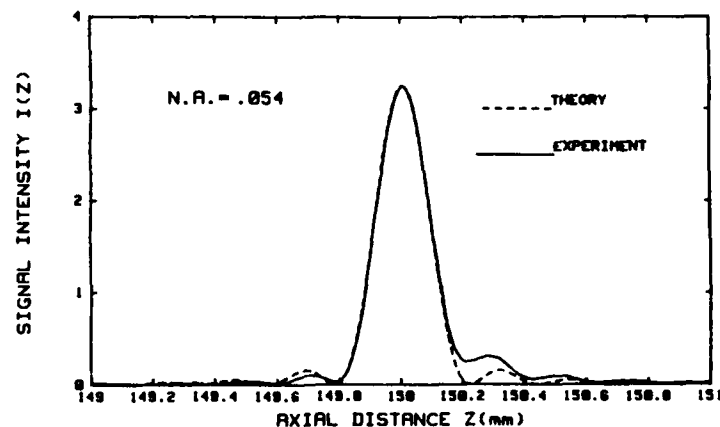


Fig. 2. The dependence of the detected signal amplitude on object distance for a mirrored surface.

before the photodetector. An iris diaphragm placed between the pinhole and the objective lens reduced the numerical aperture of the reflected light. This increased the spot size of the returning one-way spatial filter. The object was moved by two actuators in the axial direction z and the transverse direction x . The whole system was controlled by a computer.

RESULTS

To demonstrate the usefulness of this system for obtaining accurate distance measurements, we used a mirror as the reflecting object and scanned it in the axial direction z . Figure 2 shows the dependence of the signal on the position of the object. The numerical aperture of the optical system is 0.054, the corresponding depth of focus is $188 \mu\text{m}$, and the spot size is about $10 \mu\text{m}$. The experimental curve fits the theoretical curve very well, except for some discrepancy in the side lobes, which is believed to be caused by aberrations in the optical system. By determining the position of the peak of the curve, we can determine the position of the object very accurately.

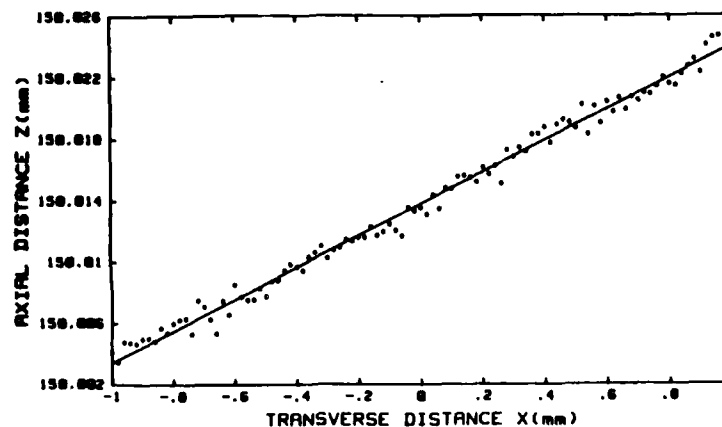


Fig. 3. One-dimensional scan over a tilted mirror.

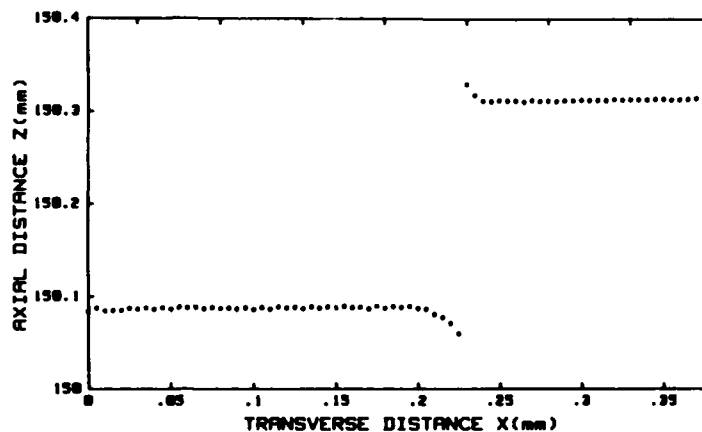


Fig. 4. One-dimensional scan over a 220 μm mirror step.

To determine the sensitivity of our measurement technique, we scanned the focused beam over a tilted mirror, as shown in Fig. 3. The straight line represents the mirrored surface and the dots are experimental results. The estimated accuracy is about 2 μm . As we tilted the mirror, the height of the central lobe decreased and the depth of focus increased. This is because less light could be collected by the camera lens, so the effective numerical aperture decreased.

The results of a subsequent scan over a 220 μm step on a specular reflector are shown in Fig. 4. The transverse spacing between adjacent points is 5 μm . Except for the overshoot near the step, the accuracy of the range measurement is about 2 μm . The overshoot is due to shadowing and interference effects which are illustrated in Fig. 5. The focused light is reflected by both top and bottom surfaces. Most of the light reflected from the bottom surface is blocked by the step, except that reflected back at a small angle. The interference between the two beams shifts the center peak and causes the overshoot effect.

This system is not only suitable for measurements on smooth surfaces, but also for measurements on rough surfaces. This is because when the light is focused to a point on a rough surface, the reflected light will be scattered in all directions, but an image of this point

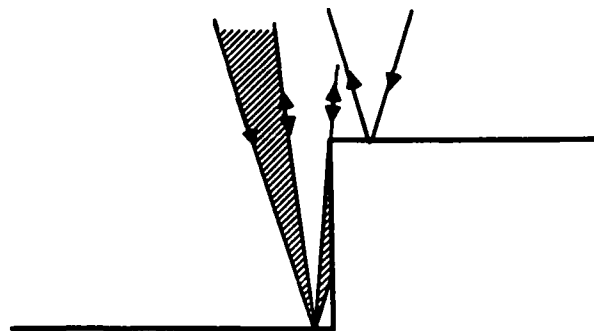


Fig. 5. Illustration of shadowing and interference effects.

$I(Z)$ ON MIRROR AND ALUMINUM SURFACES

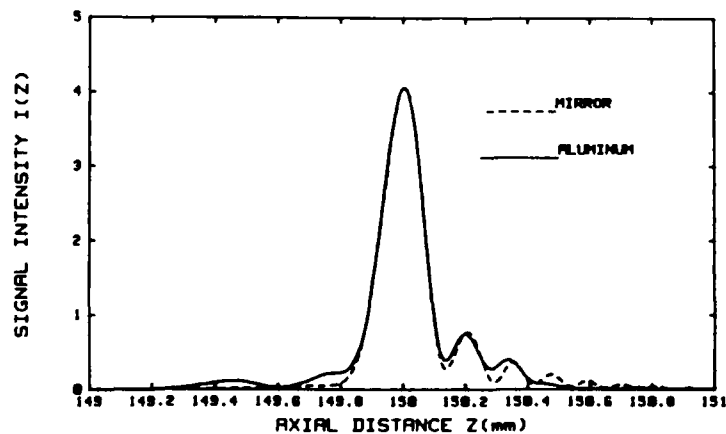


Fig. 6. Dependence of the detected signal amplitude on the object distance for a raw aluminum sample.

can still be obtained at the pinhole. We pay a price for this convenient result - the light reaching the pinhole is much reduced in intensity; the advantage is that the alignment of the rough surface is relatively uncritical. To demonstrate this effect, we scanned a sample of sheet aluminum over the surface, as supplied by the manufacturer. The results we obtained are shown in Fig. 6. The central lobe of this curve is unchanged from the central lobe obtained using a mirror. As expected, the detected signal from this rough surface is much weaker than that for a smoother surface, but it is still strong enough to be easily detected with a narrowband receiving system. The results obtained were insensitive to the tilt of the object, which is essential for the measurement of ordinary machined parts.

CONCLUSIONS

We have demonstrated an optical range finder with a range accuracy of $2 \mu\text{m}$ and a transverse definition of $10 \mu\text{m}$ at a working distance of 15 cm. The device, based upon the type II microscope principle, is very stable, easy to align, and suitable for measurement over both smooth and rough surfaces.

ACKNOWLEDGMENT

This work was supported by the Stanford Institute for Manufacturing and Automation, and by the Air Force Office of Scientific Research under Contract No. AFOSR 84-0063C.

REFERENCES

1. T. C. Strand, *Opt. Engineering* **24**, 033 (1985).
2. C. C. Williams and H. K. Wickramasinghe, "Optical Ranging by Wavelength Multiplexed Interferometry," accepted for publication, *J. Appl. Phys.*
3. C. J. R. Sheppard, *Scanned Image Microscopy*, Edited by E. A. Ash (Academic Press, London, 1980).

4. T. R. Corle, C-H. Chou, and G. S. Kino, "Depth Response of Confocal Optical Microscopes," accepted for publication, Opt. Lett.
5. B. Richards and E. Wolf, Proc. R. Soc. London A. 253, 358 (1959).
6. K. K. Liang, G. S. Kino, and B. T. Khuri-Yakub, IEEE Trans. on Sonics and Ultrasonics, Spec. Issue on Acoustic Microscopy SU-32 (2), (March 1985).

Distance measurements by differential confocal optical ranging

Timothy R. Corle, Jeffrey T. Fanton, and Gordon S. Kino

A new technique is described for measuring the distance between a lens and reflecting surface extremely accurately. It is based on the sharply peaked depth response of type II confocal systems. By dithering either the sample or the optical system, a differential measurement is generated, placing a zero-crossing at the peak of the depth response and improving the ranging accuracy. The technique is independent of surface roughness or tilt and hence is useful for robotics or machining applications. Sensitivities to surface vibrations of 0.01 nm and thin film measurements to 0.04 μm demonstrated. Signal-to-noise calculations are presented, and the procedure for measuring the thickness of transparent films is outlined.

Type II confocal scanning optical microscopes (CSOM) differ from standard (type I) confocal microscopes in that they use a columnated beam to illuminate the objective lens, thus producing a small spot on the sample. The wave reflected from the sample is then focused to a point detector.^{1,2} The net effect is to square the lens response, thus sharpening the point spread function compared with an ordinary microscope. The trade-off comes from having to take data one point at a time and build up the image using a raster scan. CSOMs are also known for their shallow depth of field.^{3,4} By exploiting this property the distance between the object and the lens can be accurately determined by looking for the peak in the amplitude response $V(z)$ as a function of distance z from a reflector to the focal point of a lens. We demonstrate that, by vibrating the sample, we can obtain an rf output from the detector at the vibration frequency Ω , which is effectively the differential of $|V(z)|^2$. Thus we can obtain a zero rf output when $|V(z)|^2$ is maximum. This zero point can be used to measure small variations in the lens object separation with great accuracy. As with direct measurements of $|V(z)|^2$, the technique is independent of surface roughness or tilt. We also present signal-to-noise calculations and results of measurements for thin films made with photoresist on silicon.

It can be shown that, as a plane reflector is scanned axially through the focal plane, the amplitude response (unnormalized) of a confocal microscope is given by the relation⁴

$$V(z) = \int_0^{\theta_0} \frac{(1 + \cos\theta) \sin\theta}{(\cos\theta)^{1/2}} \exp(2ikz \cos\theta) P(\theta) R(\theta) d\theta. \quad (1)$$

In these expressions $R(\theta)$ is the reflection coefficient of the plane reflector, $P(\theta)$ is the pupil function of the lens, k is the wave number ($2\pi/\lambda$), z is the distance between the reflector and the focal plane, and $\sin\theta_0$ is the numerical aperture of the lens. Given a uniformly excited lens of radius a , with $ka \gg 1$ and $(1 + \cos\theta)/\cos\theta^{1/2} \sim 2$, an approximate expression for $V(z)$ has been derived⁵:

$$V(z) = \exp[ikz(1 + \cos\theta_0)] \frac{\sin kz(1 - \cos\theta_0)}{kz(1 - \cos\theta_0)}. \quad (2)$$

This function is characterized by a sharp central lobe, with 3-dB depth of field given by⁵

$$\Delta z_{3\text{dB}} = \frac{0.443\lambda}{(1 - \cos\theta_0)}. \quad (3)$$

For a lens with numerical aperture of 0.9 in air and $\lambda = 633$ nm, the 3-dB width can be as small as 500 nm, hence distance measurements with this accuracy are easily achieved. For finer resolution it is desirable to measure the position of the maximum of the reflectivity function as accurately as possible. To measure this position we vibrated the sample using a vibration amplitude comparable to or less than the depth of focus. This vibration generated a differential measurement as shown in Fig. 1.

Physically the effect can be understood by referring to Fig. 2. When the object is in the focal plane of the lens ($z = 0$), the return rays are focused at the pinhole and a maximum in the output signal is obtained. If

The authors are with Stanford University, Ginzton Laboratory, Stanford, California 94305.

Received 21 November 1986.

0003-6935/87/122416-05\$02.00/0.

© 1987 Optical Society of America.

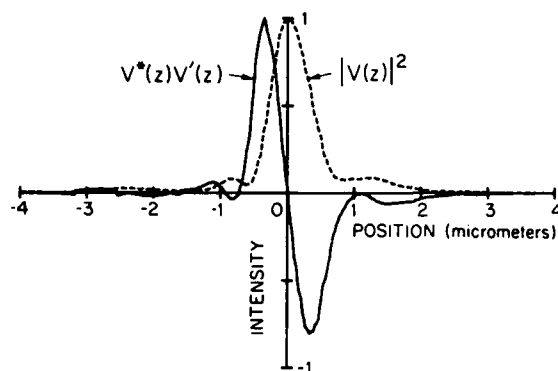


Fig. 1. Experimental $|V(z)|^2$ and $V^*(z)V'(z)$ curves. These results are for a plane reflector and a lens of numerical aperture 0.8 in air.

the object is then vibrated at a frequency Ω , two maxima will be obtained in each cycle corresponding to the two passes through the focal plane. Thus an output signal is obtained at the second harmonic (2Ω), and a zero is obtained at the output frequency Ω . When the system is defocused, however, a signal at frequency Ω is obtained whose magnitude depends on both the average distance from the reflector to the focus z_0 and the vibration amplitude z_1 .

If geometry or size considerations make it inconvenient to vibrate the sample, the lens or the pinhole may be moved to achieve the same effect. Alternatively other techniques such as the use of a flexible mirror whose focal length can be changed electronically, or an electrooptic cell, may be used to periodically defocus the image.⁶

There are two types of measurement of interest: (1) the determination of the absolute position of a surface, or by looking at two surfaces, the thickness of a thin film; and (2) the measurement of vibration amplitudes. To determine absolute distances we use the zero-crossing of the $\partial|V(z)|^2/\partial z$ curve, while in the latter case it is apparent that we should choose a value of z , where the slope of $|V(z)|^2$ is a maximum.

We may put these ideas on a more mathematical basis as follows. The small sample vibrations can be expressed as $z_1 \cos \Omega t$. We may then write

$$z = z_0 + z_1 \cos \Omega t = z_0 + \Delta z. \quad (4)$$

Expanding $|V(z)|^2$ in a Taylor Series about z_0 we obtain, to the third order in z ,

$$\begin{aligned} |V(z)|^2 &= |V(z_0)|^2 + \Delta z \left. \frac{\partial |V(z)|^2}{\partial z} \right|_{z=z_0} \\ &+ \frac{1}{2!} \Delta z^2 \left. \frac{\partial^2 |V(z)|^2}{\partial z^2} \right|_{z=z_0} + \dots \\ &= |V(z_0)|^2 + z_1 \cos \Omega t \, 2 \operatorname{Re}[V^*(z_0)V'(z_0)] \\ &+ z_1^2 \cos^2 \Omega t \operatorname{Re}[V'^*(z_0)V'(z_0) + V^*(z_0)V''(z_0)] \\ &+ \frac{z_1^3}{3} \cos^3 \Omega t \operatorname{Re}[3V'^*(z_0)V''(z_0) + V^*(z_0)V'''(z_0)] + \dots \end{aligned} \quad (5)$$

It will be observed from Eq. (5) that the leading

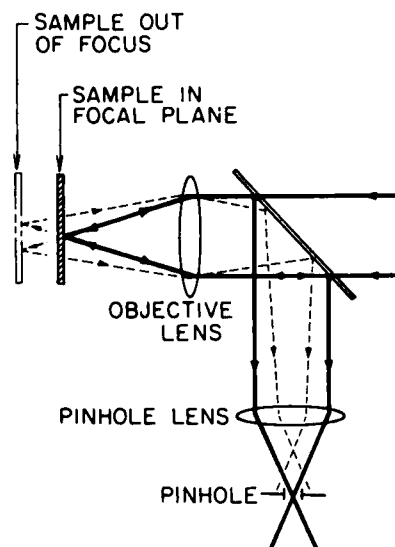


Fig. 2. Illustration of the effects of defocus on a type II microscope.

contribution to the rf term at Ω is of the form $V^*(z_0)V'(z_0)$. This derivative term is zero at $z_0 = 0$.

It follows from Eq. (2) that we can also expand $V(z_0)$ in a series of the form

$$V(z_0) = \exp(ikz_0) \left[1 - \frac{K^2 z_0^2}{3!} + \frac{K^4 z_0^4}{5!} + \dots \right], \quad (6)$$

where $K = k(1 - \cos \theta_0)$. Substituting this expansion and its derivatives into Eq. (5), to the fourth order in z_0 and z_1 we find that

$$\begin{aligned} |V(z)|^2 &= 1 - \frac{K^2 z_0^2}{3} + \frac{2K^4 z_0^4}{45} - \frac{K^2 z_1^2}{6} + \frac{2K^4 z_0^2 z_1^2}{15} \\ &+ \cos \Omega t \left(-\frac{2K^2 z_0 z_1}{3} + \frac{8K^4 z_0^3 z_1}{45} + \frac{2K^4 z_0 z_1^3}{15} \right). \end{aligned} \quad (7)$$

Equation (7) gives us a series approximation for the D.C. and first harmonic ($\cos \Omega t$) terms in Eq. (5). It may be used to calculate the optimum values of z_0 and z_1 for the measurement of absolute distances and vibration amplitudes. To measure absolute distance accurately we work near the focal point, where z_0 is small. Keeping linear terms in z_0 we find that the rf output varies with the vibration amplitude and is maximum when $K^2 z_1^2 = 5/3$, or

$$z_1 = \frac{0.20\lambda}{(1 - \cos \theta_0)}, \quad (8)$$

a movement of only 0.35λ for a 0.9 numerical aperture lens. With this vibration amplitude Eq. (7) reduces to

$$|V(z)|^2 = 0.72 + \cos \Omega t (-0.57Kz_0). \quad (9)$$

The output signal at frequency Ω becomes zero when $z_0 = 0$, i.e., when $|V(z_0)|^2$ is maximum. The sign of the rf signal is determined by the term in the brackets, so the rf signal is positive for negative z_0 and negative for positive z_0 as in Fig. 1. Hence a true zero-crossing is obtained at $z_0 = 0$.

The best sensitivity for the detection of acoustic waves and other small rf vibrations is obtained when we operate at the maximum slope of the $|V(z)|^2$ curve. The maximum slope is obtained when $K^2 z_0^2 = 15/8$, or

$$z_0 = \frac{0.22\lambda}{(1 - \cos\theta_0)} \quad (10)$$

If we include only the zeroth and first harmonic terms, the magnitude of $|V(z)|^2$ when z_0 is fixed at this value is

$$|V(z)|^2 = 0.63 + \cos\Omega t(-0.49Kz_1). \quad (11)$$

We are now in a position to determine the SNR of this technique. We shall carry out the derivation for small displacements and determine from Eq. (9) the minimum value of z_0 that can be detected.

The power entering the detector is given by

$$P = P_0 |V(z)|^2, \quad (12)$$

where P_0 is the power reaching the detector at $z_0 = 0$.

The current I from the detector is

$$I = \frac{q\eta P}{h\nu} = \frac{q\eta P_0 |V(z)|^2}{h\nu}, \quad (13)$$

where q is the charge of an electron, η is the quantum efficiency of the detector, h is Planck's constant, and ν is the optical frequency.

The mean-square noise current from the detector (i_n^2) is

$$\langle i_n^2 \rangle = 2qI_0 B + 4kTBF/R_0, \quad (14)$$

where I_0 is the average current from the detector, k is Boltzmann's constant, T is the temperature, B is the bandwidth, R_0 is the input impedance, and F is the noise figure of the preamplifier when supplied from a high impedance detector.

We shall assume that either the input impedance R_0 , the input power, or both quantities, are large enough so that the last term in Eq. (14) can be ignored and the system is shot-noise limited. In this case we can write

$$\langle i_n^2 \rangle = 2qI_0 B = \frac{2q^2 \eta P B}{h\nu}. \quad (15)$$

It follows from Eqs. (9) and (13) that the mean-square signal current from the detector is

$$\langle I_s^2 \rangle = \frac{1}{2} \left[\frac{0.57}{0.72} \frac{Kz_0 q \eta P_0}{h\nu} \right]^2. \quad (16)$$

So the SNR is

$$\text{SNR} = \frac{\langle I_s^2 \rangle}{\langle i_n^2 \rangle} = 0.11 \frac{P_0 \eta (Kz_0)^2}{h\nu B}. \quad (17)$$

For a signal-to-noise of unity, the minimum detectable value of z_0 is $z_{0\min}$:

$$z_{0\min} = \frac{0.40\lambda}{(1 - \cos\theta_0)} \left[\frac{h\nu B}{P_0 \eta} \right]^{1/2}. \quad (18)$$

As an example with $\lambda = 633 \text{ nm}$, $h\nu = 3.13 \times 10^{-19} \text{ J}$, and using a lens with an angle aperture of 0.9 in air, a detector with quantum efficiency $\eta = 0.8$, a bandwidth of 1 kHz, and $P_0 = 0.1 \text{ mW}$, we find $z_{0\min} = 8.9 \times 10^{-4} \text{ nm}$. A similar calculation based on Eq. (11), using the

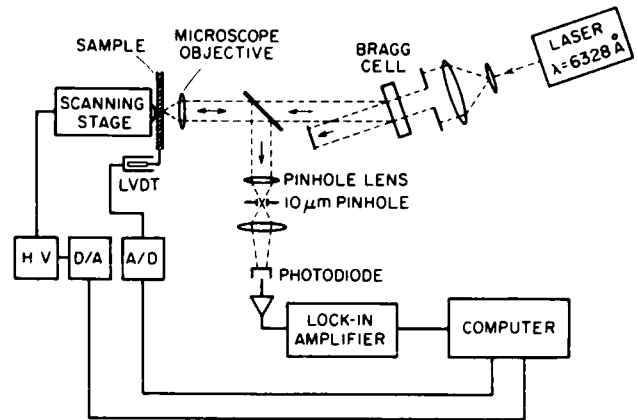


Fig. 3. Schematic of the electronically controlled type II microscope used to make the measurements.

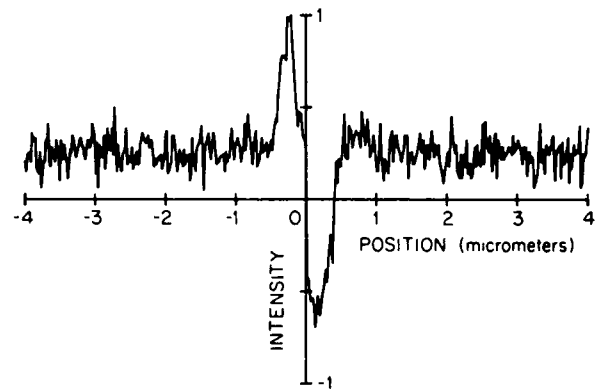


Fig. 4. $V^*(z)V'(z)$ curve for small amplitude vibrations; $z_1 = 0.01 \text{ nm}$.

same parameters, indicates that the minimum detectable value of z_1 is, $z_{1\min} = 8.6 \times 10^{-4} \text{ nm}$. Hence, with our technique in a shot-noise limited system, intensity measurements can yield interferometric accuracies.

To measure $|V(z)|^2$ and $V^*(z)V'(z)$ we used the electronically controlled type II microscope shown in Fig. 3. The sensitivity of our technique to small surface movements was determined by attaching a reflecting surface to a PZT bulk wave transducer. Scans were made while the transducer was driven at 150 kHz. Figure 4 shows the results obtained for oscillations with an amplitude of $z_1 = 0.01 \text{ nm}$. As can be seen, the signal is still quite strong, indicating surface movements in this range can easily be detected. The results in Fig. 4 also imply that our experimental apparatus is not shot-noise limited, primarily because the input impedance of our amplifier was only 50 Ω .

In addition to excellent distance resolution, this technique has several other characteristics which make it useful for remote distance sensing. First, the system has excellent transverse resolution. Because the objective lens is used twice, once to focus the incoming plane waves to a point and a second time to image this point onto the pinhole, the transverse resolution is given by the square of the lens response. For

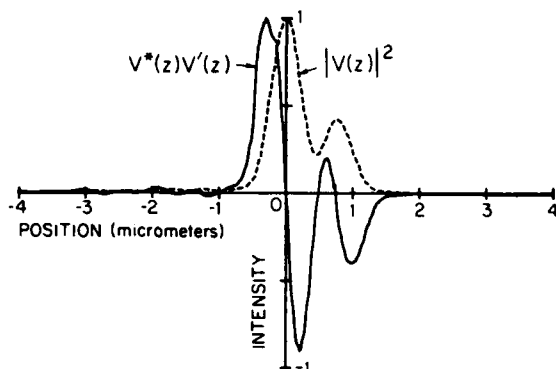


Fig. 5. $|V(z)|^2$ and $V^*(z)V'(z)$ curves for 1.8 μm of photoresist on silicon.

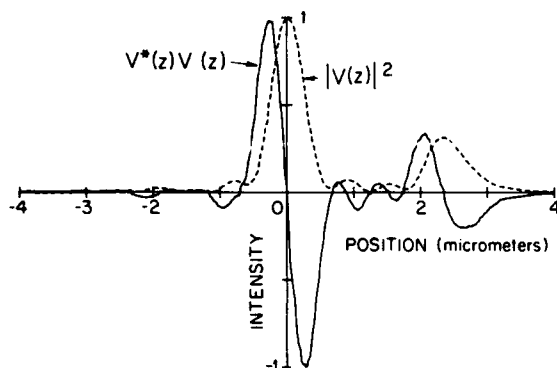


Fig. 6. $|V(z)|^2$ and $V^*(z)V'(z)$ curves for 4.86 μm of photoresist on silicon.

a 0.9 numerical aperture lens and $\lambda = 633 \text{ nm}$, the 3-dB width of the point spread function is only $0.35 \mu\text{m}$, a 27% improvement over conventional microscopes. Also, it has been demonstrated that the shape of the central lobe of $|V(z)|^2$ is independent of surface roughness or tilt (although the amplitude does vary with the reflectivity of the sample).⁴ Hence $V^*(z)V'(z)$ measurements are also independent of surface conditions. Finally, since this technique only depends on the focusing properties of the objective lens, phase stabilization of the system is not necessary. A multimode semiconductor laser, or even an incoherent LED source, can be used.

We can apply differential techniques to the measurement of thin films. With a thin film more than one reflecting plane is present, and the $|V(z)|^2$ curve has two peaks corresponding to the focusing on at the top and bottom surfaces of film. In this case differential techniques may be used to improve the accuracy of the film thickness measurements. Results are shown in Fig. 5 for 1.8 μm , and in Fig. 6 for 4.86- μm films. For thick films such as the 4.86- μm film, the results obtained are very accurate. For thinner films, where the two peaks tend to overlap, the measurement of film thickness is accurate only of the order of half a wavelength. This inaccuracy is primarily due to interference with an unknown phase difference between the reflected waves from the top and bottom surface of the

film. This problem can be overcome by using a broadband source with a coherence length less than the film thickness, or by direct comparison with calibrated samples. Alternatively the equations for $V^*(z)V'(z)$ could be fit to the data in an iterative manner, but this approach is often difficult and time-consuming. For thicker films, where the peaks do not overlap, interference does not occur, so the film thickness may be directly measured.

To determine the film thickness from the data one needs to account for the index of refraction of the film material. One approach is to modify the form of Eq. (1). Let the reflection coefficients from the top and bottom surfaces be R_1 and R_2 . We shall denote all quantities outside and inside the film by the subscripts 1 and 2, respectively, and for simplicity we shall take R_1 and R_2 to be independent of θ .

In this case Eq. (1) can be rewritten as

$$V(z) = \int_0^{\theta_0} \frac{(1 - \cos\theta_1)\sin\theta_1}{\cos\theta_1} \exp(2ik_1z \cos\theta_1) \times [R_1 + R_2 \exp(2ik_2h \cos\theta_2)] P(\theta_1) d\theta_1, \quad (20)$$

where h is the film thickness, and k_1 and k_2 are the wave numbers outside and inside the film. The angle θ_2 can be found by using Snell's law,

$$\sin\theta_2 = \frac{n_1}{n_2} \sin\theta_1, \quad (21)$$

where n_1 is the index of refraction of the material surrounding the objective lens (in our case, air), and n_2 is the index of refraction of the film material.

Direct integration of Eq. (20) for $h = 4.86 \mu\text{m}$, $n = 1.63$, $P(\theta) = 1$, $R_1 = 0.39$, and $R_2 = 1.0$ reproduces the data fairly accurately as shown in Fig. 7. Past experience has shown us that we can improve upon this result by introducing a pupil function of the form

$$P(\theta) = \exp(A \sin^2\theta) \exp(iB \sin^4\theta). \quad (22)$$

Values of $A = 0.2$ and $B = 6$ have been shown previously to account for aberrations in our system.⁴ In this case, however, the introduction of phase aberrations makes things much worse as shown in Fig. 7. This behavior could be the result of unknown phase aberrations within the film, the fact that the aberrations of Eq. (22) are an oversimplification, or other system aberrations not yet understood.

From the integration of Eq. (20) we measure the distance between the two maxima (h_c). The ratio of the actual film thickness to the calculated distance (h/h_c) gives us the multiplicative factor needed to account for the index of refraction of the film. This multiplicative factor is, to the first order, independent of the film thickness. Thus the ratio h/h_c need only be calculated once for each index material. For a photoresist film with $n = 1.63$ at $\lambda = 633 \text{ nm}$, $h/h_c = 2.08$ yielding a measured film thickness of $4.86 \mu\text{m}$. Lack of detailed understanding of the system aberrations remains the limiting factor in improving the accuracy of the thin film measurements. With the current level of understanding we feel that accuracies of $0.04 \mu\text{m}$ (1%) are

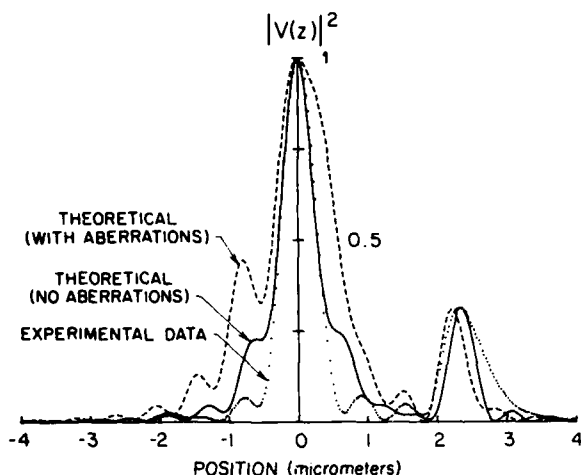


Fig. 7. Comparison of experimental data and theoretical calculations for a 4.86- μm film of photoresist on Silicon.

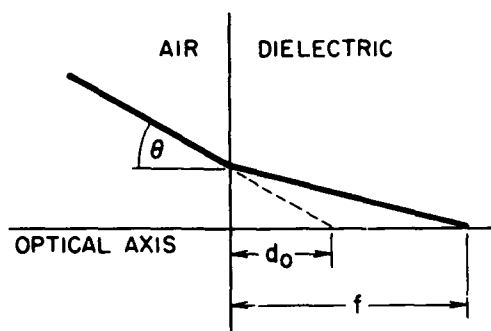


Fig. 8. Refraction of a ray incident upon a dielectric resulting in a change in the focal plane for a focused beam.

reliably obtained. Ellipsometry readings taken of the same sample give a thickness of 4.86 μm at index 1.64.

A somewhat simpler method of computing h/h_c is by calculating the distance the focal point is refracted into the material by the presence of the dielectric. A given ray impinging at an angle θ on a dielectric interface will cross the optical axis of the system at a distance (f) from the surface of the film (Fig. 8). The ratio between the distance (f) and the point where the ray would intersect the optical axis if no film was present (d_0) is given by

$$\frac{f}{d_0} = \frac{(n^2 - \sin^2\theta)^{1/2}}{\cos\theta}, \quad (23)$$

This work was supported by the Air Force Office of Scientific Research on Contract AFOSR-84-0063C. One of us, T. R. Corle, was supported by an IBM Graduate Predoctoral Fellowship for the duration of this research. The authors would also like to thank Ching-Hua Chou, and Dave Patterson for interesting discussions which contributed to this work, and Robin King for doing the ellipsometry.

where n is the index of refraction of the film material, and the material outside the film is assumed to be air ($n = 1$). To determine the focal shift of the beam, and hence the multiplicative factor, we integrate Eq. (23) over all angles in the focused beam:

$$\frac{h}{h_c} = \frac{\int_0^{\theta_0} \frac{(n^2 - \sin^2\theta)^{1/2}}{\cos\theta} \sin\theta d\theta}{\int_0^{\theta_0} \sin\theta d\theta}. \quad (24)$$

For photoresist with $n = 1.63$ at $\lambda = 630 \text{ nm}$, $h/h_c = 2.12$ giving a thickness of 4.91 μm . While this method is not strictly correct since it does not account for diffraction within the film, it offers a quick way of calculating the correction factor to within a couple of percent.

We have demonstrated that, by vibrating the sample in a confocal scanning microscope, the distance between the lens and the sample can be accurately determined. The technique is based on the shallow depth of focus properties of confocal optical microscopes. It exhibits excellent transverse resolution and can be used to image rough samples. It also has the advantage of being phase independent, hence cheap diode lasers or incoherent sources may be used. Signal-to-noise calculations are presented which illustrate that our intensity technique is comparable in sensitivity to phase-dependent interferometric techniques. The thicknesses of photoresist films have been measured to within 0.04 μm and theoretical calculations presented which correct for the index of refraction.

References

1. C. J. R. Sheppard, in *Imaging Modes of Scanning Optical Microscopy*, E. A. Ash, Ed. (Academic, New York, 1980).
2. T. Wilson and C. J. R. Sheppard, *Theory and Practice of Scanning Optical Microscopy* (Academic, London, 1984).
3. D. K. Hamilton, T. Wilson, and C. J. R. Sheppard, "Experimental Observation of the Depth-Discrimination Properties of Scanning Microscopes," *Opt. Lett.* 6, 625 (1981).
4. T. R. Corle, C.-H. Chou, and G. S. Kino, "Depth Response of Confocal Optical Microscopes," *Opt. Lett.* 11, 770 (1986).
5. K. K. Liang, G. S. Kino, and B. T. Khuri-Yakub, "Material Characterization by the Inversion of $V(z)$," *IEEE Trans. Sonics Ultrason.* SU-32, 213 (1985).
6. G. S. Kino, C.-H. Chou, T. R. Corle, and P. C. D. Hobbs, "Scanning Differential Contrast Microscopy," presented at the DARPA Review of Progress in Quantitative NDE, San Diego CA (Aug '86). To be published in *Rev of Prog in Quant Nondest Evaluation*, Vol. 6, Eds. D. O. Thompson and D. E. Chimenti (Plenum Press, New York, 1987).

A Reprint from the

PROCEEDINGS

Of SPIE - The International Society for Optical Engineering



Volume 749

Metrology: Figure and Finish

15-16 January 1987
Los Angeles, California

Phase measurements with a type 2 microscope

G. S. Kino, P. C. D. Hobbs, T. R. Corle

Edward L. Ginzton Laboratory, W. W. Hansen Laboratories of Physics
Stanford University, Stanford, California 94305

Phase Measurements with a Type 2 Microscope

G. S. Kino, P. C. D. Hobbs, and T. R. Corle

Edward L. Ginzton Laboratory; W. W. Hansen Laboratories of Physics
Stanford University; Stanford, California 94305

Abstract

We describe two ways which we have developed for obtaining phase information in Type 2 (confocal) microscopes: heterodyne interferometry using a Bragg cell for both scanning and frequency shifting, and a novel "heterodyne phase contrast" technique using a time-variable electro-optic phase plate, somewhat similar to a Zernike phase plate with mechanical scanning. The heterodyne interferometer can measure amplitude to 0.2% and phase to the 0.1° level at a rate of 30,000 to 50,000 points per second, with excellent vibration immunity. The heterodyne phase contrast system is slower, but is a single-beam system and could be retrofitted to a standard Type 2 system without affecting normal operation. If scan stage vibration can be neglected, for example in acoustic wave detection, it should be able to measure optical phase to around 0.1 millidegree; however, this accuracy is not yet demonstrated.

Introduction

The purpose of phase measurements in microscopy is well known: they provide additional information about the sample, independent of the intensity information, which may be obtainable in no other way. Conventional phase contrast, as well as shearing and Nomarski interference microscopes, perform very well for optically thin or highly reflective samples; the lack of amplitude contrast with such samples means that the image is simply a phase map. These instruments are incapable of producing quantitative phase data for more general classes of samples because they lack any provision to separate the amplitude and phase contributions to the contrast. Our systems remove this ambiguity by using AC techniques to sample the optical amplitude and phase simultaneously and independently.

Heterodyne Interferometry

The idea of this system has been presented before,^{1,2} and so will be described only briefly. Figure 1, reprinted from reference 1, shows a simplified version of the optical system of the heterodyne interference microscope. A single-frequency laser beam at 514.5 nm comes into an acousto-optic Bragg cell which is placed at the pupil of a factory-modified Leitz Orthoplan microscope. An undiffracted beam passes through the Bragg cell, along with a steerable first-order beam which has been downshifted by the acoustic frequency f_B . These beams are focused to diffraction-limited spots on the sample. The undiffracted beam forms a stationary reference spot, the steerable beam a spot which scans as the acoustic frequency is varied.

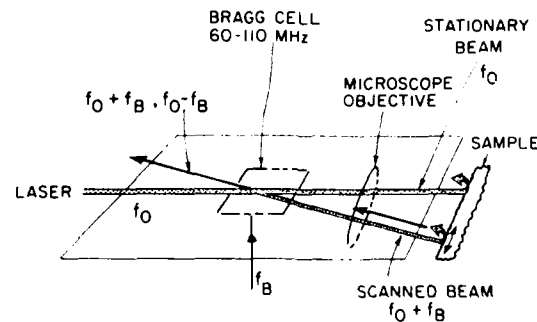


Fig. 1. Simplified diagram of the heterodyne interference microscope.

The beams reflected from the sample retrace their paths and pass through the cell again, in the other direction. Of the resulting four beams, we select the two (coaxial) singly-diffracted ones, one from each spot. The beam from the scanned spot has been downshifted; the one from the stationary spot has been upshifted. These two beams interfere on a photodiode, producing a product signal at twice the acoustic frequency. The normalized complex amplitude of this signal, an RF tone in the 120-220 MHz band, is

equal to the complex reflection coefficient of the sample at the position of the moving spot. Now the problem of measuring the optical amplitude and phase of the scanned beam is reduced to an RF measurement, which can be done very quickly and accurately.^{2,3} We have demonstrated scan speeds of 35,000 points per second with accuracies of a few tenths of a degree in phase, and 0.2% in amplitude with a dynamic range of 70 dB. This level of phase error corresponds to a height resolution of a few Angstroms.

The signal from the photodetector is the product of the amplitude illumination pattern (the scanned spot), the sample reflection coefficient as a function of position, and the sensitivity pattern (the stationary spot superimposed by the Bragg cell). Since the illumination and sensitivity patterns are identical sinc functions, the microscope's point spread function is their square; thus, the microscope is of Type 2. We refer to this property as a "virtual pinhole."

Since the reference beam is on the sample, the system has excellent immunity to sample vibrations; any vertical vibration of the sample causes equal phase shifts in the two beams, which then cancel each other when the two beams interfere. Horizontal vibrations are no more of a problem than in conventional microscopes; twisting motions can introduce differential phase shifts, but as the two spots are usually 100 μm apart (or less), this is not very serious.

This system has one disadvantage, as compared to single-beam microscopes, which it shares with shearing interference microscopes: it demands a smooth area for the reference spot. If this condition is not met, the sensitivity pattern will no longer be identical to the illumination pattern, and the microscope will no longer be of Type 2. This condition is usually accompanied by a large decrease in signal level. The smooth area need be only a micron or so in diameter, so this isn't a particularly serious fault.

Since both amplitude and phase are available, we exploit the extra spatial frequency bandwidth of the Type 2 transfer function⁴ with an inverse filter to achieve a factor of two sharper resolution² at any given wavelength. The filtering is done digitally and takes less than 30 seconds for 1024 points on a personal computer.

Heterodyne Phase Contrast

The heterodyne phase contrast system is shown in Fig. 2; it is a standard Type 2 microscope with an electro-optic phase plate at the pupil. The E-O plate, shown in Fig. 3, is a 2 mm thick block of PLZT with a transparent indium tin oxide electrode covering a central disk. Since PLZT is an electrostrictive material with large off-diagonal coupling coefficients, an applied voltage causes the optical path length through the central region to increase or decrease; thus the relative phase of the pupil's central region and outer annulus can be modulated. There is an obvious similarity between our E-O plate and the Zernike phase plate; however the principle is quite different, as will presently be seen. A complete analysis of the imaging behavior of this system in both the horizontal and the vertical directions is under way, to be published at a later date, but the main features of the phase imaging may be shown by the following heuristic presentation.

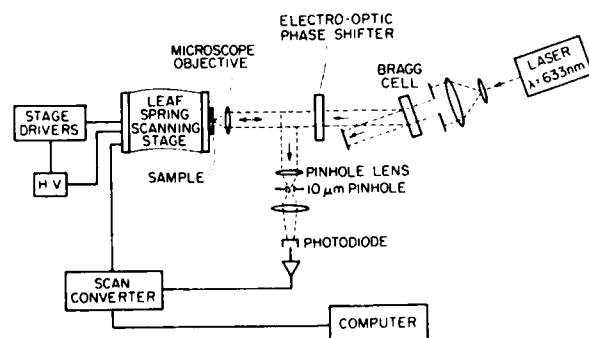


Fig. 2. Schematic of the mechanically-scanned heterodyne phase contrast microscope showing the placement of the electro-optic phase plate.

Consider an optical beam focused just inside a dielectric film (n_1), which covers a reflecting plane (Fig. 4). The top surface is considered to be $z = 0$. If, in the absence of the film, the beam would be focused at a point z , then, because of refraction, the outermost rays will actually cross the axis at a point z' , where:

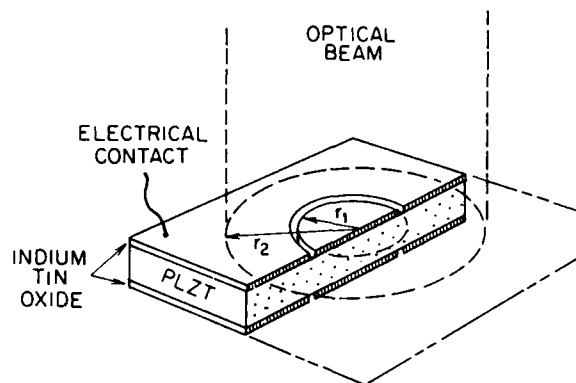


Fig. 3. Illustration of the electro-optic plate used to phase shift a portion of the illuminating beam.

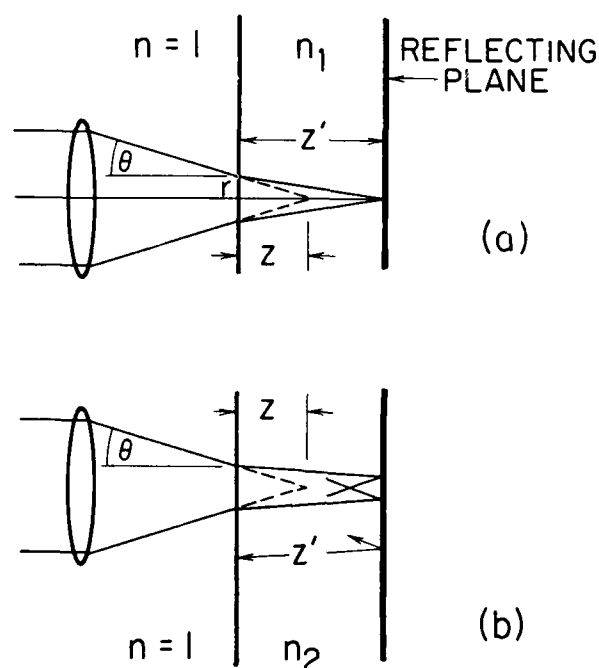


Fig. 4. (a) An optical beam focused into a dielectric n_1 illustrating the path difference between the center and outermost rays. (b) The same beam focused into a dielectric n_2 .

$$z' = \frac{z(n_1^2 - \sin^2 \theta)^{1/2}}{\cos \theta}$$

and θ is the angle the rays make with the axis. The path difference between the axial and outermost rays is:

$$\begin{aligned} \Delta z' &= \sqrt{z^2 + r^2} - z' = [z^2(n_1^2 - \sin^2 \theta)/\cos^2 \theta + z^2 \tan^2 \theta]^{1/2} \\ &\quad - z(n_1^2 - \sin^2 \theta)^{1/2}/\cos \theta \end{aligned}$$

so that the phase difference is:

$$\Delta\phi = \frac{kz}{\cos\theta} [n_1^2 - (n_1^2 - \sin^2\theta)^{1/2}]$$

Hence, the phase difference between the rays at any given plane depends on the film's index of refraction. If we use the electro-optic plate to modulate the phase of the axial ray, that phase will be $\exp[i(\omega t + \alpha \cos \Omega t)]$; the phase of the outermost ray is $\exp[i(\omega t + \Delta\phi)]$. The two rays will interfere on the detector (thanks to the pinhole), and the resulting photocurrent will have the form:

$$I_p = \cos(\alpha \cos \Omega t - \Delta\phi) + (\text{other DC terms})$$

For small modulation index ($\alpha \ll 1$), the AC term is $I_p \approx \alpha \sin \Delta\phi \cos \Omega t$. We see that a signal at the modulation frequency is obtained whose amplitude gives the sine of the optical phase; if it is multiplied by the modulating signal in a balanced mixer or synchronous rectifier, the resulting bipolar output voltage will faithfully reproduce this characteristic. The DC term is just the standard Type 2 microscope response, which is essentially unaltered by the phase plate's action. The AC signal still contains the amplitude information as well as the phase. To obtain truly independent data, we must divide the AC voltage by the DC term, an elementary task whether done in analog circuitry or in software.

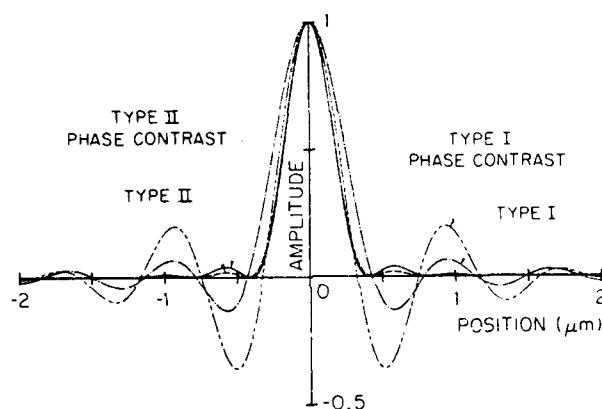


Fig. 5. Amplitude point spread function of the heterodyne phase contrast system as compared with Type 1, Type 2, and coherent Zernike microscopes.

We have calculated the in-focus point spread function (PSF) of the microscope from Fourier optics for both the AC and DC components. The DC PSF is only very slightly affected by the presence of the E-O plate; it is equivalent to the conventional Type 2 PSF shown in Fig. 5. The AC PSF has a slightly narrower main lobe and somewhat higher side lobes than the DC response; the difference, however, is by no means as pronounced as that between the Type 1 and coherent Zernike systems. In dramatic contrast to the coherent Zernike system, the AC PSF of our microscope exhibits a very compact structure with tightly confined sidelobes; there is none of the halo or shading off which bedevils edge measurements with Zernike systems.

Although we are still in the early stages of this work, by analogy with other systems the ultimate height resolution of the system should be shot noise limited at around 10^{-3} Å. As it is a one-beam system, however, vertical vibrations will limit the resolution. In practice the objective to sample distance is generally only a few millimeters, and so vibrations can be minimized by careful mechanical design. Some applications, such as detection of acoustic waves, are insensitive to these low-frequency vibrations and so could take advantage of the instrument's full capabilities.

In this early version, the inner region of the E-O cell was driven with a 10 kHz sine wave of 300 V (p-p) amplitude, producing a phase shift of about 6° in the inner region of the pupil (later versions will drive the outer annulus in order to eliminate the need for a conducting path to the center electrode). Figure 6 shows the bipolar AC response observed while a plane reflector was scanned through the focal region; the curve

was obtained by measuring the AC output at 10 kHz with a single-channel lock-in amplifier. We see that, as the plane reflector moves away from the focal plane, a signal is generated proportional to the distance off focus, as the simple theory predicts.

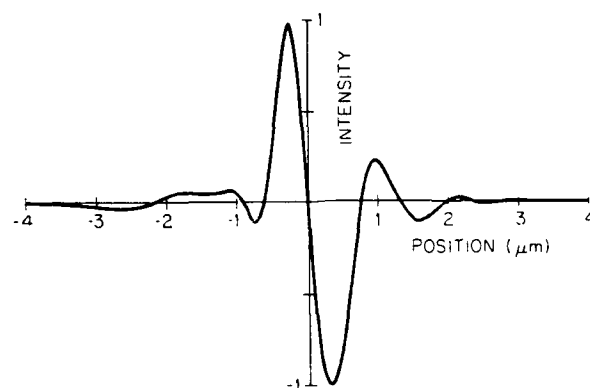


Fig. 6. Variation of the AC signal with depth in the heterodyne phase contrast system.

Acknowledgements

This work was supported by the Air Force Office of Scientific Research under Contract No. AFOSR 84-0063C. The authors gratefully acknowledge the support of E. Leitz Wetzlar GMBH, W. Germany.

References

1. Jungerman, R. L., P. C. D. Hobbs, and G. S. Kino, Appl. Phys. Lett. Vol. 45, 846 (15 October 1984).
2. Hobbs, P. C. D., R. L. Jungerman, and G. S. Kino, SPIE Proc. Vol. 565, 71 (August 1985).
3. Hobbs, P. C. D., "High Performance Amplitude and Phase Digitizers at 60 MHz," submitted to Rev. Sci. Inst.
4. Wilson, T. and C. J. R. Sheppard, Scanning Optical Microscopy, Academic Press (1984).
5. Corle, T. R. and G. S. Kino, to be published.
6. Corle, T. R., C-H. Chou, and G. S. Kino, "Depth Response of Confocal Optical Microscopes," Opt. Lett. Vol. 11, 12 (1986).

END

DATE

FILMED

9-88

DTIC